Polymers in extension: from crystallization to filament breakup

Jessica Pepe

Polymers in extension: from crystallization to filament breakup

Jessica Pepe

A catalogue record is available from the Eindhoven University of Technology Library.

ISBN: 978-90-386-5947-3

Cover design: Prakhyat Hejmady

Printed by: Gildeprint, Enschede, The Netherlands

This work was financially supported by Brightlands Material Center BMC, Geleen.

©Copyright, 2024, Jessica Pepe. All rights reserved.

Polymers in extension: from crystallization to filament breakup

PROEFSCHRIFT

ter verkrijging van de graad van doctor aan de Technische Universiteit Eindhoven, op gezag van de rector magnificus prof.dr. S.K. Lenaerts, voor een commissie aangewezen door het College voor Promoties, in het openbaar te verdedigen op donderdag 8 februari 2024 om 13:30 uur

door

Jessica Pepe

geboren te Salerno, Italy

Dit proefschrift is goedgekeurd door de promotoren en de samenstelling van de promotiecommissie is als volgt:

voorzitter:	prof.dr.ir. L.E. Govaert
promotor:	prof.dr.ir. P.D. Anderson
promotor:	prof.dr.ir. R.M. Cardinaels
1^{e} co-promotor:	prof.dr.ir. G.W.M. Peters
leden:	prof.dr.ir. J.M.J. den Toonder (Eindhoven University of Technology)
	prof.dr. C. Clasen (KU Leuven)
	dr. G. Portale (University of Groningen)
adviseur:	dr. E.M. Troisi (Sabic)

Het onderzoek of ontwerp dat in dit proefschrift wordt beschreven is uitgevoerd in overeenstemming met de TU/e Gedragscode Wetenschapsbeoefening.

Summary

Polymers are widely used in various applications and their behavior and final properties strongly depend on the processing conditions such as temperature, presence of pressure and type of flow. Among these, flow is one of the most difficult parameters to fully understand and control. Two model types of flow are shear and extension. They can be present separately in different parts of the process or simultaneously, generating, in this case, a complex flow. When semicrystalline polymers are processed, crystallization during flow becomes a dominant factor in determining the final properties. In order to characterize and understand the effect of flow on the final properties of a polymer, its rheological behavior (i.e. response to an applied flow field) and structure development in model flows should first be studied.

Shear flow is relatively easy to apply, therefore rheometers have been developed wherein controlled shear experiments with well-controlled temperature profiles can be applied and the material response can be studied. Innovative setups have been developed that capture simultaneously the rheological response as well as the evolution of the crystalline microstructure, thereby utilizing in-situ X-ray characterization. On the other hand, a pure and controlled uniaxial extensional flow is difficult to realize and therefore the challenge to design suitable measurement devices is higher, especially when in-situ structure characterization is required. The existing extensional rheometers do not allow for both controlled uniaxial extensional flows and in-situ structure characterization generating a lack of knowledge in the field.

In free surface flows the interplay between flow, interfacial properties and extensional rheology, for instance during filament stretching and breakup, becomes crucial for understanding and accurately controlling the process. Material jetting is one of such processes during which tiny droplets of a material are deposited, on demand, on a specific position of a substrate. The material choice will affect the droplet formation as well as the deposition mechanism. Despite being a mature and consolidated technique used in different fields, it has a strong limitation in handling very highly viscous fluids like polymers with a consequent scarcity of studies on the matter despite the benefit they could offer for specific applications.

Given the limitations of the current technologies to fully characterize uniaxial extensional flow induced crystallization, the first goal of this work is to provide a tool to study the effect of extensional flow on the rheology and crystalline microstructure evolution of semi-crystalline polymers. A filament stretching extensional rheometer has been designed and built in-house with the capability of applying well controlled uniaxial extensional deformations while performing in-situ X-ray experiments. After validation of the measurement capability of the novel setup, the flow enhanced crystallization of a

branched semicrystalline polymer has been investigated with a systematic study of the effect of flow parameters (i.e. strain and strain rate) under isothermal conditions. A clear correlation between flow strength, degree of orientation of the polymer chains and crystallization rate was found. Moreover, fitting the experimental scattering data with a model for shish-kebab growth, a detailed analysis of the microstructure development during crystallization was performed.

In the second part of this work, the jetting and deposition process of highly viscous polymers have been investigated with a new generation dispensing machine using a piezo-activated plunger above the dispensing nozzle. The effects of crucial parameters such as fluid viscosity, distance between nozzle and substrate and substrate properties have been studied. A rheological characterization of the fluids together with optical visualization of the filament breakup process and spreading on the substrate reveals new insights of drop on substrate deposition when highly viscous fluids are used. An understanding of the interplay between filament stretching and spreading is key for a full control of the process thereby opening new possibilities in the jetting field.

Contents

Summary iii

1 Introduction 1
- 1.1 Crystallization induced by extensional flow . . . 1
- 1.2 Jetting of highly viscous polymers . . . 2
- 1.3 Research objective . . . 3
- 1.4 Outline of the thesis . . . 4

2 A filament stretching rheometer for *in-situ* X-ray experiments: combining rheology and *in-situ* crystalline morphology characterization 5
- 2.1 Introduction . . . 6
- 2.2 Rheometer design and description . . . 7
- 2.3 Experimental procedure . . . 16
- 2.4 Results and discussion . . . 20
- 2.5 Conclusions . . . 25

3 Unraveling the extensional flow induced crystallization of LDPE via *in-situ* X-ray characterization 27
- 3.1 Introduction . . . 27
- 3.2 Materials and methods . . . 30
- 3.3 Results and discussion . . . 34
- 3.4 Conclusions . . . 50

4 A study on the jetting process of highly viscous fluids: from droplet-on-demand (DOD) to volume-on-demand (VOD) 53
- 4.1 Introduction . . . 53
- 4.2 Materials and methods . . . 56
- 4.3 Results and discussion . . . 61
- 4.4 Conclusions . . . 77
- 4.A Appendix . . . 78

5 Effect of substrate - fluid interaction on the thinning of a viscous filament 81
- 5.1 Introduction . . . 81
- 5.2 Materials and methods . . . 83
- 5.3 Results and discussion . . . 85
- 5.4 Conclusions . . . 97

6 Conclusions and Recommendations 99
- 6.1 Conclusions . . . 99

6.2 Recommendations 101

Publications **119**

Acknowledgment **121**

Curriculum Vitae **123**

CHAPTER 1

Introduction

Extensional flows are present in our everyday life: when rain falls water droplets stretch under gravitational forces and break up in smaller droplets, while baking bread the extensional properties of the gluten are responsible for the formation of a foamy structure [1], when taking a spoon of honey we can observe a long tail forming at the edge of the spoon witnessing its extraordinary extensional properties. Plants and animals make use of extensional flows to catch their prey or drink [2, 3, 4]. Extensional flow is equally important in the production of goods that we constantly use such as printed papers, clothes, packaging, to mention a few. The rheological behavior of a material is very much dependent on its molecular structure and can also be influenced by external parameters like temperature, humidity, pH, and the flow conditions itself (i.e. deformation and deformation rate). Despite the fact that extensional flows are ubiquitous, extension is, until now, the least studied field in the area of rheology. It should be clear that a proper understanding of the extensional properties of materials is essential to control the process and to obtain the desired properties and thus the final product. When semicrystalline materials are used, particularly in processes that involve dispensing such high viscous polymers, two main aspects remain mostly untouched in literature: the crystallization induced by extensional flow and the effect of high viscosity and elasticity on the dispensing process.

1.1 Crystallization induced by extensional flow

Different products require different properties and it is well established that the processing history will determine the final material characteristics. A plastic film demands different mechanical, optical and barrier properties than heavy duty ropes and thus the material choice as well as the selected type of processing method will be crucial. The majority of the polymers used are semi-crystalline thermoplastics [5]: they are easy to process in the melt state and allow to achieve a variety of properties that satisfy low and high performance applications. One of the most commonly used polymers belongs to the family of polyethylene (PE). Depending on the reaction process several polyethylenes can be obtained that differ in their molecular structure and thus in the properties achievable. The minimum energy state for polymer chains, in the melt state, is that of a random coil, and when the molecular weight increases and the chains become long enough, physical entanglements establish between them. Upon cooling

they form crystal structures called spherulites, the size and number of which depend on the cooling profile. When a flow is applied the crystallization rate is increased due to enhanced nucleation and in case of strong flow orientation induced structures called shish-kebabs are formed [6, 7].

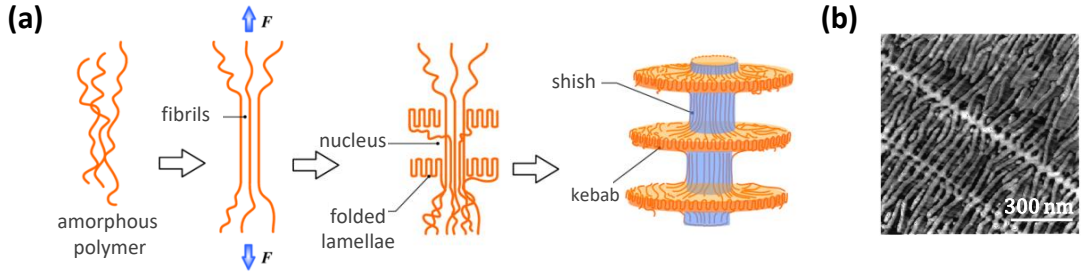

Figure 1.1: (a) Schematic representation of the shish-kebab structure formation under extensional flow (reproduced from [8]). (c) Atomic force microscopy of a shish-kebab structure in a sheared polyethylene [9]

Being able to control and predict the formation of such structures during processing is of vital importance. To gain the fundamental understanding underlying this control new experimental techniques that are able to capture structure formation under processing relevant conditions are required. While most of the studies focus on shear flow and shear flow induced crystallization, unanswered questions are left behind regarding the extensional flow enhanced crystallization.

1.2 Jetting of highly viscous polymers

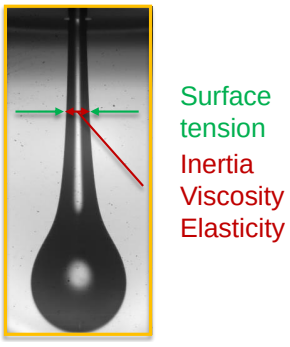

Figure 1.2: Representation of a free surface flow for highly viscous PDMS (viscosity = 60 Pa·s).

Extensional rheology plays a key role in processing dominated by free surface flow, wherein thinning and breakup of a fluid filament is driven by surface tension and resisted by viscous, inertial and extensional material contributions [10] (see Figure 1.2).One of

the processes in which these phenomena play a crucial role is material jetting (MJ), also called droplet-on-demand (DOD) technology. Material jetting is a contactless material deposition process that involves the ejection of materials, in fluid form, from a nozzle and subsequent deposition of the formed droplets on a substrate. The most known form of this process is inkjet printing, which is widely used in the paper and photograph printing industry. There can be several mechanisms that drive the material ejection and usually the choice depends on the application and the nature of the fluids. This technique is very well consolidated in the 2D world and when extended in 3D could be used for many applications thanks to its unique features. Unfortunately its main limitation lays in the material requirements. For 3D structuring or specific applications demanding properties are required. The materials satisfying these requirements, usually having high molecular weight components or fillers and, subsequently, process complexity, typically exhibit complex rheology. For low viscous fluids many studies have been performed that fully characterize the fluid ejection, droplet formation and deposition, as well as considering the effect of viscosity (in the low viscosity regime) and elasticity in case of more complex fluids. New research of the jetting process in combination with a high viscous material could lead to new discoveries and possible applications.

1.3 Research objective

Synergy between experiments and modeling provides a key tool in the control of process and product properties. Unfortunately extensional flow is not well studied because of the lack of proper instruments that enable controlled applied uniaxial extensional flows while allowing *in-situ* structure characterization. At the same time the investigation of the extensional jetting process, thinning and breakup of highly viscous fluids that could be of high interest for niche applications have never been extensively and systematically studied. The focus of this work is to overcome the above mentioned limits and offer the possibility of filling the existing knowledge gaps. Two experimental setups that allow *in-situ* characterization in extensional flow have been developed. One enables *in-line* microstructural characterizations while following the rheological response to a controlled uniaxial extensional deformation. This opens new horizons in the extensional flow induced crystallization field and helps verifying existing theories as well as introducing new fascinating questions. The other allows to perform experiments on the actual processing flow and to investigate the macrostructure of the dispensed fluid. On the other hand a systematic and fundamental study of the jetting behavior of extremely high viscosity fluids has never been performed. The effect of rheological properties (i.e. fluid molecular weight), specific process parameters, as well as substrate to nozzle distance and substrate nature have been investigated and the effects on resolution and processing time are shown. The results help building new knowledge about the use of such materials for jetting and provide a better awareness of the challenges as well as of new possibilities.

1.4 Outline of the thesis

In order to unlock new research in the field of polymer processing a novel in-house filament stretching rheometer was developed. The rheometer allows to perform time resolved measurements while locally controlling the uniaxial extensional deformation. In Chapter 2 this setup is described and preliminary in-situ X-ray experiments, performed at ESRF in Grenoble, prove the enormous capability of the rheometer by opening new possibilities in the field of flow induced crystallization.

In Chapter 3 the in-house developed rheometer is used to investigate the extensional flow induced crystallization of a low density polyethylene (LDPE), a long chain branched semicrystalline thermoplastic, of which very little is known about its flow induced crystallization. Time-resolved X-ray experiments were performed at the European Synchrotron in Grenoble, where, systematically, the effect of strain and strain rate at constant temperature on the orientation and structure formation have been investigated.

To investigate the jetting performance of highly viscous fluids a setup has been developed and described in Chapter 4. A new generation dispensing system, that allows to process high viscosity fluids, has been employed and was combined with an optical system to visually follow the jetting and droplet deposition process. A systematic study of the jetting parameters such as nozzle to substrate distance and viscosity has been performed and their impact on dispensing mechanism, process resolution and productivity is investigated. As model material, polydimethylsiloxane (PDMS) has been used.

In Chapter 5 a more focused research has been dedicated to the substrate nature and thus the effect that material - substrate contact properties have on the jetting process. Experiments with PDMS on substrates with different static contact angles and surface roughness have been performed employing the setup developed in the previous chapter.

Chapter 6 presents the final conclusions and recommendations for future research.

CHAPTER 2

A filament stretching rheometer for *in-situ* X-ray experiments: combining rheology and *in-situ* crystalline morphology characterization

Abstract

We present a rheometer that combines the possibility to perform *in-situ* X-ray experiments with a precise and locally controlled uniaxial extensional flow. It thus allows to study the crystallization kinetics and morphology evolution combined with the rheological response to the applied flow field. A constant uniaxial deformation rate is ensured thanks to a fast control scheme that drives the simultaneous movement of the top and bottom plate during a pulling experiment. A laser micrometer measures the time evolution of the smallest diameter, where the highest stress is concentrated. The rheometer has a copper temperature-controlled oven with the ability to reach 250°C and a N_2 connection to create an inert atmosphere during the experiments. The innovation of our rheometer is the fixed location of the midfilament position, which is possible because of the simultaneous controlled movement of the two end plates. The copper oven has been constructed with four ad-hoc windows: two glass windows for laser access and two kapton windows for X-ray access. The key feature is the ability to perfectly align the midfilament of the sample to the laser micrometer and to the incoming X-ray beam in a synchrotron radiation facility, making it possible to investigate structure and morphologies developed during extensional flow. The rheological response measured with our rheometer for LDPE is in agreement with the linear viscoelastic envelope and with the results obtained from existing extensional rheometers. To demonstrate the capability of the instrument we have performed *in-situ* -resolved X-ray experiments on low-density polyethylene (LDPE) samples exhibiting extensional flow-induced crystallization.

Largely reproduced from:
Pepe, J., Cleven, L.C., Suijkerbuijk, E.J., Dekkers, E.C., Hermida-Merino, D., Cardinaels, R., Peters, G.W. and Anderson, P.D., 2020. A filament stretching rheometer for in situ X-ray experiments: Combining rheology and crystalline morphology characterization. *Review of Scientific Instruments, 91(7).*

2.1 Introduction

Nowadays, polymers, and in particular thermoplastics, are widely used materials in the manufacturing industry, thanks to their relatively low price, good processability and wide range of achievable properties. Despite these favorable aspects polymers are quite elaborate molecules and, as a consequence their response to the thermo-mechanical history experienced during processing is not only complex, but also different from one polymer to the other. During processing, using techniques ranging from the most consolidated ones, like extrusion, injection molding, blow molding and fiber spinning, to the emerging ones such as filament fused deposition modeling (FDM) and inkjet printing, polymers are subjected to various flow fields, consisting of both shear and extensional contributions. For semi-crystalline materials the presence of flow largely affects the kinetics as well as formed crystal morphologies and structures [11, 12, 13] which in turn affect the final properties (e.g. mechanical, optical, barrier, piezoelectrical) [14, 15, 16]. It is well-established that the most common crystalline morphology developed during strong flows is the so called "shish-kebab" consisting of: extended crystal chains oriented in the direction of the flow (shish), and folded chain lamellae in the opposite direction (kebab) [11]. Shear-induced crystallization has received substantial attention since decades[17]. Thereto, several innovative setups and modifications of existing setups that allow *in-situ* crystallization studies have been developed. These devices were combined with various *in-situ* structure characterization techniques, like birefringence [18, 19, 20, 21], optical imaging [22, 23], X-ray scattering and diffraction (SAXS, WAXD) [11, 24, 25, 26, 27, 28]. In the context of flow-induced crystallization time resolved X-ray experiments are the most popular technique to resolve the structure evolution during processing [29, 30, 31, 32, 33, 34].

Despite the extreme importance of extensional flow in polymer processing, very little is known about the material response to an extensional flow and even less is known about extensional flow-induced crystallization. This is because the implementation of an ideal uniaxial extensional deformation is still an experimental challenge and there is a lack of suitable devices for the application of uniaxial extensional flow combined with *in-situ* characterizations. Nevertheless several studies have been conducted in order to understand the role of extensional flow in the crystallization process [35, 36, 37, 38, 39, 40, 41, 42, 43, 44, 45, 46, 47, 48, 49, 50]. They use different devices that either generate a precise and locally controlled uniaxial extension resulting in accurate rheological data without *in-situ* access to the microstructure [36, 37, 38, 39, 40, 41, 42, 43, 44], or they facilitate *in-situ* structure characterization whereas the deformation field undergone by the material is less well controlled [35, 45, 46, 47, 48, 49, 50]. In the former category a commercial (VADER 1000) and a home-built filament stretching rheometer have been used, to study the extensional flow-induced crystallization of a commercial low-density polyethylene (LDPE) and an isotactic polypropylene (iPP) respectively [41, 43, 44]. The filament stretching rheometer is a powerful and versatile tool to investigate the extensional rheology of complex fluids with a wide range of viscosities and makes it possible to reach high strains. It mainly consists of two plates, of which one moves, thereby stretching the fluid in between. The most important feature of this type of device is its ability to keep the deformation rate at the midfilament point constant, leading to an

ideal uniaxial extensional flow. In both devices only the upper plate moves causing a shift of the middle point position over time, that allows only for structure characterization via post-mortem *ex-situ* X-ray experiments. In the second category, apart from cross-slot flow cells [45, 46, 47], a home-built double-drum windup device allows for *in-situ* X-ray characterization during extension and has been tested on poly(ethylene oxide), poly(1-butene) and a commercial iPP [35, 48, 49, 50]. This rheometer has two counter-rotating drums as in the Sentmanat extensional add-on for commercial shear rheometers (SER) [51] with improved design to reduce polymer sagging and to homogenize the temperature. However this type of rheometer is limited in the Hencky strain values that can be reached and it does not allow for local strain (rate) measurements or control. A homogeneous deformation is assumed, which is however not always the case, especially at large values of the Hencky strain, as shown in the study of McCready et al. [52] on pre-aligned cylindrical block copolymer melts.

In the current work we present, for the first time to our knowledge, a rheometer that combines the possibility to perform *in-situ* X-ray characterization whilst the material undergoes a precise and locally controlled uniaxial extensional flow. The general design of the rheometer is based on existing filament stretching rheometers [53, 54, 55, 56], but differs from that of similar devices in its ability to perform *in-situ* experiments while locally controlling the deformation. To fulfill this purpose the design of the rheometer ensures the stationary position of the midfilament point allowing precise alignment of it to the X-ray source. An electrically heated oven is built to control the temperature and degradation is avoided using nitrogen gas. Studies of polymer crystallization, combining scattering (SAXS) and diffraction (WAXD) techniques, with this device will allow us to develop an understanding of the extensional flow-induced crystallization process.

2.2 Rheometer design and description

Figure 2.1 shows the rheometer combined with SAXS/WAXD measurements, as arranged in the beamline.

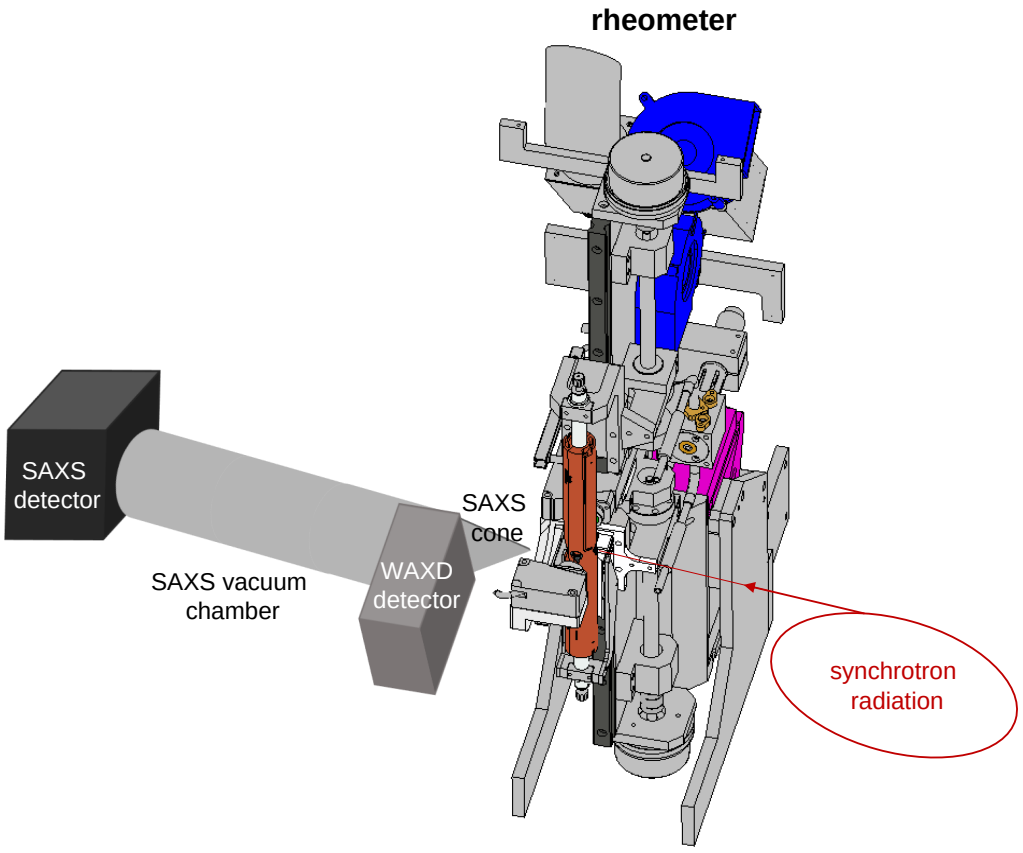

Figure 2.1: Schematic of the experimental setup with *in-situ* X-ray capability, as placed in the ESRF beamline.

The rheometer is constructed with two end plates that move simultaneously and at the same velocity (Figure 2.2 (a)), the latter being controlled to create an ideal uniaxial extensional deformation. In an ideal uniaxial extensional flow at a constant strain rate, the length increases and the diameter decreases exponentially in time. To control the deformation at the midpoint the diameter is constantly measured by a laser micrometer and its value serves as input for a closed control loop. The simultaneous movement of the plates is realized by two motors driven by two ball screws that are independently controlled. The response of the material to the deformation is measured by a load cell connected to the bottom plate. An *ad-hoc* copper oven allows for high-temperature experiments in an inert environment, and enables access for the laser micrometer and the X-ray source. The four windows, two for the laser and two for the X-rays Figure (2.2 (c)), are aligned with respect to each other with an accuracy of ± 50 μm, ensuring a precise alignment of the midfilament point to the laser and subsequently to the X-ray beam, as will be described in detailed later. Figure 2.2 (b) and Figure 2.2 (d) show the rheometer with the main components indicated. The overall programming and controlling of the filament stretching rheometer is done with MATLAB® Simulink. The RTI1104 DSpace® card is the real time control platform that runs the model created in Simulink, while DSpace® ControlDesk software provides a user interface to interactively

work with the model. The main components and features are described in more detail in the following sections.

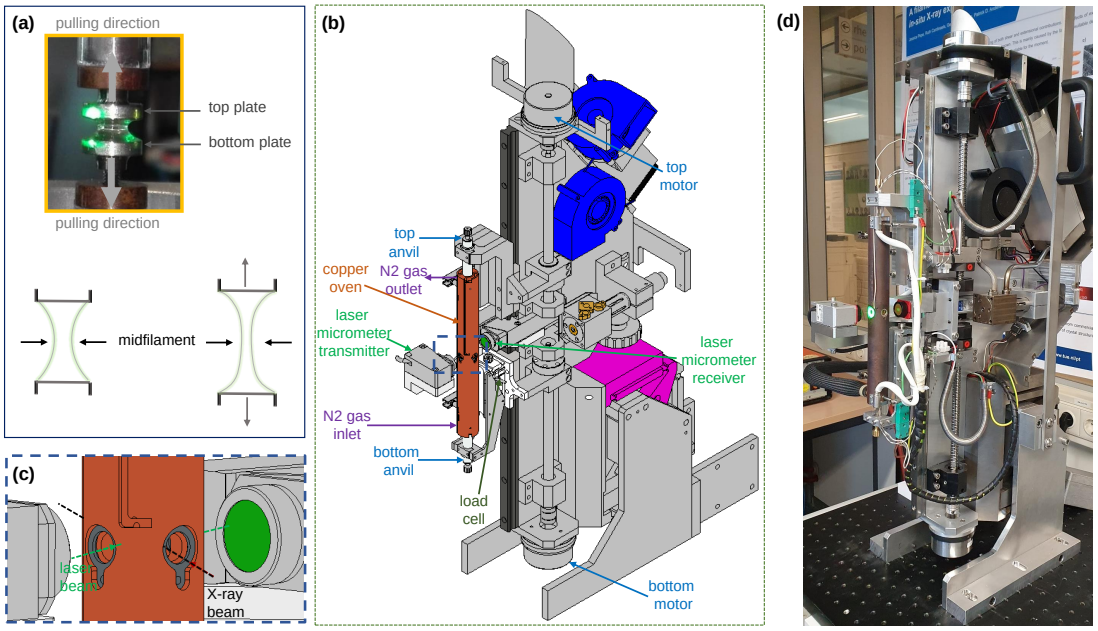

Figure 2.2: (a) Picture of a pre-stretched sample between top and bottom plate, pulling direction is indicated by the arrows and schematic of the diameter evolution with the midfilament point stationary in time. (b) 3D drawing of the in-house developed filament stretching rheometer. (c) Zoomed-in view of the oven showing the alignment of the four windows and the direction of the laser and the X-ray beam. (d) Photograph of the device.

2.2.1 Motion control and force measurement

The top and bottom stainless steel plates are connected to two pistons thanks to their threaded body. Hence it is possible to use, and easily interchange plates of different diameters, materials and geometries, which allows to increase the contact between the sample and the plates in case slip-off occurs [44]. Each piston consists of two main components, a copper plate holder in which the plates are screwed and a quartz tube that accommodates the plate holder itself, the heating element and the thermocouple used to heat and control the temperature of the plates, respectively, as shown in Figure 2.3. The low thermal expansion coefficient of quartz ensures minimum changes in length and thus minimum changes in the position of the plates.

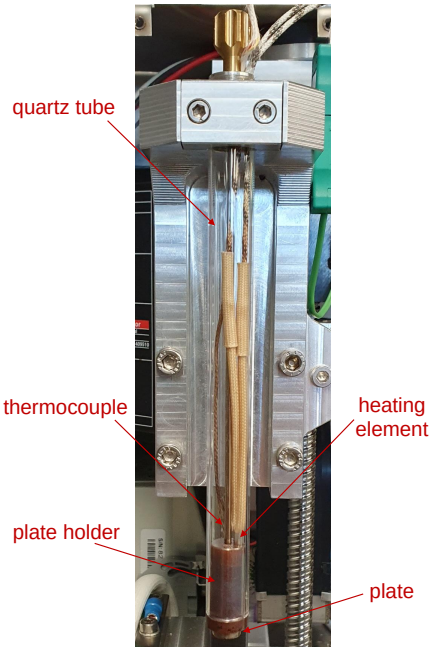

Figure 2.3: Photograph of the piston with its components indicated.

The pistons are mounted and connected to a preloaded linear profile guide that is linked by ball screws to the motors. The maximum distance achievable between the plates is 145 mm. When the oven is used, this distance is reduced to 114 mm to assure that the pistons always remain inside the oven, throughout the experiment. The motors that drive the guides are EC Maxon motors, with a maximum speed of 3740 rpm, which corresponds to a maximum linear movement of 623.3 mm/s for a single axis, while the minimum speed is 0.001 mm/s. The motors are externally controlled by a servocontroller, an encoder provides the electrical signal that is used for speed control. The sampling time of the speed controller is 200 μs.

The axial force on the bottom plate during the uniaxial experiment is measured by a load cell HBM U9C of 100N maximum nominal force. The load cell housing is designed as such that different cells can easily be interchanged (i.e. to measure lower viscous samples). In particular 2N and 20N (XFTC300) load cells are available. The load cell has been calibrated both in compression, by placing known weights on it, and in tension, by pulling, at constant rate, a metallic spring of which the elastic constant k is known. The calibration indicated that the minimum value measurable by the 100N load cell is 0.02 N with a noise level of $\pm$0.01 N. Furthermore it was verified that the contribution of the acceleration from the moving components to the total force measured during an experiment is negligible. The load cell is placed outside the oven to ensure that no increase of its temperature occurs during the experiments.

At the center of the oven there are two flat quartz windows providing optical access for the head and receiver of the KEYENCE LS-9006 laser micrometer, thereby allowing it to measure the diameter of the sample during the experiment. Because the middle point location of the polymer is fixed, the laser, mounted on an aluminum support, is aligned to

the oven quartz windows and, thus, to the midfilament point. The measurable diameter ranges from 0.04 mm to 6 mm, with an accuracy of ± 0.5 µm. For a typical initial sample diameter $D = 5$ mm and height $L = 1.5$ mm, the combination of laser micrometer range and motor speed results in a maximum Hencky strain of 9 and extension rates ranging from 0.00001 s^{-1} to 5 s^{-1}. The aluminum support on which the laser is mounted allows to dissipate the heat generated from the laser itself and to keep it within its operating temperature range. The laser micrometer not only measures the diameter but also shows video images of the measured area (over a filament height of 1.6 mm), allowing to verify the location of the minimum diameter.

2.2.2 Oven

Around the pistons a cylindrical copper oven is constructed to control the temperature and to create an inert atmosphere, and its design is crucial for the success of the *in-situ* X-ray experiments. The copper oven is designed as a double wall cylinder with an external diameter $D_e = 38$ mm and an internal diameter $D_i = 13$ mm. Copper is chosen as construction material because of its high-thermal conductivity and because it can easily be shaped. Dimensional choices are restricted by the requirements of good temperature control, minimal amount of air around the sample to minimize the scattering background, and correct placement of the rheometer in the beamline. The internal diameter has been chosen as the minimum possible value in order to reduce the gap between the quartz tube and the copper oven, and to minimize the scattering background coming from the air. The outer diameter is the optimal compromise between design limitations and the beamline requirements of placing the rheometer as close as possible to the incoming tube of the X-ray source and to the SAXS cone to reduce the background scattering. In order to allow an X-ray beam to access the oven and to collect all the diffraction and scattering patterns from the polymer two Kapton windows of 0.05 mm thick have been designed as shown in Figure 2.4 (b). Kapton is the material of choice because, being amorphous, it is free of strong diffraction peaks and it does not show lamellar scattering in the q-range of our interest. The inlet window for the X-ray beam has a diameter of 6 mm, similar as the two quartz windows for the laser access. The window for the outlet of the X-ray beam has been realized with an intrusive angle of 90° facilitating diffraction angles (2θ) of most polymeric materials.

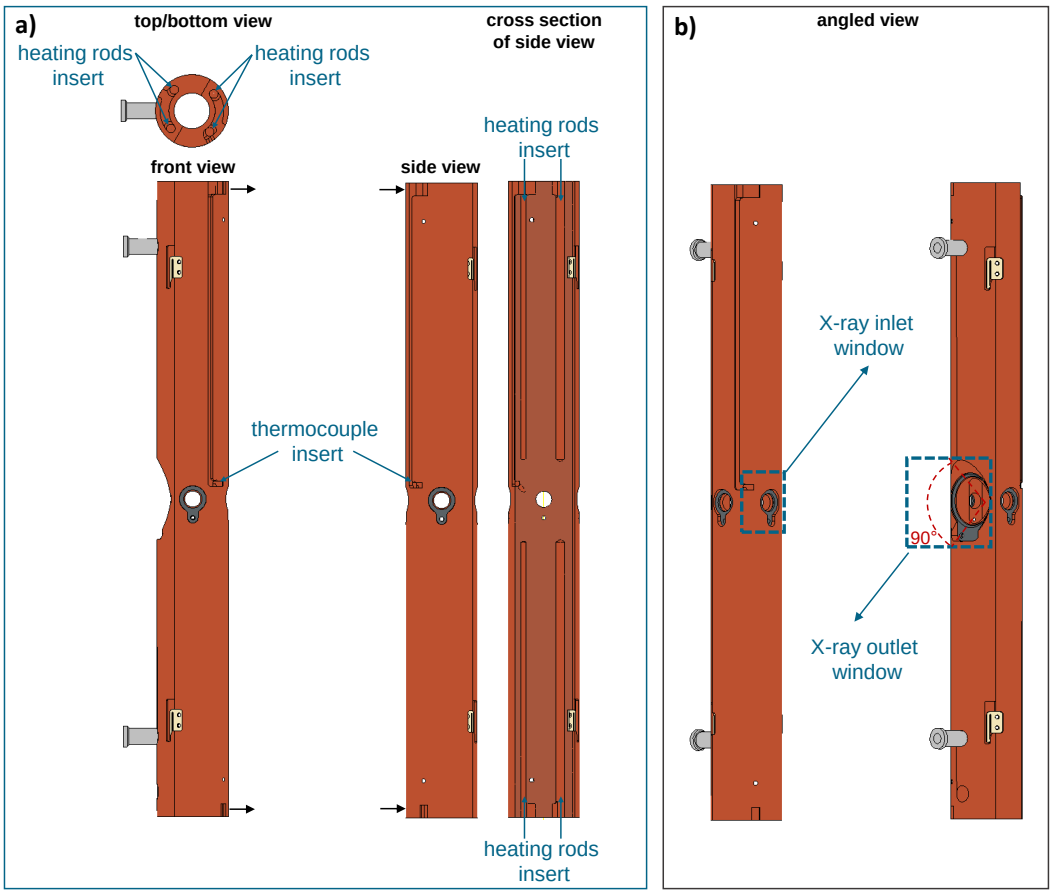

Figure 2.4: Technical drawing of the oven. (a) Top/bottom, front and side views with thermal insert. Cross-section and top/bottom view show the heating inserts. (b) Angled view of the inlet and outlet windows for the X-rays.

Eight heating rods with a power of 100 W each, four on the top and four at the bottom equally distributed on all sides in the oven walls, regulate the temperature of the oven Figure (2.4 (a)). In order to avoid degradation of the polymer because of the high temperatures involved, nitrogen gas (at a pressure of 1 bar) continuously flows from the bottom through the oven keeping the environment inert and helping in reducing temperature gradients. The nitrogen gas is externally preheated using a 400 W heating cartridge regulated by a thermocouple and Hasco power supply unit. The heat is transferred to the polymer from the plates by conduction and from the heated nitrogen in the oven by convection. The temperature is measured and controlled at three points: at the top, and bottom plate and in the oven wall at the center of the oven, where K-type thermocouples (RS Pro, ±1 °C accuracy) are integrated. Three feedback loops regulate the temperature of the plates and of the oven using the three independently measured temperatures as input values. Each loop contains a PI controller. The temperature of the sample at the middle point has been checked with an external thermocouple, of the same type as mentioned before and placed directly into the polymer. The measured temperature offset from the set point is 5°C (corrected for during the experiments) and the maximum achievable temperature is 250 °C. The heating and cooling rate are fixed, and approximately 100°C/min and 4°C/min, respectively. There is an overshoot of 2°C

and the oscillations around the set point are ±0.5°C. We chose to not cover the copper oven with an insulation shield because the presence of insulation would enormously increase the cooling time, which is extremely undesired for flow-induced crystallization experiments.

2.2.3 Control scheme implementation

In this type of rheometer a perfect uniaxial extensional deformation is not achievable throughout the filament because of the presence of the rigid plates. The contact with the end plates results in deviations from a cylindrical shape due to which the average and local extension rates differ from each other. In early version of filament stretching rheometers, a locally constant uniaxial extension rate was accomplished by determining the plate speed evolution via trial-and-error, which gave good control for polymer solutions [53, 57]. When using polymer melts the implementation of open control loops becomes a tedious process due to the dependence of the material rheology on the strain rate [58]. Previous works show that by means of an active real time control of the diameter evolution at the midfilament point, it is possible to impose, locally, a deformation at constant rate and thus to achieve an ideal uniaxial extensional flow [58, 59]. The most successful way to perform such experiments is to implement a closed control loop and the most robust algorithm available at present for controlling the kinematics of a filament stretching rheometer is the one proposed by Marín et al. [58]. The working principle of this control scheme is schematically depicted in Figure 2.5.

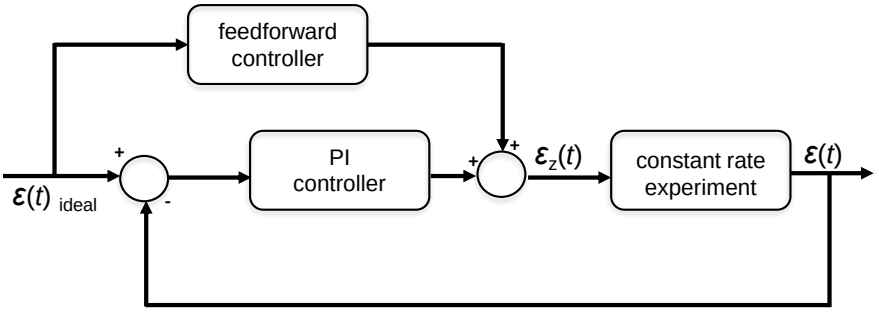

Figure 2.5: Schematic of the control scheme.

In the control loop the Hencky strain based on diameter (ϵ) is the controlled variable:

$$\epsilon = -2\ln\left(\frac{D(t)}{D_0}\right), \tag{2.1}$$

while the strain based on the distance (ϵ_z) between plates is the actuated variable:

$$\epsilon_z = \ln\left(\frac{L(t)}{L_0}\right). \tag{2.2}$$

A combination of a PI (proportional/integral) feedback and a feed-forward control is used to act on ϵ_z to control ϵ. Hence the evolution of the diameter over time is controlled by changing the plate separation velocity profile accordingly. The governing equations are the following[58]:

$$\epsilon_z(i+1) = \epsilon_z(i) + \Delta{\epsilon_z}^{ff}(i) + K_p[\delta\epsilon(i) - \delta\epsilon(i-1)] + K_i\Delta t[\delta\epsilon(i)], \tag{2.3}$$

where $\delta\epsilon$ is the error and $\Delta{\epsilon_z}^{ff}$ is the feed-forward contribution calculated as:

$$\delta\epsilon(i) = 2\ln\left(\frac{D(i)}{D_{ideal}(i)}\right), \tag{2.4}$$

$$\Delta{\epsilon_z}^{ff}(i) = f(\epsilon(i+1)) - f(\epsilon(i)), \tag{2.5}$$

where D_{ideal} is the the desired diameter and $f(\epsilon)$ describes the kinematic curve (i.e. the relation between the extent of separation between the end plates and the midfilament diameter) with the following function:

$$f(\epsilon) = \frac{\alpha\epsilon d}{\alpha\epsilon + d}, \tag{2.6}$$

wherein the values of the parameters are $\alpha = 1$ and $d = 2.5$ [58]. The actuation time of the system (Δt) is 200 μs. After tuning the proportional and integral gain (K_p and K_i, respectively) of the feedback controller the optimal values found were K_p=0 and K_i=2.5 s^{-1}, in agreement with the values from literature [58]. This results in a deviation from the ideal diameter ranging from approximately 2% at low rates to approximately 15% at strain rates as high as 1 s^{-1}. By increasing the integral gain it is possible to reduce the error and to increase the maximum strain rate at which a successful experiment with closed loop control can be performed. In particular at a value of K_i=12.5 s^{-1} experiments up to $\dot{\epsilon}$=2.5 s^{-1} are possible. All the experiments shown in this paper are performed with a value of 0 for the proportional gain and 2.5 s^{-1} for the integral gain. Switching off the control loop allows to achieve higher overall strain rates, albeit without control over their local value. More details on the control scheme can be found in the paper of Marín et al. [58].

2.2.4 Beamline setup

Time-resolved X-ray experiments have been performed at the Dutch-Belgian beamline (DUBBLE) at the European Synchrotron Radiation Facility (ESRF). Figure 2.6 shows the beamline setup.

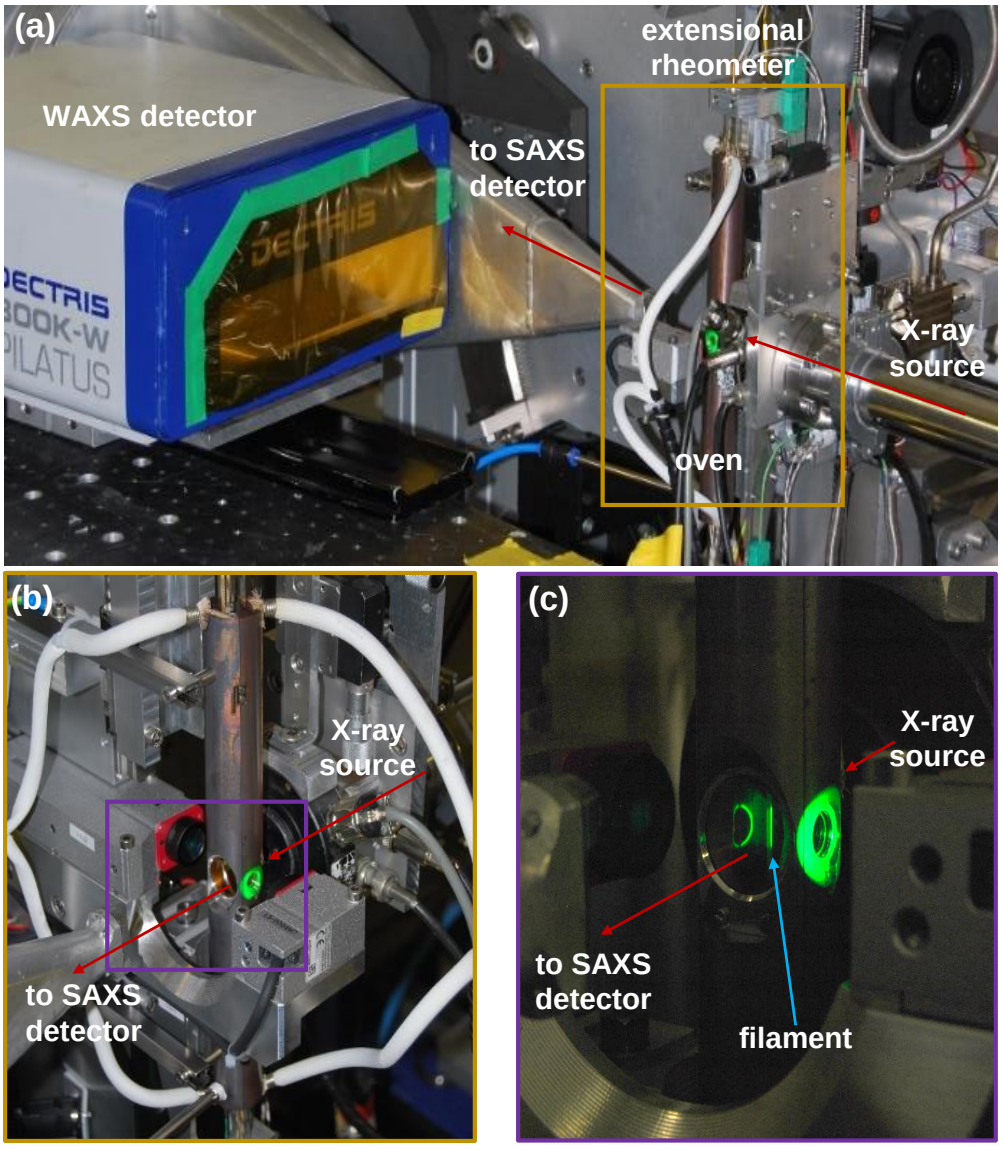

Figure 2.6: (a) Experimental setup in the beamline BM26 at ESRF. (b) Close view of the alignment between the oven and the SAXS cone. (c) View of the filament after stretching and complete crystallization.

To allow alignment with respect to the incoming X-ray beam the rheometer is mounted on a system of linear translation stages. For the movements in x and y direction a Huber stage 5102.20 is used. The travel range of the motor is ± 15 mm and it has a minimal incremental step of 0.1 mm. The z translation stage is a Huber 5103.A20-90 with a travel range of 90 mm and resolution of 0.05 μm. The wavelength of the X-ray beam is 1.0408 Å, and a beam size of 300 μm x 300 μm is obtained by chopping the standard beam. This size is smaller than the minimum value of the diameter reached during the experiments. During and after extensional flow X-ray scattering (SAXS) and wide angle X-ray diffraction (WAXD) measurements have been performed using, simultaneously, a Pilatus 1M detector (981 x 1043 pixels of 172 μm x 172 μm placed at a distance of 3.432 m) and a Pilatus 300K detector (1472 x 195 pixels of 172 μm x 172 μm placed at a distance of 0.297 m), respectively. The distance and tilt angle were calibrated

using AgBe (silver behenate) for the SAXS detector and Al_2O_3 (aluminum oxide) for the WAXD detector. A mask was applied to remove any trace of the beam stop and direct beam from the acquired images that were further corrected for the background and the decrease of the diameter during the experiments [60]. The starting of the SAXS/WAXD acquisition was triggered by an electric TTL pulse send by the rheometer to avoid any time discrepancy. A combination of a fast and a slow acquisition was used to collect both SAXS and WAXD patterns for a total acquisition time of 30 min (1800s). The fast acquisition mode was used in the first 60 s of the experiments and carried out with an exposure time of 0.5 s. For the remaining 1740 s the slow acquisition mode was used, and an exposure time of 5 s was chosen. Detailed information regarding the acquisition procedure can be found in Table 2.1. SAXS and WAXD data were analyzed using the software Fit2D [61] developed by the European Synchrotron Radiation Facility.

Table 2.1: Acquisition protocol.

acquisition time [s]	exposure time [s]	delay [s]
60	0.5	-
60	5	-
600	5	25
1080	5	55

2.3 Experimental procedure

2.3.1 Sample preparation

To validate the performance of the rheometer, experiments on a low-density polyethylene (LDPE) (LD 150BW, ExxonMobil) have been carried out. The peak melting temperature (T_m) of this LDPE is around 112°C, as determined by differential scanning calorimetry (DSC) at a heating rate of 5°C/min. The samples used in our experiments are small LDPE cylinders of 6 mm diameter and 1.5 mm thickness obtained by means of hot compression molding. A rectangular mold was filled with LDPE pellets, heated to 180°C and held at this temperature for 5 min. Subsequently a force of 250 kN was applied and held for 6 min allowing the molten polymer to be shaped between the two hot plates. After cooling to room temperature, samples of the desired dimensions were punched out of the polymer sheet. A schematic of the procedure for the extensional rheology experiments is shown in Figure 2.7. The compression molded sample is placed on the bottom plate allowing for melting. The plates are then moved close to each other, thereby slightly compressing the molten polymer to ensure attachment to both plates before surface tension effects become predominant. The sample is held in between the plates for a sufficient time allowing relaxation and homogenization of the temperature. Subsequently, the material is slowly prestretched to a desired midfilament diameter value and its complete relaxation. During this procedure a small flow could be present due to the interfacial tension and viscoelastic relaxation of the material, causing a small decrease of the filament diameter. Moreover, depending on the viscosity of the material,

the height of the midpoint could shift to a lower position because of gravitational effects. Both phenomena are visible on the real time video images from the laser micrometer, thus making it possible to realign the midpoint to the center of the laser by moving both plates simultaneously in the same direction. The midpoint position during both the prestretch and the experiment is constantly monitored, indicating a fixed position for all the experiments performed in this work. In the rest of the manuscript we will refer to $\Lambda_i = L_i/D_i$ as the initial aspect ratio of the compression molded sample, $\Lambda_c = L_c/D_c$ as the aspect ratio prior to the prestretch and L_0 and D_0 as the values right before starting the experiment, of the length L (distance between the plates) and the midfilament diameter D (measured with the laser micrometer) that will be used in the control loop as initial conditions.

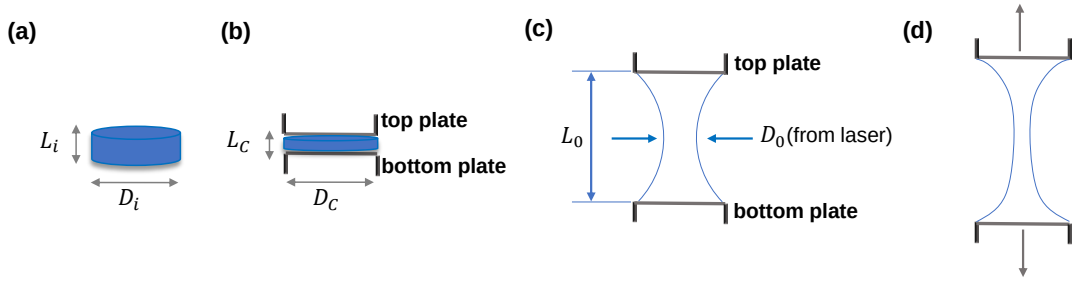

Figure 2.7: Schematic of the experimental procedure. (a) Preparation of the sample by compression molding. (b) Melting and attachment to the end plates, by slight compression. (c) Prestretching. (d) Controlled uniaxial deformation.

2.3.2 Linear viscoelasticity

The material response to extensional flow is different from the one in simple shear. This is because extensional flow is irrotational and, therefore, it can induce much stronger orientation and stretching of the macromolecules. In a uniaxial extensional deformation the material function of interest is the transient extensional viscosity that is a function of the extension rate, time and temperature. For viscoelastic fluids after startup of the flow only in the limit of very low extension rates the transient extensional viscosity approaches three times the transient shear viscosity, thereby defining the linear viscoelastic envelope (LVE) [62]. At higher strain rates, for branched polymers as LDPE, the extensional viscosity deviates upwards from the LVE, and this phenomenon is known as "strain hardening" [55, 59, 63]. The linear viscoelastic behavior of the LDPE was determined using small amplitude oscillatory shear (SAOS) measurements. A 25 mm plate-plate geometry was mounted on an ARES rheometer with a convection oven using a nitrogen flux and experiments at four different temperatures, between 130°C and 190°C, were performed at 2% strain. The data were shifted to a master curve at the reference temperature of 150°C using time-temperature-superposition (TTS) (Figure 2.8 (a)). The shift factors (Figure 2.8 (b)) were fitted with the Arrhenius equation [64]:

$$a_T = \exp\left[\frac{E_a}{R}\left(\frac{1}{T} - \frac{1}{T_{ref}}\right)\right]. \tag{2.7}$$

In the above equation the fitting parameter is the activation energy E_a, R is the universal gas constant, T the temperature and T_{ref} the reference temperature. Good agreement between the fitting and the experimental shift factors is found for a value of E_a of 65.7 kJ/mol, which is in agreement with literature values for a different LDPE grade [65].

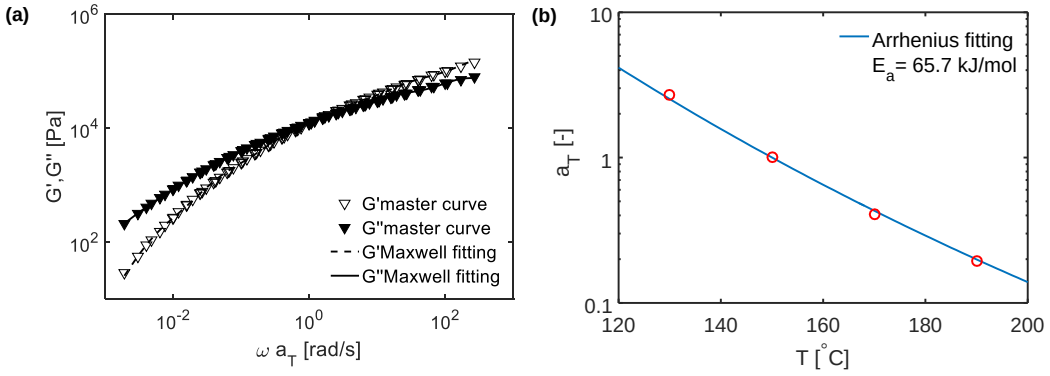

Figure 2.8: (a) Master curve of storage modulus G′ (open symbols) and loss modulus G″ (filled symbols) at the reference temperature of 150°C and multi-mode Maxwell model fitting (dashed and continuous lines). (b) Time-temperature shift factors (open symbols) and Arrhenius fitting.

A multi-mode Maxwell model was fitted on the dynamic moduli to obtain the linear viscoelastic relaxation spectrum. This model is constructed by placing n modes in parallel, whereby each mode (a spring and a dashpot connected in series) models a viscoelastic contribution of the polymer. The relaxation times and corresponding plateau moduli for LDPE are given in Table 2.2.

Table 2.2: Relaxation spectrum for LDPE at 150°C.

mode	τ_i [s]	G_i [Pa]
1	0.00406	$1.44{\cdot}10^5$
2	0.0461	$4.85{\cdot}10^4$
3	0.386	$2.09{\cdot}10^4$
4	3.04	$7.46{\cdot}10^3$
5	22.7	$1.84{\cdot}10^3$
6	170	224

2.3.3 Experimental procedure for *in-situ* X-ray experiments

To perform *in-situ* structure characterization experiments it is important that the midfilament point is perfectly aligned with the X-ray beam. After the polymer has been prestretched, the temperature is lowered to the desired experimental value. Before the temperature reaches the set point an X-ray scan is performed by moving the rheometer along the x- and z- direction, allowing the material, during this aligning procedure, to achieve the experimental temperature. During this process the reduction

of the minimum diameter was negligible (around 2%). The transmitted beam intensity collected at the photo-diode is used to evaluate the coordinates of the midfilament point. Figure 2.9 (a) illustrates the alignment method.

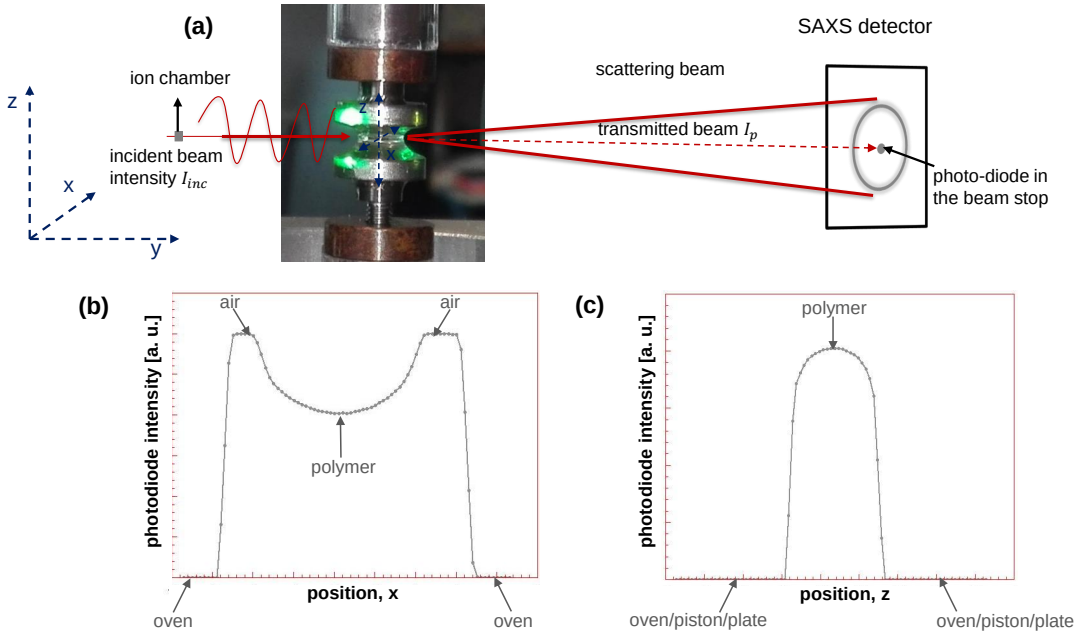

Figure 2.9: (a) Schematic of the scanning procedure to find the midfilament point. (b) Photo-diode intensity profile in horizontal direction. (c) Photo-diode intensity profile in vertical direction.

When scanning along the x-direction (i.e. along the width of the sample) the metal of the oven initially absorbs the complete intensity received, as a consequence no intensity is transmitted to the photo-diode. Moving further the intensity suddenly reaches a maximum, corresponding to the air present in the oven. A subsequent decrease of the transmission marks the presence of the polymer which absorbs part of the intensity proportionally to its thickness. The minimum in the intensity profile at the photo-diode corresponds to the center of the polymer, the profile is symmetric because of the geometry of the prestretched sample. While scanning along the z-direction (i.e. along the height of the sample) the photo-diode intensity is only different from zero when the X-rays pass through the polymer and the intensity shows a maximum at the midfilament region where the thickness is the lowest. Figure 2.9 (b) and Figure 2.9 (c) show the transmitted intensity profile, as measured with the photo-diode, as a function of the scanning position. This procedure allows to precisely identify the midfilament point and to align it to the X-ray beam source. A quiescent experiment (no flow applied after the prestretch) has been performed prior to the flow experiment to determine the time window for the temperature stabilization and scanning procedure before the polymer starts to crystallize. In quiescent conditions the crystallization starts around 200 s after the completion of thermal homogenization and alignment. The scanning procedure takes less than 5 minutes during which, SAXS/WAXD patterns of the midfilament region have been acquired to check that the material remains amorphous.

2.4 Results and discussion

2.4.1 Control scheme and melt rheology validation

To demonstrate the capability of our rheometer to locally control the deformation, the implementation of the control scheme was validated by performing experiments at different flow conditions. Figure Figure 2.10 (a) demonstrates that the laser measurement effectively occurs at the point of minimum diameter. In Figure 2.10 (b) we report the evolution of the diameter in time in comparison with the ideal exponential decrease during representative experiments performed at strain rates of 0.1 s^{-1} and 1 s^{-1}, and a temperature of 150°C for an LDPE sample. 2.10 (c) shows the non-ideal relation between the strains in axial and radial directions.

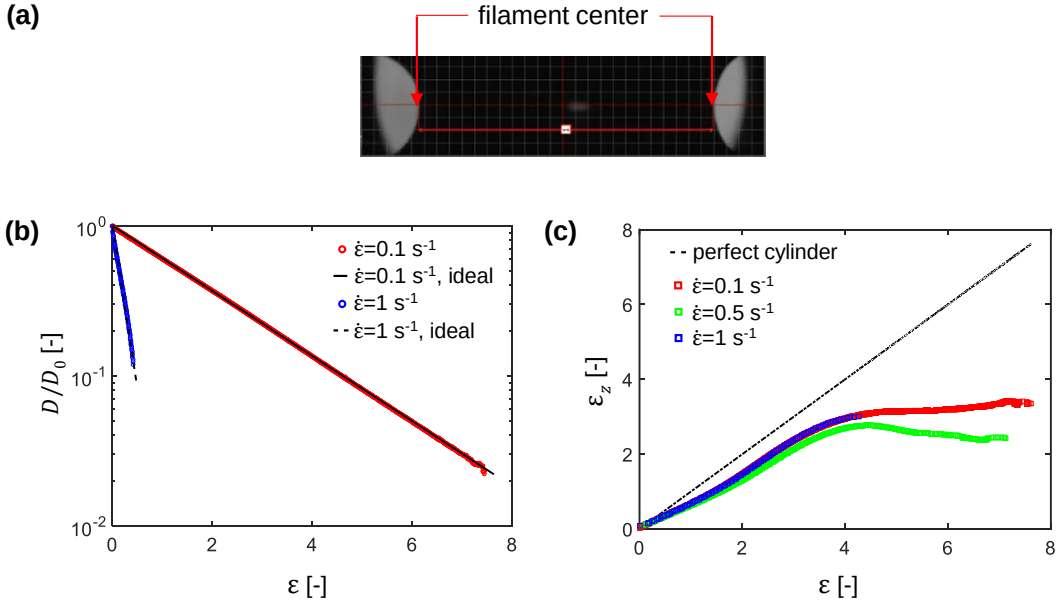

Figure 2.10: (a) Optical image of the area around the filament point. (b) Comparison of the evolution of the filament diameter with the ideal exponential thinning profile. (c) Kinematic curve for the evolution of the axial strain. Experiments with LDPE at a temperature of 150°C.

The transient extensional viscosity calculated from a force balance[66], and in absence of surface tension and inertia contributions, is defined as [54, 67]:

$$\eta_E^+ = \frac{F_z - 1/2mg}{\dot{\epsilon}\pi D^2/4}(\kappa_{\dot{\gamma}}). \tag{2.8}$$

In the above equation F_z is the axial force measured by the load cell, g is the gravitational acceleration, m the mass of the filament, D the diameter measured with the laser micrometer and $\dot{\epsilon}$ the strain rate. At the startup of the flow strong shear contributions

can be generated due to the pinning of the polymer at the end plates. The consequent radial pressure gradient adds an extra contribution to the axial force measured that can be compensated for by using a correction factor [68]:

$$\kappa_{\dot{\gamma}} = \left(1 + \frac{\exp(-7\,(\epsilon + \epsilon_{\mathrm{pre}}/3))}{3{\Lambda_{\mathrm{c}}}^2}\right)^{-1} \tag{2.9}$$

The above expression takes into account the amount of deformation that the polymer undergoes during the prestretch (ϵ_{pre}) and the aspect ratio prior to it (Λ_{c}). For large strains the shear contribution becomes negligible because of the reduction of the radial pressure gradients [69].

To test the validity of the rheological data, the extensional viscosity measured with our rheometer (rheoTU/e) has been compared with the linear viscoelastic envelope (LVE) and the extensional viscosity, measured at the same flow and temperature conditions, with a Sentmanat Extensional Rheometer (SER) setup mounted on an Anton Paar MCR502 with convection oven. The linear viscoelastic envelope is calculated from the following equation [62]:

$${\eta_{\mathrm{E}}}^{+} = 3\sum_{i} G_{\mathrm{i}}\tau_{\mathrm{i}}\left(1 - \exp\left(\frac{-t}{\tau_{\mathrm{i}}}\right)\right). \tag{2.10}$$

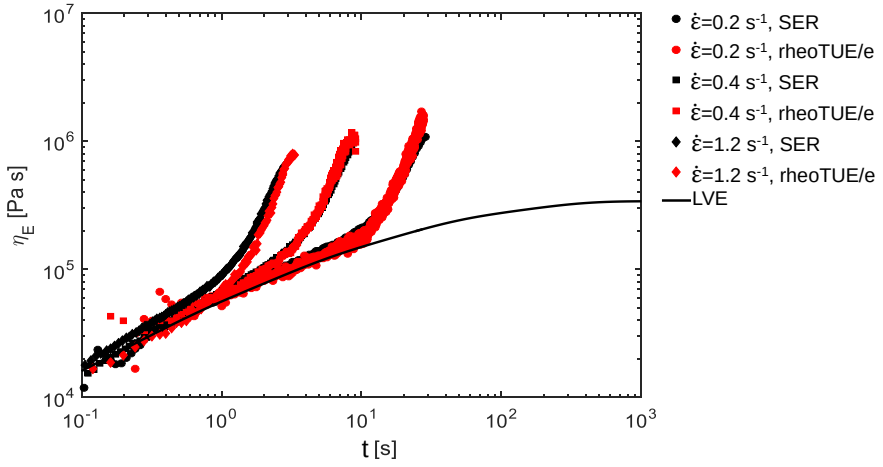

Figure 2.11: Measured extensional viscosity as a function of time for LDPE at 150°C at different strain rates, comparison with SER measurements and LVE envelope.

Figure 2.11 shows that the rheological response measured with our rheometer for LDPE is in nice agreement with the linear viscoelastic envelope (LVE) in the linear region and with data from the commercial device (SER) over the complete measurement range.

2.4.2 Combining rheology and *in-situ* SAXS/WAXD

To demonstrate the potential of our filament stretching rheometer for *in-situ* structure characterization, time-resolved X-ray experiments have been performed while applying a locally controlled deformation. A case study experiment is reported at 107°C, for a strain rate of 1.2 s^{-1} and final strain of 3.2. Figure 2.12 demonstrates that the crystallization kinetics, and the evolution of the crystal structure and morphology, during and after uniaxial extension, can be studied with our rheometer. The scattering patterns collected during flow (Figure 2.12 (a)) being characteristics of the shish-kebab evolution can be compared to the viscosity evolution, which is measured simultaneously. In the linear regime the polymer is amorphous and no scattering pattern is observed. When the viscosity deviates from the LVE envelope, streaks appear in the SAXS pattern in the direction perpendicular to the flow, indicating the formation of shish. Immediately after the shish form, and the deformation proceeds, lobes due to the scattering of crystal lamellae (kebabs) start to grow on top of the shish as is clearly visible from the increase of the scattered intensity in the direction of the flow.

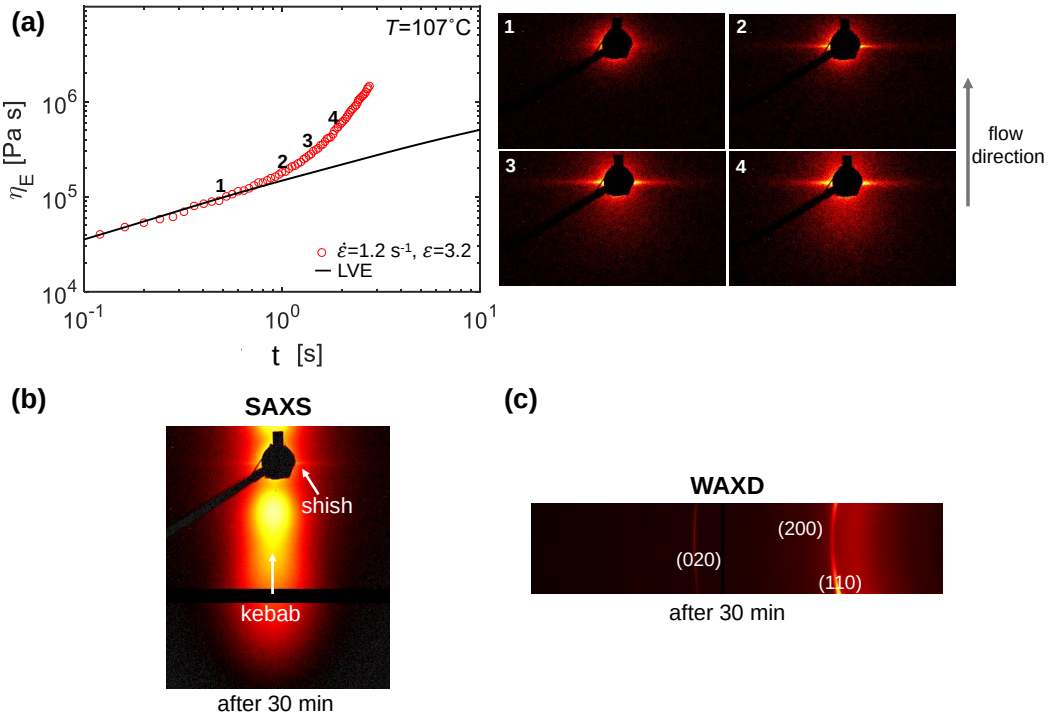

Figure 2.12: (a) Shish kebab morphology evolution and extensional rheology response during flow, at a strain rate of 1.2 s^{-1} and final Hencky strain of 3.2. (b) SAXS pattern and (c) 1D-WAXD pattern after cessation of flow and complete crystallization (after 30 min). The positions of shish, kebabs and of the characteristic crystal peaks of LDPE are indicated on the scattering and diffraction pattern, respectively.

To gain a better understanding of the changes in the morphology of the crystalline structures, an analysis of the intensity scattered at small angles was carried out. From the 2D-SAXS pattern two azimuthal regions can be identified. The equatorial (centered

at ϕ=0°), and meridional (centered at ϕ=90°) (Figure 2.13 (a)), where scattering of respectively shish and kebabs occurs. To obtain the time evolution of the intensity the 2D-SAXS pattern was integrated azimuthally in both regions according to:

$$I_{\mathrm{SAXS}} = \int_{q_{\min}}^{q_{\max}} \int_{\phi_{\min}}^{\phi_{\max}} I(\phi, q)\, d\phi\, dq, \tag{2.11}$$

where $q_{\min}$ and $q_{\max}$ are the minimum and maximum values of the scattering vector experimentally accessible, $\phi_{\min}$ and $\phi_{\max}$ are the minimum and maximum value of the azimuthal angle (for the meridional region $\phi_{\min}$=45° and $\phi_{\max}$=135°, for the equatorial region $\phi_{\min}$=-15° and $\phi_{\max}$=20°. Because the beam stop is not perfectly aligned to the shish position, the integration area of the equatorial region results to be asymmetrical). The intensities of the kebab (flow experiment) and of the spherulites (quiescent experiment) have been corrected with the Lorentz factor for a 2D and 3D object respectively [70]. The time evolution of the SAXS meridional and equatorial intensity is reported in Figure 2.13. The intensities are normalized with respect to the corresponding maximum values (to allow a more clear comparison of the trends in Figure 2.13 (b)). The kebabs intensity is compared with the scattered intensity under quiescent conditions. As expected flow has two main effects on the crystallization process. Firstly, it enhances the crystallization rate, an effect which is noticeable from the earlier onset of crystallization and the quasi-plateau reached in the meridional intensity curve compared to the quiescent case. Secondly, it modifies the crystallization kinetics changing the shape of the intensity curve versus time, due to the development of highly oriented structures. Furthermore it can be observed that the equatorial intensity (shish) grows much faster during flow as compared to the meridional one (kebab) and it shows an unusual maximum followed by a decrease over time. We believe that this phenomenon is caused by the nature of the SAXS technique itself. The scattered intensity indicates the deviation of the local electron density from the average electron density in the irradiated volume [71], as a consequence, when kebabs start to grow very fast they take over the shish on the scattering pattern causing, because of the electron density difference, an apparent decrease of the equatorial intensity.

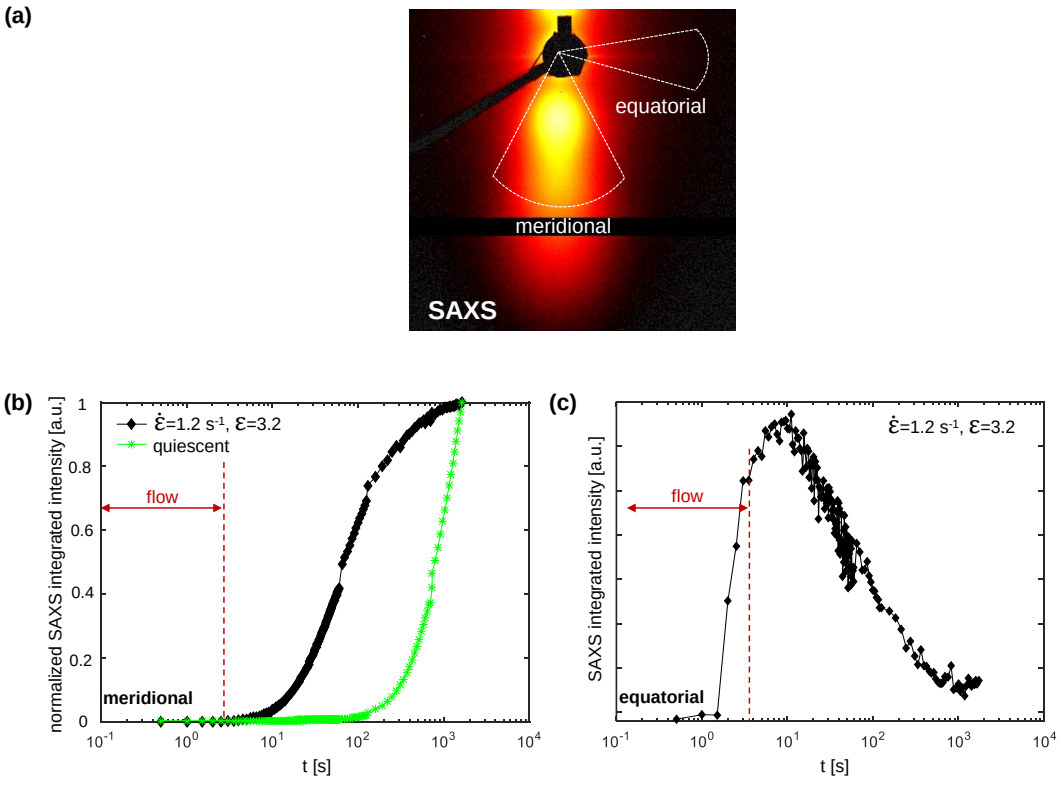

Figure 2.13: (a) Anisotropic two-dimensional SAXS image showing the two azimuthal regions. (b) Kebab intensity evolution (black) compared with meridional intensity evolution under quiescent conditions (green). (c) Shish intensity evolution.

Simultaneously 1D-WAXD patterns have been acquired in the equatorial direction. Because the Pilatus 300K detector has a limited azimuthal range (not sufficient to capture the complex orientation and twisted lamellae typical of polyethylene [72]) only a qualitative time evolution of the characteristic crystal peaks of LDPE is provided. The 3D-plot in Figure 2.14 shows the intensity profiles obtained by radially integrating the 1D-pattern and plotting it against the time and the scattering angle (2θ). The evolution from a completely molten polymer, at the start of the flow, to a fully crystallized one starts with the decrease of the amorphous halo and the appearance of the characteristic peak (110) approximately after 2.5 s. Three reflections centered at scattering angle values (2θ) of 14.7°, 15.1° and 25.4° related to interplanar distances (d) of 4.1 Å , 3.9 Å and 2.4 Å , characteristic for the (110), (200) and (020) planes of the orthorhombic form of polyethylene [73], respectively are present. The small peak at lower scattering angle could suggest the presence of the (001) plane of the monoclinic form of polyethylene usually favored by high deformations [74]. The investigation of the latter is outside the scope of this work.

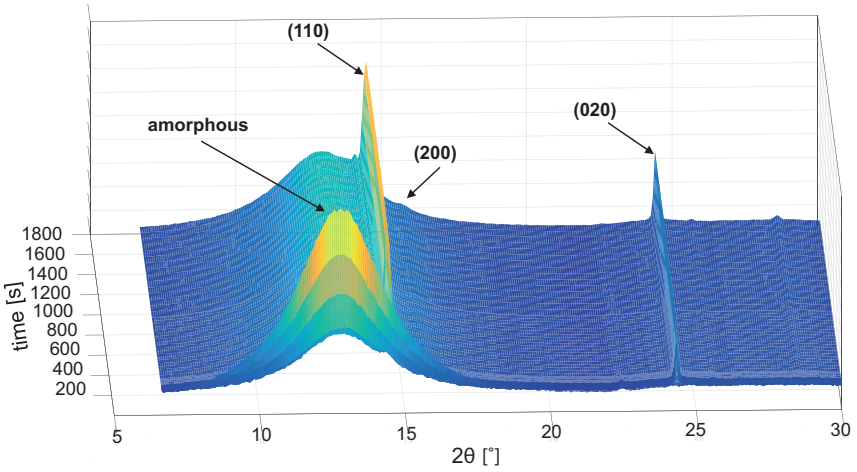

Figure 2.14: Real-time 1D-WAXD evolution for the experiment performed at a final Hencky strain of 3.2 with a constant strain rate of 1.2 s^{-1}.

The results from this case study on LDPE demonstrate the capability of our in-house developed rheometer to simultaneously capture the structure and morphology evolution, and thus the kinetics of the development of the microstructure, while the polymer undergoes a controlled uniaxial extensional deformation. Further experiments at different flow conditions, and on different semi-crystalline polymers, will help in unraveling unsolved questions of flow induced crystallization. Furthermore the fixed location of the midfilament point is a unique innovation that makes the device flexible towards different *in-situ* characterization techniques.

2.5 Conclusions

A filament stretching rheometer has been designed and constructed, with the ability to perform *in-situ* X-ray experiments on flow-induced crystallization of polymer melts during and after a precisely controlled uniaxial extensional flow. To demonstrate the performance of the rheometer the extensional rheology of a molten LDPE sample has been measured, and *in-situ* flow induced crystallization experiments have been performed in a synchrotron radiation facility. Controlled experiments with extension rates up to 2.5 s^{-1}, with a deviation from the ideal diameter ranging from 2% to approximately 15%, depending on the applied strain rate and chosen controller gains, are possible and good agreement with results from commercial rheometers is found. Furthermore the *in-situ* X-ray experiments demonstrate that the crystallization kinetics, and the evolution of crystal structure and morphology can be studied with our innovative rheometer. Access to this unique information will help us to develop an enhanced understanding of extensional flow-induced crystallization that is essential for the design of polymer processing operations involving extensional flow. The flexibility of the rheometer towards different *in-situ* characterization techniques, due to the steady location of the midfilament point, opens new opportunities in material testing.

CHAPTER 3

Unraveling the extensional flow induced crystallization of LDPE via *in-situ* X-ray characterization

Abstract

The extensional flow induced crystallization of LDPE has been investigated. The experimental setup consists of an *in-house* developed filament stretching device that allows for simultaneous time resolved X-ray measurements while applying a uniaxial extensional and well controlled flow on the polymer melt. Isothermal experiments have been performed while varying the applied strain and strain rates in order to investigate the effect of flow conditions on the rheology and crystallization kinetics. There is a clear dependence of crystallization on flow strength that translates into different crystal morphologies: from slightly oriented structures to shish-kebabs. SAXS analysis reveals details on the formation kinetics of kebabs and the presence of a critical time prior to their (observable) growth. Evolution of the kebab diameter reveals a single initial growth rate for every flow condition that is strongly influenced by both strain and strain rate. This kebab growth rate decreases with time.

3.1 Introduction

Low-density polyethylene (LDPE) is one of the most used polyolefins worldwide. It is a semi-crystalline polymer belonging to the family of polyethylene (PE) and is characterized by long chain branches attached to the main polymer backbone, which, together with short chains on the branches, reduce molecular packing leading to crystallinity value, often in the order of 40-50% [75]. As a result LDPE exhibits easy processability, flexibility and good barrier properties [76], which are all required in a

Largely reproduced from:
Pepe, J., Cardinaels, R., Peters, G.W. and Anderson, P.D. Unraveling the extensional flow induced crystallization of LDPE via *in-situ* X-ray characterization. *In preparation.*

variety of applications. In fact, LDPE is used in packaging, trays and plastic bags for food and no food industry, protective foams, flexible lids and bottles and for protective coatings on textile, paper and other types of polymers [76, 77, 78, 79, 80].

Most of the processes used to manufacture the above mentioned products are very complex in terms of thermal [81, 82] and flow conditions, including both shear and extensional components [19, 41, 83], that determine the final polymer structure and hence the final properties. The effect of flow is to enhance crystallization kinetics and, when inducing strong orientation of the polymer chains, to change the type of crystal structure from spherulites, in case of no or weak flows, to shish-kebab structures for strong flows [84]. In addition to the processing conditions, the final crystal morphology is highly dependent on the molecular structure. For instance, the molecular weight and molecular weight distribution, the presence, type and number of branching will affect the material rheology as well as the flow induced crystallization [43, 85, 86, 87, 88, 89, 90]. Most of the studies on the flow induced crystallization of PE polymers focus on linear PE, i.e. high density polyethylene (HDPE), or linear low density polyethylene (LLDPE), a PE with very short chain branches attached to the backbone, or blends of the different PEs, like LLDPE/LDPE blends, that are of importance for blow molding processes.

A broad range of research has been conducted on PE's, focusing on different aspects of flow induced crystallization using both *in-situ* and *ex-situ* X-ray characterization and combinations with other *ex-situ* characterization techniques like Raman spectroscopy and electron microscopy. Linear polyethylene has been characterized studying the flow effect on the long period and lamellar thickness in injection molded samples of linear PE [91, 92], the stability of shish precursors in shear flow as a function of flow strength and temperature in high-density polyethylene (HDPE) [93, 94], the nucleation and growth behavior of twisted kebabs in sheared HDPE [95] and the formation and evolution of shish-kebab structures in solvent extracted sheared PE blends [96]. The LLDPE primary and secondary crystallization kinetics have been investigated in shear flow using dilatometry experiments [97], and the effect of pressure caused by the structure formation of LLDPE was investigated using a piston driven slit flow device [98]. The shish-kebab nature, formation and structure was investigated for blends of HDPE/LLDPE [99] and UHMWPE/HDPE [100].

All the studies mentioned above largely focus on shear induced crystallization. Many of the industrial processes (e.g. blow molding, extrusion and fiber spinning) that involve PE melts, and in particular LDPE, are characterized by strong extensional flows. Very often, the rheological response of polymers to extensional flow is less well characterized than their shear response and, as a consequence, also the effect of extensional flow on crystallization [101]. Structure formation film blowing of LDPE and several blends of LLDPE and LDPE have been investigated both with *ex-situ* X-ray experiments [76] and with innovative setups to follow the in-line developments of the crystal structure during film blowing [29, 72]. These studies provide important information on the processing of polyethylene films during film blowing wherein a biaxial extensional flow occurs, but they do not provide information on the uniaxial extensional flow induced crystallization of the polymers.

Only a few studies are dedicated to the effect of uniaxial extensional flow on crystallization of PE. Derakhshandeh et al. [39] studied the effect of temperature (well above the melting peak of the polymers), strain and strain rate on the rheological response of two different HDPE's using a Sentmanat extensional rheometer (SER). They compared the results with shear experiments showing that the effect of extensional flow induced crystallization is much higher than that of shear at same the temperature and deformation rates. The group of Li investigated the matter using *in-situ* X-ray experiments combined with a modified SER [27]. They found that for HDPE the main cause for shish formation is a polymer network stretch that appears at a critical deformation, when the flow conditions overcome chain relaxation [102]. With the same technique they studied the extensional flow induced crystallization near equilibrium conditions (under slow deformation) and the mechanism that determines the transition to shish nuclei for different cross-linked HDPE's [103].

The different types of PE and blends are unique systems in their own whose response to flow cannot be translated to LDPE. To our knowledge, until this date there is only one study on the extensional flow induced crystallization of LDPE. The group of Hassager has investigated the effect of the extensional stress overshoot on the crystallization of LDPE. They used *ex-situ* X-ray analysis on samples stretched with a filament stretching rheometer (FSR). The crystallization of quenched samples being stretched below, above and at the stress overshoot was studied, for different flow and temperature conditions. It was found that the backbone stretch is reflected in the stress overshoot, typically observed for branched polymers, and that the crystal orientation that determines the final morphology is directly connected to the stress (and thus molecular stretch) decreasing after the overshoot [43].

Despite the insightful knowledge that both extensional rheometer types used in prior works can provide, they suffer from one important limitation: the SER does not allow for a locally controlled deformation while with the FSR in-line structure characterizations are not possible. These limitations cause knowledge gaps in the extensional flow induced crystallization of polymers because of deviations from uniaxial extension or possible changes in crystallinity during the fast (but never instantaneous) cooling of the polymer for *ex-situ* characterizations.

With our in-house developed extensional rheometer, presented in Chapter 2, we combine the advantages of both systems assuring a locally well controlled deformation while allowing *in-situ* measurements. In the present work we use this unique device to systematically study the extensional flow induced crystallization of low-density polyethylene, thereby capturing the extensional rheological response with the rheometer and the crystal structure and morphology evolution with *in-situ* X-ray scattering (SAXS) and diffraction techniques (WAXD). In particular we focus on the effect that flow conditions, at constant temperature, have on the rheological response of the material and on the shish-kebab development. To the best knowledge of the authors, this is the first study of this kind.

3.2 Materials and methods

3.2.1 Materials and material characterization

The LDPE investigated in this work is LD 150BW from ExxonMobil, with a molecular weight (M_w) of 145.6 kg/mol and a polydispersity index (PDI) of 6.4 [76]. Knowing the thermal properties of the material is extremely important to choose the right experimental conditions for the *in-situ* crystallization study. Differential scanning calorimetry (DSC) (Mettler Toledo 823e/700 DSC module) was used with a heating and cooling rate of 5°C/min. The DSC was calibrated for the heat flux and melting enthalpy with indium. To prevent oxidation of the sample, the chamber was flushed with nitrogen gas. The following thermal parameters were extracted from the measurements: melting temperature (T_m), crystallization temperature (T_c), onset of crystallization ($T_{c,onset}$) and crystallinity (x_c), see Table 3.1.

Table 3.1: LDPE thermal properties.

T_m [°C]	T_c [°C]	$T_{c,onset}$ [°C]	x_c [-]
112	100	104	40%

Shear rheological measurements were performed to characterize the linear viscoelastic properties of the material. For this purpose small amplitude oscillatory shear experiments (SAOS) were performed, at a strain amplitude of 2% and frequencies between $2{\cdot}10^{-4}$ and 628 (rad/s) to capture the terminal region and to extract the longest relaxation time. An Ares rheometer equipped with a 25 mm plate-plate geometry was used. The experiments were conducted in a temperature range of 130°C to 190°C in a convection oven under nitrogen flow to avoid degradation of the samples during the measurements. A master curve was created at 150°C using the shift factors (a_T) obtained by time-temperature superposition (TTS). The data were subsequently fitted using the multi-mode Maxwell model for viscoelastic materials from which the relaxation spectrum was derived [62]. For more details on the analysis procedure the reader can refer to Chapter 2 of this thesis. From the relaxation spectrum the reptation time (τ_{rep}) or longest relaxation time at 150°C is found to be 251 s.

The extensional rheology of LDPE was investigated using an *in-house* developed extensional rheometer [101]. This polymer filament stretching rheometer, wherein the polymer is stretched by the simultaneous movement, in opposite directions, of two plates, allows the position of the midfilament diameter to be constant in space. The midfilament diameter is constantly measured by a laser micrometer and used as an input for a feedback loop that controls the separation velocity of the plates in order to obtain a constant deformation rate. The experiments were performed at a temperature of 150°C and at 3 different strain rates: 0.12 s^{-1}, 0.4 s^{-1} and 1.2 s^{-1}. The temperature is kept constant by a PI loop connected to the heating elements of the brass oven while a heated nitrogen flow avoids degradation of the sample. The details of the setup are described in Chapter 2. LDPE is known to show strain hardening due to the presence

of branching. In order to quantify the amount of hardening the data are compared with the LVE base curve calculated using the relaxation spectrum. The results are available in Chapter 2. As expected, a clear dependence of the strain hardening on the strain rate is observed. The onset of this non-linear effect appears at earlier times with increasing strain rate.

3.2.2 X-ray characterization of crystallization

Since LDPE is widely used in polymer processes wherein it undergoes high extensional deformations and changes in temperature, a fundamental understanding of the extensional flow induced crystallization is required to model and predict the crystallization kinetics, crystal structure formation and, in the end, properties. To perform time resolved *in-situ* experiments a high energy X-ray beam source and fast acquisition times are required to properly detect structure evolution. Therefore, the experiments were performed at the European synchrotron radiation facility ESRF, in Grenoble, France. An X-ray beam with a wavelength (λ) of 1.0408 Å and size of 300 μm x 300 μm was used. The *in-house* developed extensional rheometer was used for these measurements. The center of the filament was aligned to the X-ray beam and to the laser micrometer [101]. Small angle X-ray scattering (2D-SAXS) and wide angle X-ray diffraction (1D-WAXD) patterns were simultaneously acquired using a Pilatus 1M and a Pilatus 300K detector, respectively. Patterns were acquired for a total of 30 min (1800 s): for the first 60 s an exposure time of 0.5 s was used, while for the remaining 1740 s the exposure time was 5 s with several waiting times between frames. For analysis purposes the time signal has been corrected for the different acquisition and waiting times.

From the SAXS patterns the evolution of the intensities at the meridional and equatorial region are analyzed, which relate to kebab and shish growth, respectively. In addition an integration of the diagonal region, in between equatorial and meridional, has been performed. The intensity evolution in this diagonal region corresponds to the isotropic and/or not well oriented crystal structures. This diagonal contribution is subtracted from the one in the meridional region to isolate the intensity scattered exclusively from kebabs. Using the Fit2D software [61], the 2D-SAXS pattern is azimuthally integrated to obtain the 1D intensity profile (I_{m}) as a function of the scattering vector $q = 4\pi sin\theta/\lambda$, where 2θ is the scattering angle (see Figure 3.1). The azimuthal angle range used is $80° < \phi < 100°$, $40° < \phi < 50°$ and $-15° < \phi < 20°$ for the meridional, diagonal and equatorial region, respectively. The obtained intensities were subsequently corrected for the background, acquisition time and the decreasing sample thickness during the experiment:

$$I_{corr} = \frac{I_m}{I_{inc}} - \frac{I_p}{I_{p,bkg}} \frac{I_{bkg}}{I_{inc,bkg}}, \tag{3.1}$$

where I_{corr} is the corrected intensity, I_{m} the measured intensity, I_{inc} the intensity measured before the sample, I_{p} the intensity transmitted at the photo-diode and I_{bkg} is the measured intensity of the background at the same acquisition rate. The intensities

were not corrected for dimensionality using the Lorentz factor for 2D (kebabs) and 3D (spherulites) [70] as in our previous work [101] since the correction might not be applicable for all the cases where neither only spherulites or only kebabs are present. The omitted correction was found to not affect the results and their interpretation. As a last step the relative intensity (I) is calculated, by integrating over the whole accessible q range:

$$I = \int_{q_{min}}^{q_{max}} I_{corr}\, dq, \tag{3.2}$$

where $q_{\min}$ and $q_{\max}$ are the minimum and maximum values of the experimental scattering vector.

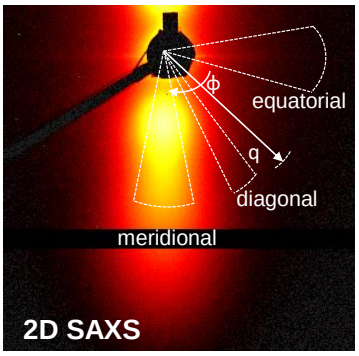

Figure 3.1: SAXS pattern of the last frame acquired for the experiment at strain rate of 1.2 s^{-1} and strain of 3.2.

Prior DSC data have been acquired at the heating and cooling profile (100°C/min and 4°C/min, respectively) characteristic for the rheometer to identify the experimental temperature for the in-situ extensional flow induced crystallization experiments. Based on this measurement a value of 107°C was chosen, 2°C above the onset of crystallization during cooling at 4°C/min. A quiescent *in-situ* X-ray experiment was performed to verify if any crystallization occurs during the preparation phase prior to the flow experiment and to identify the time window frame for extensional experiments prior to crystallization [101]. The radially integrated WAXD patterns were used to calculate the crystallinity x_c, by deconvolution of the total intensity into the amorphous (A_a) and crystalline contribution (A_c), as follows:

$$x_c = \frac{A_c}{A_c + A_a}, \tag{3.3}$$

The integrated intensity, peak position, and peak width were obtained by fitting the curve with a single Gaussian-Lorentzian function, while for the amorphous halo a double Gaussian-Lorentzian function was used, see Figure 3.2.

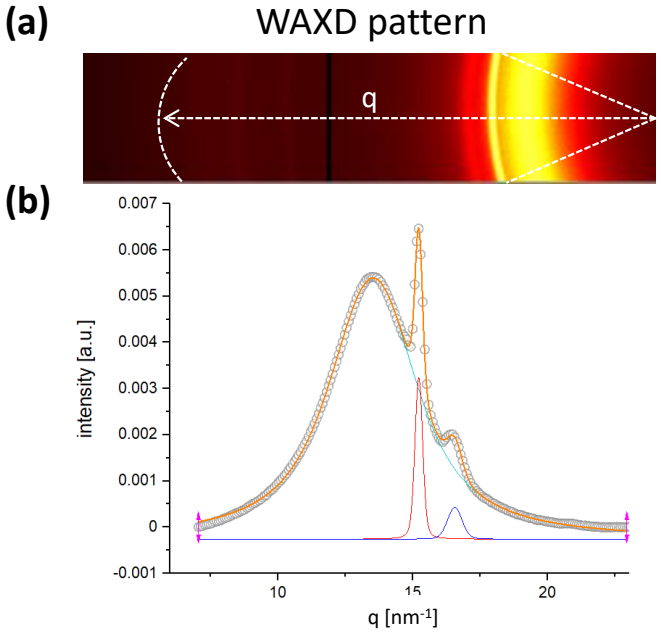

Figure 3.2: (a) WAXD pattern of the last frame acquired for the quiescent experiment at 107°C. (b) Integrated WAXD pattern and fitting of the amorphous and crystalline peaks.

Using the diffraction patterns at different times it is possible to obtain the time-resolved evolution of the crystallinity, see Figure 3.3. In the rest of this chapter only the influence of strain and strain rate on the extensional flow induced crystallization will be investigated.

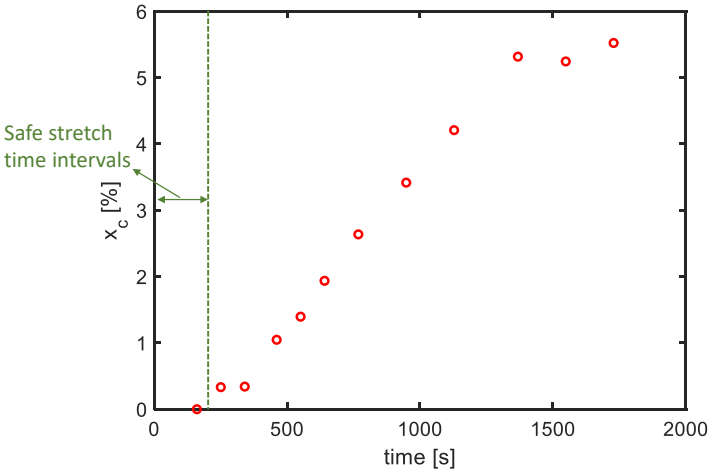

Figure 3.3: Temporal evolution of the crystallinity from the quiescent *in-situ* experiment (107°C). In green the time interval before quiescent crystallization starts is indicated.

3.3 Results and discussion

During *in-situ* X-ray experiments both the evolution of the rheological response of the material to the applied extensional flow as well as X-ray data, reflecting crystallinity and morphology evolution, were acquired. The deformations (Hencky strain ϵ) and deformation rates ($\dot{\epsilon}$) studied are reported in Table 3.2.

Table 3.2: Experimental flow conditions.

$\dot{\epsilon}$ [s^{-1}]	ϵ [-]
0.12	1.3
	1.9
	3.2
0.4	1.9
1.2	1.3
	1.9
	3.2

3.3.1 Influence of FIC on extensional rheology

Flow is known to be able to induce high orientations of the polymer chains and, when strong enough, to determine the local chain stretch. Dimensional analysis helps defining the conditions for which these phenomena will or will not occur. The Weissenberg number in extension generally defined as $Wi = \dot{\epsilon}\tau$, is the product of the applied extensional deformation rate and the characteristic relaxation time of the polymer. There are two characteristic relaxation times: the longest relaxation time, known as reptation time (τ_{rep}), and the Rouse time (τ_s), both derived from shear measurements. For linear polymers $\tau_s = \tau_{rep}/3Z$, where Z is the average number of entanglements calculated as the ratio of the molecular weight of the polymer (M_w) to the molecular weight between entanglements (M_e) [104]. For branched polymers it has been shown that, to capture the non-linear behavior and, from that derive the stretch relaxation times, applying the extended Pom-Pom model [105], a modified version of the original Pom-Pom model of McLeish and Larson [106], works quite well. The work of Verbeeten et al. [105] shows that, for two different LDPE types, the stretch time for the highest molecular weight, (for branched polymers the part of a molecule that has the highest number of branches) is of the same order or even equal to the reptation time. This result is adopted in the current work. When τ_{rep} is considered then Wi_{rep} defines the degree of orientation of the chains while, when τ_s is used Wi_s defines the possibility of chain stretch. Using the dimensionless Wi number the strength of the flow is defined for the applied conditions and the results are reported in Table 3.3. In particular, for $Wi_{rep} < 1$ and $Wi_s < 1$ the polymer chains are at equilibrium, when $Wi_{rep} > 1$ and $Wi_s < 1$, orientation is predominant, while at $Wi_{rep} > 1$ and $Wi_s > 1$ partial or full stretch occurs [107]. From Table 3.3 it is clear that at all flow conditions strong orientation is present as well as chain stretch which becomes more predominant with increasing strain rate.

Table 3.3: Weissenberg number at 107°C.

$\dot{\epsilon}$ [s^{-1}]	Wi_{rep} [-]	Wi_{s} [-]
0.12	249.4	$\sim O(Wi_{\mathrm{rep}})$
0.4	831.4	$\sim O(Wi_{\mathrm{rep}})$
1.2	2494.2	$\sim O(Wi_{\mathrm{rep}})$

When comparing the extensional rheology at 107°C (FIC experiment) and 150°C (melt state), it is possible to observe the clear influence of the temperature on the accumulated stress: a lower temperature results in a higher axial force for the same diameter, see Figure 3.4 (a) and (b), respectively. Notice that the experiment performed at 150°C is continued until breakage of the filament and was not interrupted at a specific strain, therefore the total strain for both experiments is different. In addition to the above mentioned, from the force signal it is possible to identify the onset of strain hardening from an increase of the force after a decay from the initial maximum. The formation of this minimum shifts with the onset of strain hardening as can be seen in Figure 3.4 (a) for the two different temperatures. The effect of temperature is valid at all flow conditions but the particular example given below is representative for a deformation rate of 1.2 s^{-1}.

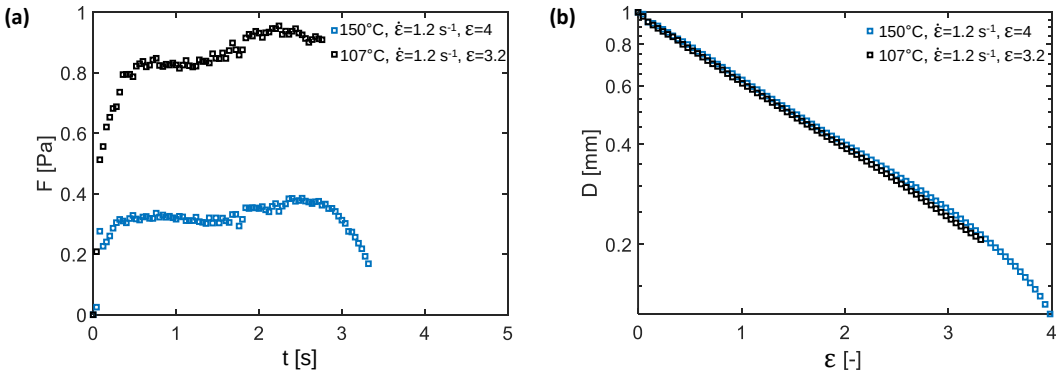

Figure 3.4: (a) Influence of temperature on the force signal during stretching. (b) Diameter evolution for different temperatures at the same strain rate.

When analyzing the extensional viscosity as function of total deformation it is possible to observe the strong influence that the temperature has on the extensional viscosity (see Figure 3.5). A lower temperature enhances the strain hardening phenomenon and the effect is similar for different strain rates, i.e. 0.12 and 1.2 s^{-1}, at the same temperature (107°C) and strain. Considering that at $\dot{\epsilon} = 1.2$ s^{-1} the polymer crystallizes immediately after the start of strain hardening, as shown in our previous work [101], while at $\dot{\epsilon} = 0.12$ s^{-1} no crystallization occurs during flow, it is not clear from these results whether any crystallization during flow has an effect on the strain hardening behavior. It seems that the crystallization process during flow involves such a small portion, due to local stretch of the polymer chains that the effect is not strong enough to influence the rheology.

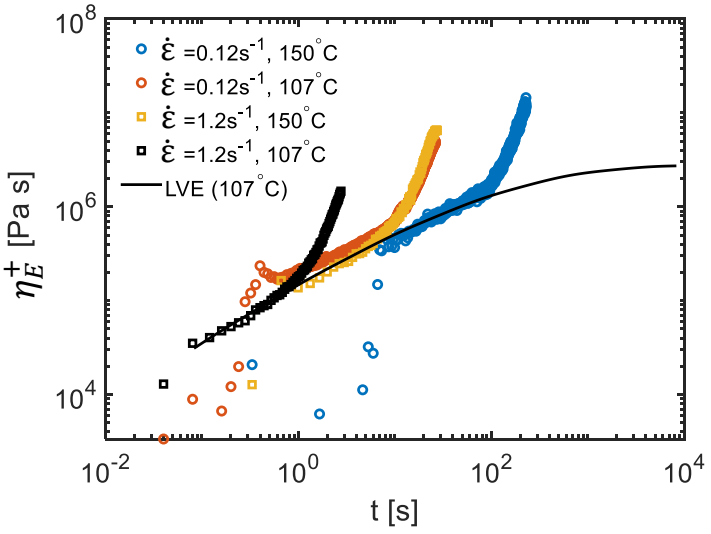

Figure 3.5: Influence of temperature on the transient extensional viscosity. The data at the reference temperature of 150°C are shifted to the experimental temperature of 107°C using the shift factor a_T.

As mentioned before, the goal of this work is to gain knowledge on the extensional flow induced crystallization mechanism as a function of strain and strain rate. The rheological responses of the material to the applied flow field in Table 3.2 are shown in Figure 3.6 (a), (b) and (c), where the influence of strain in (a) and (b) and of strain rate (c) can be observed. The experiments at constant strain rate give the opportunity to split the extensional curve at different points in time to extrapolate the effect of the deformation on the crystal morphology while, when fixing the deformation, it can be observed that the strain rate strongly influences the strain hardening. Extensional rheology results of flow induced crystallization experiments are not sensitive enough to provide information about the crystallization process as already mentioned earlier. Therefore, the simultaneous acquisition of X-ray data is of vital importance to study the flow induced crystallization phenomenon.

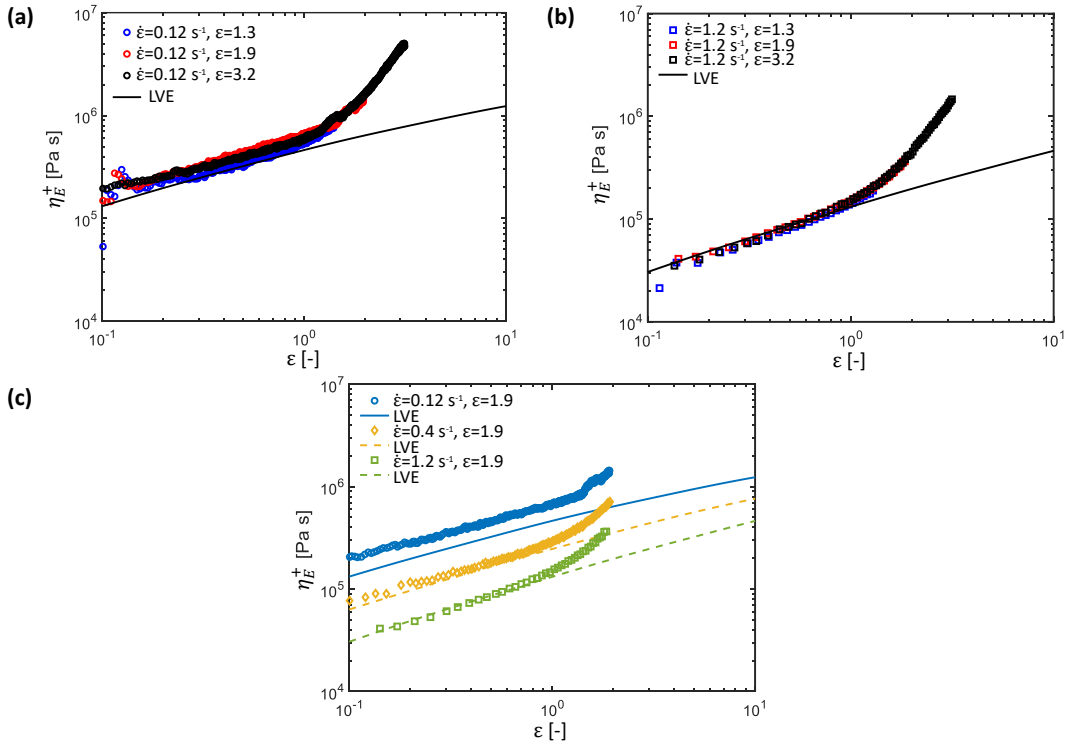

Figure 3.6: (a), (b) Transient extensional viscosity for experiments up to different strain. (c) Transient extensional viscosity at different strain rates (107°C).

3.3.2 *In-situ* X-ray study of FIC

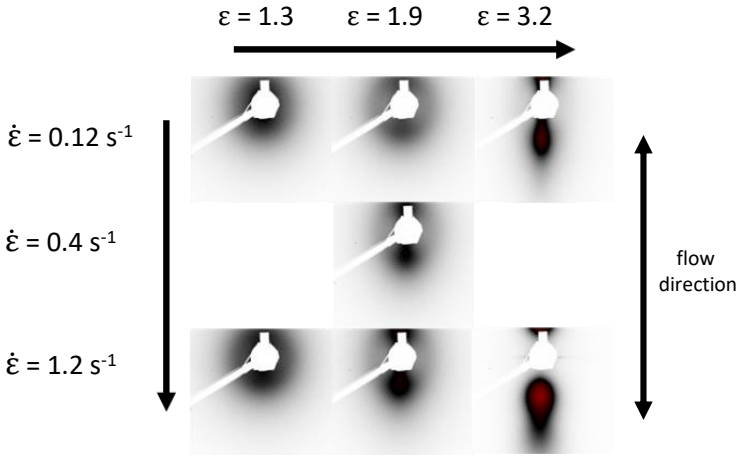

Figure 3.7: Final SAXS patterns (107°C)

Figure 3.7 shows the 2D-SAXS pattern of the last frame acquired for the different flow conditions applied. From these images it can be observed that increasing both the strain

and strain rate enhances orientation. Despite the fact that the dimensional analysis suggests chain stretch at all strain rates it is clear that the effect of deformation history is key for the formation of shish-kebab structures (resulting in streaks in the opposite direction to the flow and blobs in the flow direction, respectively). Moreover, at the flow conditions examined the effect of strain is predominant compared to the effect of strain rate. This can be understood better when analyzing the integrated intensities. Figure 3.8 shows an example of the procedure used to calculate the kebab intensity evolution: first the meridional and diagonal intensity are calculated (Figure 3.8 (a)), subsequently the diagonal intensity, corresponding to the isotropic and less well oriented structures, is subtracted from the meridional one to obtain the contribution of kebabs solely (Figure 3.8 (b)). Notice that, when subtracting the two intensities, the initial step present in the kebab curve becomes more dominant confirming that the contribution of the isotropic crystals masks some of the features of the kebab formation.

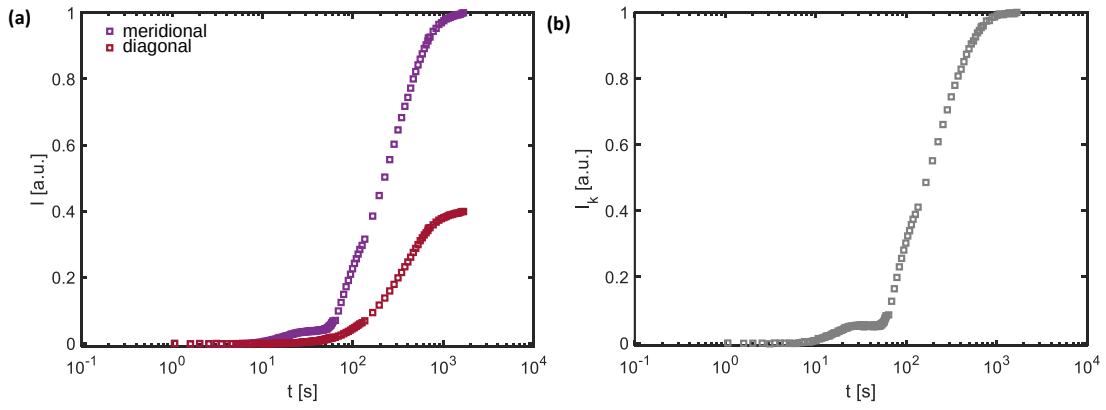

Figure 3.8: (a) Relative meridional and diagonal intensities normalized with maximum value of meridional intensity and (b) kebabs normalized intensity for $\dot{\epsilon}$= 1.2 s^{-1} and ϵ = 1.9.

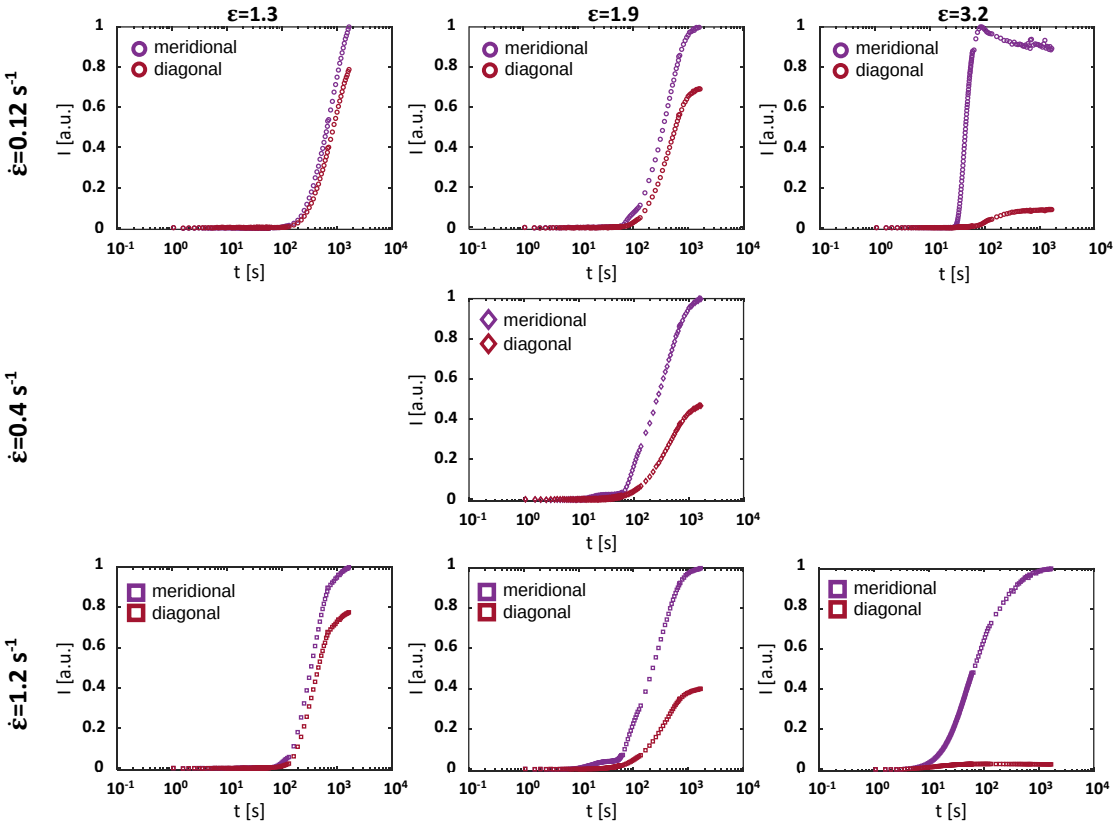

Figure 3.9: Meridional and diagonal intensity normalized with the maximum value of meridional intensity for different flow conditions.

In order to understand the influence of the flow conditions on the crystallization process, first the diagonal and the meridional intensity evolutions are taken into consideration (see Figure 3.9). It can be observed that with increasing strain and strain rate the time to start crystallization is reduced for both oriented (meridional) and isotropic and less oriented structures (diagonal). The strain has a remarkable influence on increasing the amount of orientation as can be observed by the decrease of the diagonal intensity compared to the meridional one. This effect is less pronounced when an increase in strain rate is considered.

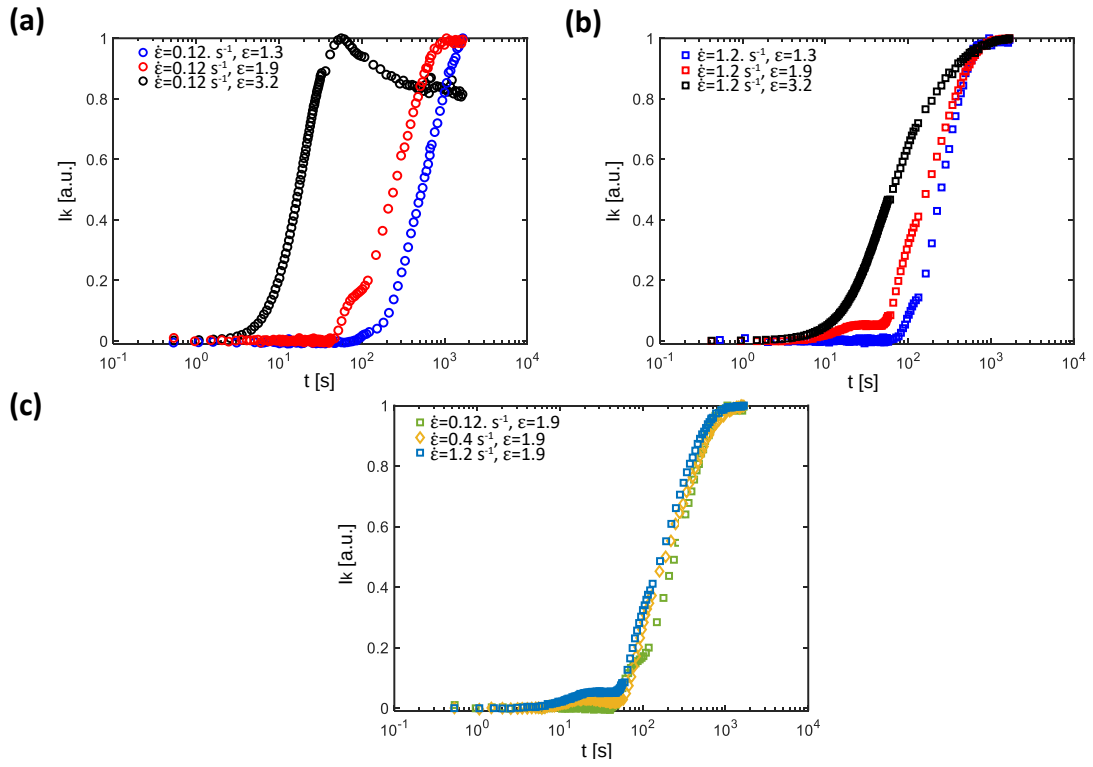

Figure 3.10: Kebabs normalized intensity for different flow conditions.

In order to evaluate the kinetics of solely oriented structures (kebabs) the diagonal intensity has been subtracted from the one in the meridional region and the obtained kebabs intensity evolutions are plotted in Figure 3.10. It is important to mention that in Figure 3.10 the starting time has been considered to be the time after cessation of extensional flow. This in order to get a better comparison of the results at different flow conditions. It is possible to observe that when the strain is kept constant (Figure 3.10 (c)) the crystallization rates and kinetics are less influenced, while with increasing strain, for a strain rate of 0.12 s^{-1} and 1.2 s^{-1}, a clear influence on the crystallization rate and kinetics can be observed (see Figure 3.10 (a) and (b)). Interesting to notice is that at a strain rate of 0.12 s^{-1} and strain of 3.2 a sharp increase of the meridional intensity is observed (Figure 3.10 (a)), with a subsequent decrease after about 80 s for which the authors do not have a clear explanation. Despite the fact that kebabs are formed at different flow conditions, shish are only detectable and quantitatively measurable at a strain rate of 1.2 s^{-1} and strain of 3.2. This can occur when no shish are formed or when the length and/or concentration of shish is too small to be detectable by the SAXS technique [99, 100]. The evolution of the shish for this single flow condition is reported in Chapter 2 where it was shown that the shish intensity decreases when the intensity of the kebabs becomes predominant, thereby causing an apparent decrease of the equatorially measured intensity and implying that the shish formed are not metastable but crystalline in structure. We have confirmed this hypothesis by comparing the 2D SAXS pattern with the 1D-WAXD pattern (see Figure 3.11): while a weak shish signal starts to appear around 1.5 s on the SAXS pattern, the WAXD pattern does not

show any signal of crystallization yet. Only about 1 s later, and therefore at 2.5 s a clear peak corresponding to the 110 crystal phase is detected confirming the transformation of the shish from local oriented and stretched segments of molecules to a crystal structure.

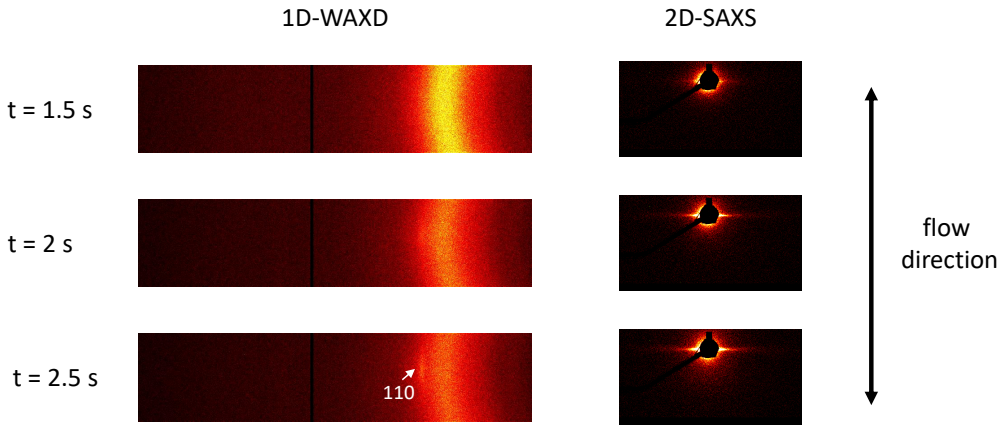

Figure 3.11: 1D-WAXD and 2D-SAXS pattern evalution of the 110 crystal phase and shish, respectively at strain rate of 1.2 s^{-1} and strain of 3.2.

The effect of flow is very evident when analyzing the kebab intensity. When increasing the flow strength one can observe the formation of a step in the temporal evolution of the intensity that disappears at $\epsilon = 3.2$. We hypothesize that when the flow is not strong enough to create well defined shish-kebab structures an "ordening" along the polymer backbone (between branches) forms. These not well oriented structures have long correlation distances and, therefore, the scattering contribution is very small and located very close to the beam stop. This phenomenon induces a first increase in the kebab intensity. Further increase of ordering does not translate in an increase in the scattered intensity since the difference in electron density between these oriented structures and the amorphous phase is not high enough. A certain time is required before the kebabs can significantly contribute to the scattered intensity. At this point a new increase of intensity is observed. The fact that this step is not clearly visible at $\epsilon = 1.3$ and at $\epsilon = 3.2$ can be explained considering that at low strain the amount and size of kebabs formed might be very small to significantly contribute, while at high strain the transition period is extremely short or not existent. To understand the nature of the step formation in the kebab intensity we have analyzed the 2D-SAXS and have estimated the critical time for the formation of kebabs.

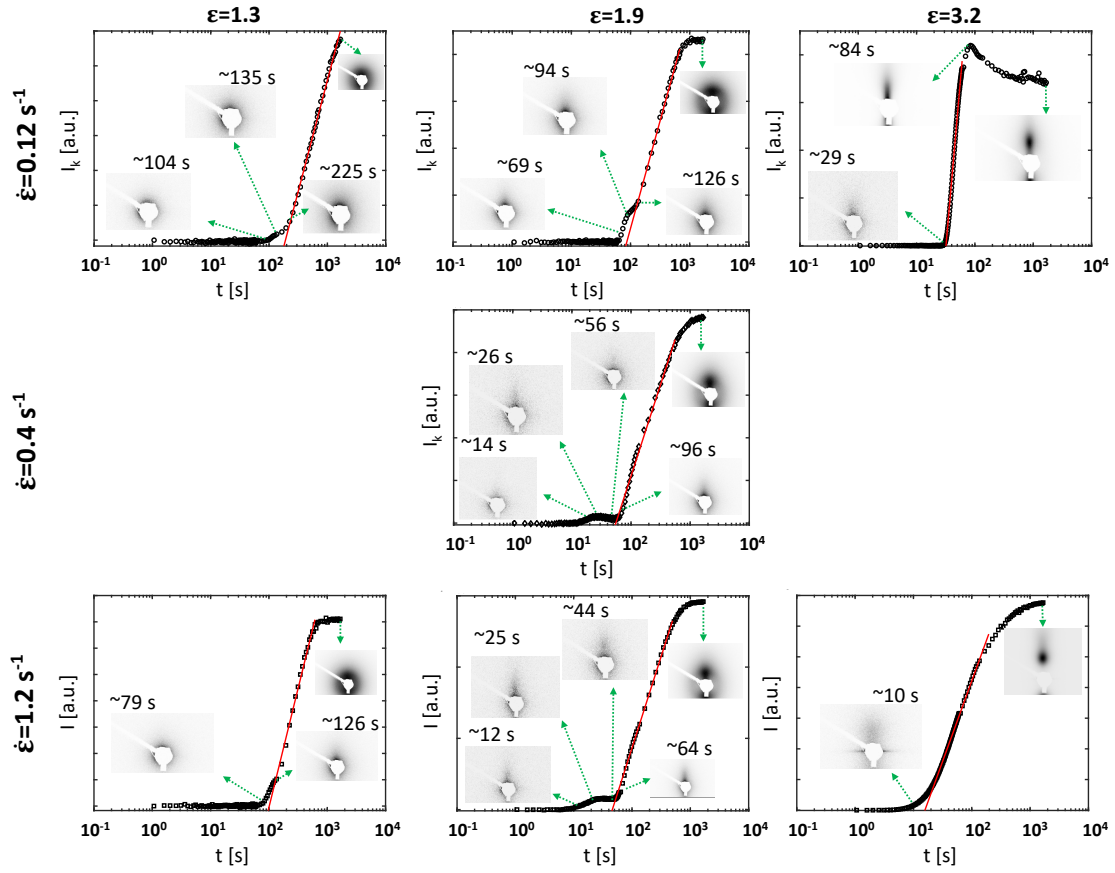

Figure 3.12: Kebab intensity for different flow conditions (symbols) and fitting (lines). Images correspond to the 2D-SAXS pattern at a specific time.

In Figure 3.12 the streak like shape of the meridional patterns in the 2D-SAXS images, at the timescale of formation of the step, is typical of ordered entities along the backbone with smaller length scale compared to kebabs and very high correlation distances. The critical time for the growth of kebabs has been calculated from the intercept of the fitted (red) line to the x-axis, as shown in Figure 3.12. From Figure 3.13 (a) the critical time decreases with increasing strain for both $\dot{\epsilon}$= 0.12 s^{-1} and $\dot{\epsilon}$= 1.2 s^{-1} and the curve shifts downward at higher strain rates. The dependence of strain rate is highlighted in Figure 3.13 (b). The formation of an 'ordening' phase before the growth of kebabs is confirmed in Figure 3.14. The evolution of the measured intensity (I_m) shows no maximum (see Figure 3.14 (b)) at the time scale correspondent to the step in the kebab intensity in Figure 3.14 (a), confirming that the correlation distance at the beginning, if present, is higher than the estimated value of 85 nm (calculated from the initial value of q from where no maximum is present), which is well above of typical correlation distances for kebab structures (see further on). A schematic representation of this two step process for the growth of kebabs is proposed in Figure 3.15 where, for example purposes, the evolution of the kebab intensity for the experiments at $\dot{\epsilon} = 1.2$ and at $\epsilon = 1.9$ has been taken into consideration.

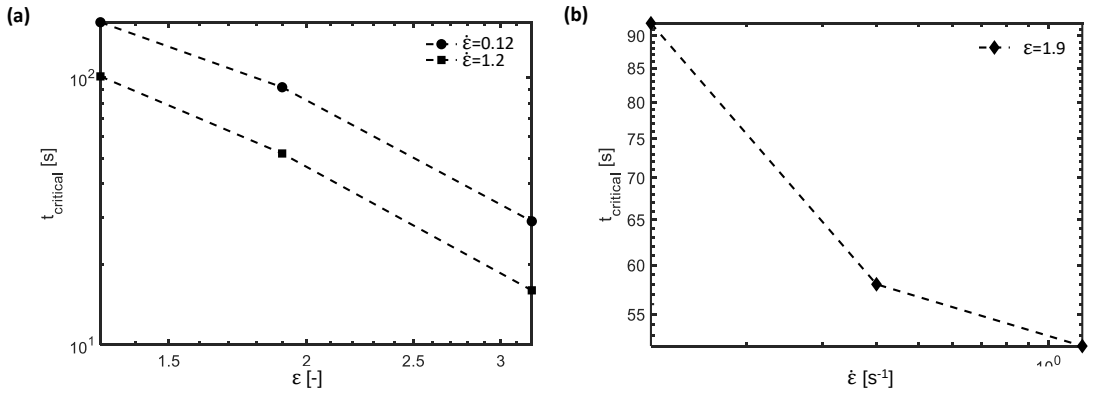

Figure 3.13: Critical time for the kebab growth as function of strain (a) and strain rate (b). Lines are drawn to guide the eye.

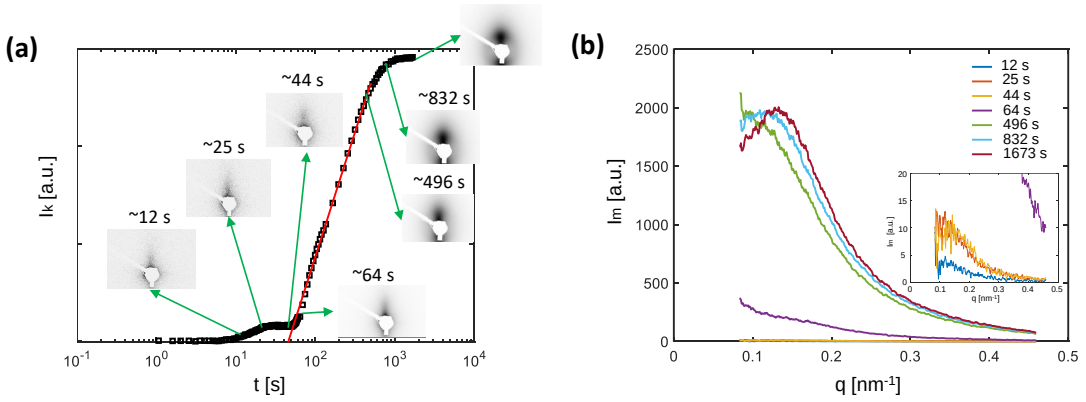

Figure 3.14: (a) Kebab intensity evolution and 2D-SAXS pattern at selected times and (b) measured intensity as function of the scattering vector at selected times. Inset shows the evolution of the intensities for t<64 s. Data correspond to the experiments at $\dot{\epsilon}$= 1.2 s^{-1} and ϵ = 1.9.

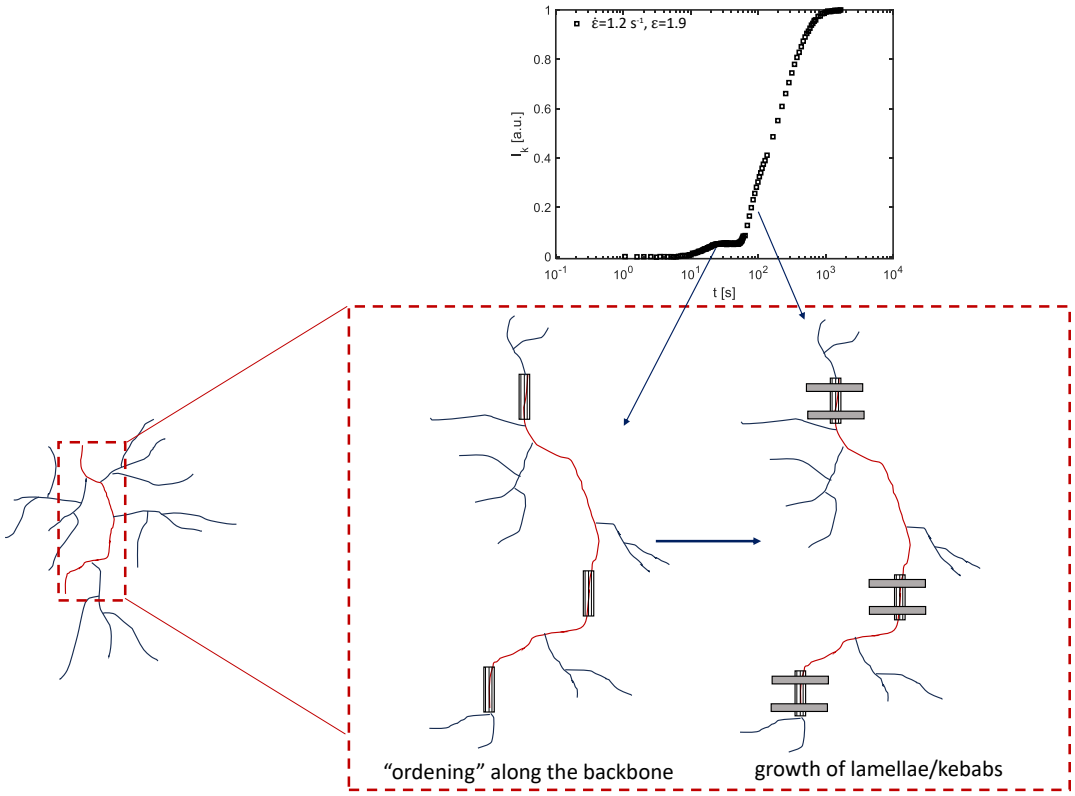

Figure 3.15: Schematic representation of the kebab formation process. On the left typical branch on branch structure of LDPE.

Previous studies on isotactic polypropylene (iPP) have shown that the kebab growth rate is enhanced by molecular orientation close to the shish backbone and, while growing faster initially, the growth rate decreases over time [108]. The model developed by Roozemond at al. for iPP was validated by *in-situ* WAXD measurements using a uniaxial extensional flow device [35] and a piston driven slit flow device [109]. Therefore, to gain a deeper knowledge of the formation of kebabs, and to find out whether kebabs have a non-constant growth rate for LDPE too, we applied the model developed by the group of Hsiao [11, 99]. This model provides the radial growth of kebabs. The model assumes each shish kebab structure to be independent from the neighboring ones and therefore considers a single shish kebab. Kebabs are known to be folded lamellae growing around the shish as a disk, and the model assumes them to be perfect discs with a specific diameter (D), thickness (T) and long period (L_p) (see Figure 3.16 (a)). The kebabs have a periodic arrangement along the shish with an infinite length [11, 99]. The scattered intensity in the meridional region can, then be expressed as [11, 99]:

$$I(s_{1,2}, s_3) = K\left[\langle|A(s_{1,2}, s_3)|^2\rangle_{D,T} - |\langle A(s_{1,2}, s_3)\rangle_{D,T}|^2 + \langle|A(s_{1,2}, s_3)|^2\rangle_{D,T}|Z_L(s_3)|^2\right], \quad (3.4)$$

where K is a proportionality factor that mainly takes into account the electron density difference between the crystalline and amorphous phases, and the crystalline volume fraction and finite density transition at the interface, $s_{1,2}$ and s_3 are the components of the scattering vector in the equatorial and meridional direction respectively, $A(s_{1,2},s_3)$ is the Fourier transform of the electron density distribution of a single disc and Z_L is a 1D paracrystalline lattice factor. When the generalized Γ-distribution is employed to describe the distribution functions of the long period Lp, diameter D, and thickness T of the kebabs, Eqn. 3.4 provides an analytical expression that can be used to fit a set of meridional intensity slices (I versus s_3 at constant s_{12}) and, in this way, allows to obtain the dimensions that characterize kebabs. For more details on the model the reader is referred to Somani et al. [11]. An example of the extracted intensity profile and of the agreement between experimental data and fitting can be found in Figure 3.16 (b) and Figure 3.16 (c), respectively.

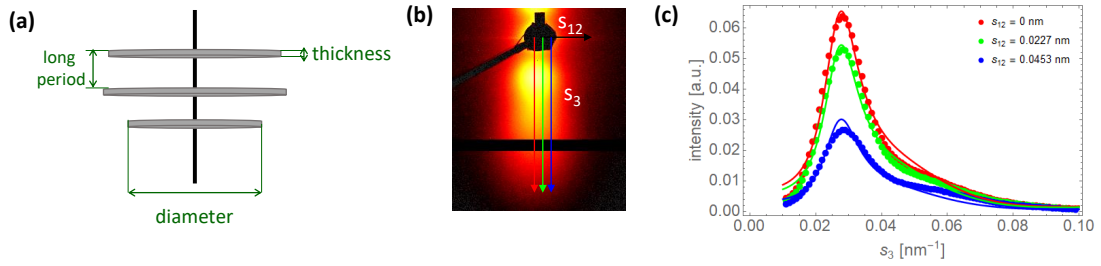

Figure 3.16: (a) Representation of the shish-kebab model. (b) SAXS pattern with schematic of the 1d-integration for the intensity extraction. (c) Experimental data (dots) and fitted intensity (lines). The data shown refer to the last frame of the experiment at $\dot{\epsilon}$= 1.2 s^{-1} and ϵ = 3.2.

The average dimensions of the kebabs, obtained from the fitting, are plotted as a function of time. Figure 3.17 presents an example of the calculated dimensions for the case $\dot{\epsilon}$= 1.2 s^{-1} and ϵ = 3.2. It confirms that the model describes the experimental data quite well and is capable of capturing important key aspects of the kebab growth. The diameter shows an initial constant growth rate with a subsequent decrease before reaching the plateau. The final plateau can be explained considering the fact that in time the kebab grows big enough to cause impingement: the kebabs from neighboring shish start to interfere. Regarding the decrease of the long period observed there are controversial hypotheses: according to Balzano et al. [26] the long period is constant under isothermal conditions for isotactic polypropylene despite impingement of the kebabs, while Keum at al. [99] justified the decrease of the long period for HDPE/LLDPE blends with the hypothesis that at short times kebabs initiated from certain shish are densely packed and thus have a short long period while kebabs developed later are more loosely packed giving the possibility for additional kebabs to grow. The overall effect is a decrease of the average long period with time after a first increase. The kebab thickness is known to be only dependent on the temperature under isothermal conditions if no other external stimulus is applied [26, 98]. The model shows, surprisingly, a (small) change in the thickness

during the isothermal experiments that approaches a constant value of around 11 nm after 35 s.

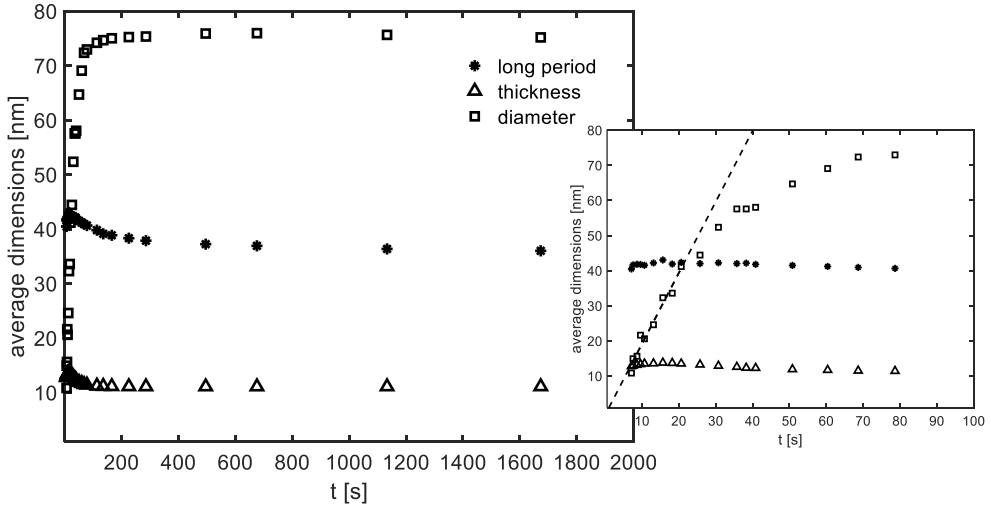

Figure 3.17: Evolution of kebab diameter, thickness and long period at strain rate 1.2 s^{-1} and strain 3.2 (107°C). The dotted line is drawn to indicate the initial kebab growth rate.

The model cannot be used when the molecular orientation is not enough to induce the formation of well defined shish-kebab structures and when the kebab size and/or density is too small. In the latter case the predictions are not accurate anymore. Therefore the model was used only for the following flow conditions:

Table 3.4: Experimental flow conditions.

$\dot{\epsilon}$ [s^{-1}]	ϵ [-]
0.12	3.2
0.4	1.9
1.2	1.9
	3.2

Figure 3.18 shows the shish-kebab model results for the flow conditions in Table 3.4. The long period is overall higher for the lower strain (1.9) suggesting the presence of more amorphous area between kebabs and therefore a lower nucleation density. The kebab thickness is constant and around a value of 15 nm except for strain rate 1.2 s^{-1} and strain 3.2. For the latter, as already observed before, the thickness is not constant over time and the final steady state value is lower and approximately 11 nm.

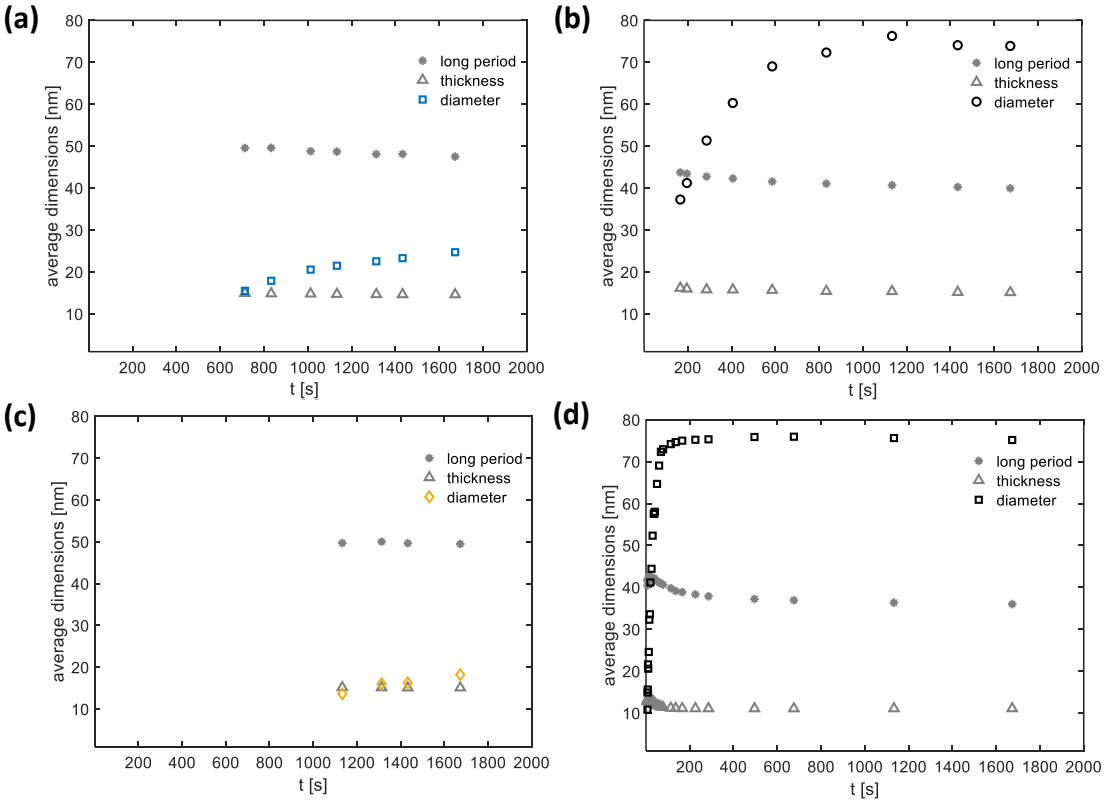

Figure 3.18: Evolution of the kebab diameter, thickness and long period for different flow conditions: (a) $\dot{\epsilon}$= 0.4 s^{-1} and ϵ = 1.9, (b) $\dot{\epsilon}$= 0.12 s^{-1} and ϵ = 3.2, (c) $\dot{\epsilon}$= 1.2 s^{-1} and ϵ = 1.9 and (d) $\dot{\epsilon}$= 1.2 s^{-1} and ϵ = 3.2.

In order to analyze the kebab growth rate in more detail we compared the temporal evolution of the kebab diameters in Figure 3.19. For all the flow conditions the kebabs do not show a single growth rate: after an initial constant value the growth rate slows down without reaching a new constant value. Despite the fact that the behavior is similar to what was observed for iPP [108], where this decrease is caused by a relaxation of the molecular orientation in the surrounding of the shish, for LDPE it is not clear what could cause the decreasing growth rate of the kebabs. Overall the kebab growth rate is strongly influenced by the flow parameters (see Table 3.5) while the strain plays a dominant role in determining the final kebab diameter.

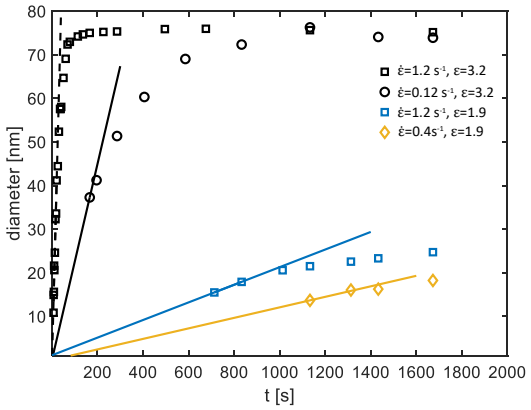

Figure 3.19: Influence of flow conditions on the kebab diameter evolution for different flow conditions (107°C). The lines are drawn to indicate the initial kebab growth rates.

Table 3.5: Initial kebab growth rate for different flow conditions (107°C).

$\dot{\epsilon}$ [s^{-1}]	ϵ [-]	G [nm/s]
0.4	1.9	0.012
1.2	1.9	0.020
0.12	3.2	0.225
1.2	3.2	2.022

WAXD pattern are used to extract information on the crystallinity, crystal phases and their structure and orientation. Because of the limited angle available in the 1D-WAXD patterns and the imperfect alignment at the equator region it is not possible to perform a quantitative analysis, because of the orientation induced by the flow the peaks are not fully captured on the detector. Polyethylene is known to form two types of oriented structures namely Type I with twisted lamellae and Type II with lamellae perfectly aligned to the flow direction which usually form at very high strain [72]. From the WAXD patterns shown in Figure 3.20 it is clear that for the experiments at a strain of 3.2 the lamellae formed are a mix between Type I and Type II since the 100 peak splits while the 200 peak is present at the equator. Wingstrand et al. [44] have already demonstrated the formation of these mix structures for intense flow conditions in the case of LDPE via *ex-situ* extensional flow induced crystallization experiments. For strains of 1.9 and 1.3, for all deformation rates, from the region available it seems that a Type II structure is present. This is in contradiction with the fact that Type II structures only form under very strong flow conditions and in the particular case analyzed, shish kebab structures are not always visible. While for low strain (1.3) an almost fully isotropic structure is formed for intermediate strain (1.9) a sort of Type II structure is formed. Because all the peaks, including the 200 one are present at the equator, this could be the result of the isotropic contribution being present simultaneously. Unfortunately because of the limited view of the WAXD detector no further conclusions can be made. The authors decided to not perform *ex-situ* WAXD experiments because of the extremely

rapid crystallization rate of LDPE upon cessation of the isothermal conditions which could cause variations in the actual crystal structure.

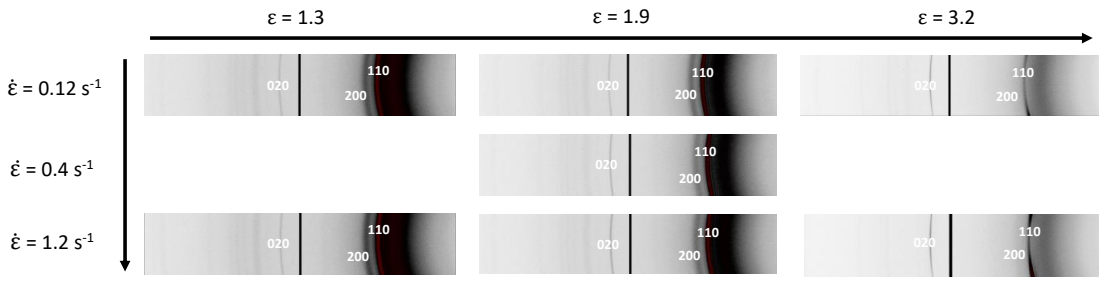

Figure 3.20: Final WAXD patterns (107°C).

Considering the results above a schematic representation of the final crystalline morphology is proposed in Figure 3.21. Because the effect of strain is predominant we decided to generalize the schematic considering the three strain levels investigated in the present work. At higher strain ($\epsilon = 3.2$) more and longer shish form between the branched points. Most of the kebab fully orient in the flow direction but we assume that the distance between shish is high enough to allow twisting of kebabs giving rise to the mixed Type I- Type II structures. It is not excluded, especially for lower strain rates, that other oriented and non oriented structures with twisted and non twisted lamellae can form. For $\epsilon = 1.9$ clear kebabs are visible from the SAXS pattern. In this case the number, diameter and length of shish formed is lower. The bigger distance between shish gives the opportunity for kebabs to easily twist, and on the other hand, for other oriented and non oriented structures (like spherulites and randomly oriented structures) with twisted (always in case of PE spherulites [110]) and non twisted lamellae to form. These structures in between might hinder the further growth of kebabs causing an overall lower diameter than at higher strain. For $\epsilon = 1.3$ the amount of orientation is relatively small therefore we assume the presence of spherulites and other crystal structures with lamellar orientation in the direction of the flow. In Figure 3.21 the scale between shish-kebab structures and spherulites is not realistic since the order of magnitude of their size is 100 nm and 10 μm, respectively.

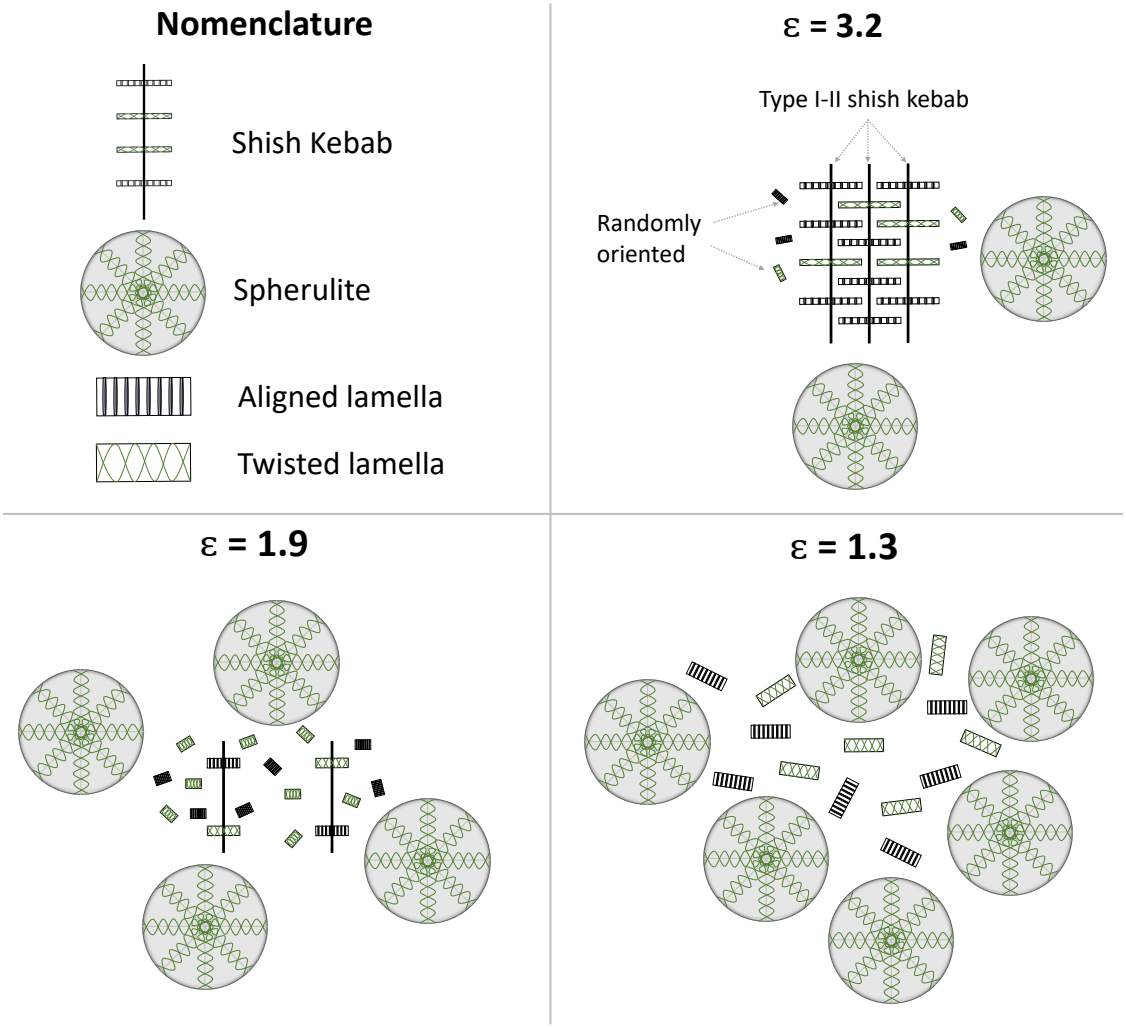

Figure 3.21: Schematic representation of the proposed crystalline morphology for different deformations.

Despite a lack of a more complete set of experimental data the results shown in this work prove the capability of this experimental methodology and analysis to study in details the extensional flow induced crystallization mechanism.

3.4 Conclusions

In the present work we have, for the first time, performed a systematic study on uniaxial extensional deformation induced crystallization of LDPE combining in-situ X-ray experiments with rheological measurements. The rheological data reveals that even when the polymer crystallizes during flow the strain hardening behavior remains unchanged, this can be explained considering that for branched polymers a large amount of the molecular parts can stretch (branch points act like crosslinks) and the contribution of relatively small flow induced crystal regions (also acting like crosslinks)

it is not strong enough to effect the rheology. From the SAXS data a clear dependence on the flow conditions is found in the crystallization evolution, with a stronger effect of deformation over deformation rate. The onset of crystallization shifts to earlier times at higher deformations and deformation rates, and crystallization during flow occurs in the strain hardening regime. From the set of data available it was not possible to determine whether crystallization during flow occurs at a critical strain [102], when the deformation rate is high enough to cause molecular stretch. The analysis reveals the presence of an initiating phase during which kebabs precursors are formed. The presence and duration of this phase strongly depend on the flow conditions. It is possible to follow the kebab growth rate applying an existing model. The diameter growth rate clearly shows a dependency on the deformation history and decreases with time, i.e., the influence of the deformation (the molecular orientation) relaxes with time. This is similar to what is observed for other polymers [108]. Because of the limited angle available in the 1D-WAXD pattern it is not possible to follow the crystallization rate and fully define the type of oriented lamellae formed, but its simultaneous use with SAXS revealed the crystalline nature of the shish formed during flow at a strain rate of 1.2 s^{-1} and strain of 3.2. This work provides new insights in the extensional flow induced crystallization of LDPE never studied before with time resolved measurements. Despite its novelty it does not provide a full understanding of flow enhanced crystallization phenomena but it signs the start of a new set of experimental research that can fill the knowledge gp in the field for LDPE and other materials.

CHAPTER 4

A study on the jetting process of highly viscous fluids: from droplet-on-demand (DOD) to volume-on-demand (VOD)

Abstract

A study of the jetting performance of highly viscous fluids with a high viscosity has been performed. Thereto, an experimental setup has been developed consisting of a piston piezo-driven microdispensing valve, as a jetting device, combined with an optical system to visualize the jetting process. The setup allows dispensing of extremely high viscous fluids, while thanks to a high speed camera and microscope system, the fast dispensing process can be captured. When using high viscosities such as the ones used in this work the jetting process results in a transfer of fluid from the nozzle to the substrate via formation of a liquid bridge. The process image sequences have been analyzed to extract filament thinning and fluid spreading on the substrate. The effects of the substrate to nozzle distance and fluid viscosity have been systematically investigated. The substrate heights as well as viscosity have a direct impact on the process time scale and volume deposited. The interplay between axial forces in the filament and capillary forces in the spreading droplet governs the process. This interplay turns out to be highly dependent on the substrate height.

4.1 Introduction

Jetting has been used for decades as the main paper printing technology. It is based on the idea of producing tiny droplets of fluid (ink) through a printhead, depositing them on a substrate (paper) according to a predefined pattern (text/image). Because of the intrinsic capability of the technique to achieve high resolution, accuracy, throughput and

Largely reproduced from:
Pepe, J., Cardinaels, R., Peters, G.W. and Anderson, P.D. A study on the jetting and spreading process of highly viscous fluids. *In preparation.*

versatility it has potential in industrial applications wherein an accurate deposition is required [111, 112, 113]. It has already being used, for example, in food [114, 115, 116], electronics [117, 118, 119, 120], biomedical [121], pharmaceutical [122, 123, 124], packaging [125] and textile industry [117]. It is an emerging technology and promising additive manufacturing technique regardless of the fact that 3D printing still remains one of its biggest challenges.

The process relies on an intimate relation between ink properties, printhead technology and droplet formation as key in defining the quality of the end product. The technology core is the droplet generation, which in conventional jetting processes can occur in two ways: continuously or on demand. In continuous inkjet printing (CIJ) a harmonic modulation is applied to a continuous stream of fluid in order to create droplets. Electrostatic charging and deflection are used to select and deposit the droplets on a specific location on a substrate [112]. On the other hand, droplet-on-demand (DOD) printing produces individual droplets discretized in time and space. Small droplets are created in response to a pulse, generated either thermally or piezoelectrically [126].

The fluid physical and rheological properties are essential to determine jettability and the breakup process [127, 128, 129, 130]. Firstly the fluid should have a low viscosity (< 20 mPa·s) to avoid that the energy generated by the printhead is dissipated within the fluid with consequently no ejection [111]. Secondly the fluid thinning and breakup process should be optimal in order to obtain stable droplets in a rapid manner [111]. For demanding applications high molecular weights (M_w) and/or high loads of functional particles are required to achieve the desired properties. As a consequence the viscosity of the fluid increases dramatically with in addition inevitable changes of the viscoelastic properties. In the past years several studies have been devoted to the fabrication of new printheads that could eject higher viscosity fluids ($\leqslant 500$ mPa·s) [131, 132, 133], as well as combining the conventional printhead technologies with reactive processes [134, 135, 136] and UV-curable inks [117, 137, 138]. Recent studies have shown that for fluids with viscosities much higher than 500 mPa·s a completely different type of dispensing system is required, usually using a piezo-driven piston mechanism to eject the fluid [139, 140].

When increasing the molecular weight of a fluid there is a transition from a droplet-on-demand (DOD) process to a volume-on-demand (VOD) deposition type. When the fluid filament touches the substrate it starts to spread on it and the filament undergoes an extensional flow. This process is no longer contactless and the filament thinning becomes coupled with the wetting dynamics on the substrate. This phenomenon of a thinning liquid bridge with moving contact lines is present in several industrial applications like offset printing and contact droplet dispensing [141, 142, 143, 144, 145], microfluidics [146], adhesion [147, 148], and in nature [2, 3]. Filament thinning dynamics and extensional rheology have been extensively studied for low viscous Newtonian and complex fluids using several techniques such as the dripping-onto-substrate (DoS) setup [141, 149, 150, 151], capillary breakup extensional rheometer (CABER) [151, 152, 153],

filament stretching rheometer (FISER) [154, 155, 156, 157] and microfluidic systems [158]. These studies provide important information regarding the thinning mechanism of the different fluids in relation to their rheological properties. At the same time research has been conducted on the spreading of droplets on solid surfaces, with different wettability properties, with attention to the evolution of the contact line and the dynamic contact angle, for fluids with different viscosities and rheology [159, 160, 161, 162, 163, 164, 165, 166, 167]. Other studies have focused on liquid transfer between surfaces through the formation of a liquid bridge. In this field extensive work, both experiments and simulations, has been done in order to correlate the material transfer ratio to the effect of pinned and free contact lines, surface wettability, contact angle hysteresis, plate separation motion and velocity, as well as deviations from axisymmetry [142, 143, 144, 168, 169, 170, 171, 172, 173, 174]. While theories, models and experimental techniques have been developed for free surface flows, as well as for dynamic wetting, the knowledge of the interplay between thinning and spreading is less mature and less studies have been devoted to this phenomenon [141, 175]. Wu et al. [141] studied the influence of wetting of non-Newtonian surfactant solutions on the extensional deformation using DoS experiments with pinned and free contact lines. They found that when increasing the concentration of surfactant there is a critical value above which wetting affects the extensional behaviour of the fluid compared to the case of pinned contact lines. The authors proposed a scaling analysis to describe the effect of wetting on the filament pinch-off based on the balance between surface tension forces and viscous dissipation inside the droplet. Qian et al. [175] investigated the deposition of droplets on a hydrophobic surface by means of the stretching of a liquid bridge created with fixed contact points at the top and a free contact line at the bottom. From the experiments they observed that after a first increase of the contact line, when a critical filament radius is reached the bridge becomes unstable and the contact line recedes rapidly. They found a good agreement between the experimental results and the numerical predictions of the bridge shape, onset of pinch-off and its behavior. In both studies different fluid viscosities and rheological behaviour, as well as different experiments, that simulate the stretching of a liquid bridge with moving contact lines, have been investigated, in order to develop fundamental knowledge of this complex phenomenon, but none of them focuses on the actual industrial process.

The aim of this work is to provide a fundamental and systematic study of the jetting of high viscous materials, which is not present in literature according to our knowledge. For this reason the piezo-driven piston dispensing system is the choice for the present work. The effect of process parameters such as the distance of the substrate from the nozzle and the molecular weight on the jetting performance of silicone fluids (polydimethylsiloxane, PDMS) has been investigated. The range of viscosities investigated, the complete wettability of the deposition substrate and high aspect ratio (> 10) used in the experiments define a parameter range not explored before. We show, in the current work, that the mutual effects of thinning and spreading, together with substrate height and viscosity are key in determining the time scale and resolution achievable during the process. We believe that the results are relevant for applications wherein precise deposition of small volumes of high viscosity fluids is required.

4.2 Materials and methods

4.2.1 Materials and material characterization

The materials investigated are silicone fluids (PDMS) (AK, Wacker Chemie AG) of different molecular weights (M_w) with the same density (ρ = 970 kg/m^3) and surface tension (σ = 0.0215 N/m), in order to systematically study the influence of viscosity and viscoelasticity on the jetting performance. As the response of the material to both shear and extension extremely is important in the process, the fluid behavior in both flows is separately investigated.

To probe the linear viscoelastic properties of the fluids, small amplitude oscillatory shear (SAOS) measurements were performed. An Anton Paar rheometer (MCR 501) equipped with a 25 mm sanded plate/plate geometry was used. The experiments were performed at 25°C, with a fixed strain of 10% and frequencies ranging from 0.03 rad/s to 628 rad/s. Storage and loss modulus curves were fitted using a multi-mode Maxwell model in order to obtain the linear viscoelastic relaxation spectrum. This model describes the viscoelastic behavior of the material using k modes in parallel, whereby each mode is composed of a spring and a dashpot connected in series [62]. The relaxation times (τ_i) and the corresponding plateau moduli (G_i) for the silicone fluids are given in Table 4.3 of Appendix 4.A. From the relaxation spectrum the viscosity average relaxation time (τ_{av}), has been calculated as:

$$\tau_{av} = \frac{\sum_{i=1}^{k} \tau_i \eta_i}{\sum_{i=1}^{k} \eta_i}, \tag{4.1}$$

where τ_i and η_i are the relaxation time and viscosity contribution of each mode, respectively. The complex viscosities obtained from the oscillatory experiments were fitted, in the shear thinning region, with a power law model [176]:

$$\eta = K\dot{\gamma}^{n-1}, \tag{4.2}$$

where η is the viscosity (Pa·s), K is the consistency of the fluid (Pa·s^n) and n is the power low index (dimensionless). For a Newtonian fluid $n = 1$, while for a shear thinning material $0 < n < 1$. From the complex viscosity it is possible to extract the zero shear viscosity of the fluids (η_0) corresponding to the plateau value at low frequencies, since these fluids obey the Cox-Merz rule [177, 178]. The viscoelastic properties and shear thinning behavior of the silicone fluids investigated are shown in Figure 4.1 (a) and Figure 4.1 (b) respectively. Table 4.1 summarizes the molecular information of the fluids (molecular weight (M_w) and polydispersity index (PDI)), and their rheological properties.

Table 4.1: Silicone fluids properties at 25°C. M_w and PDI as tabulated by the supplier.

Material	M_w [kg/mol]	PDI [-]	η_0 [Pa·s]	n [-]	τ_{av} [s]
PDMS 60	120 000	5.2	58.2	0.87	0.005
PDMS 100	130 000	5.9	100	0.73	0.01
PDMS 500	240 000	6.5	475	0.52	0.06
PDMS 1000	250 000	9.6	919	0.49	0.13

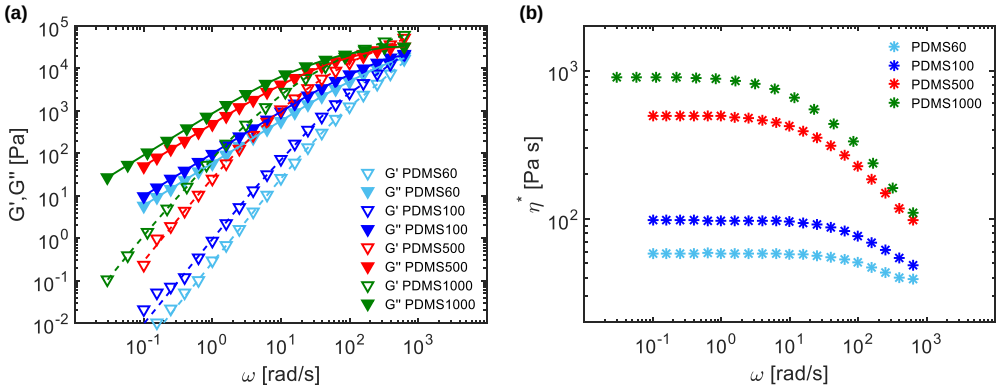

Figure 4.1: (a) Storage modulus G′ (open symbols) and loss modulus G″ (filled symbols) and multi-mode Maxwell model fitting (dashed and continuous lines). (b) Complex viscosity. (T = 25°C)

The extensional rheological properties were measured using the in-house built filament stretching rheometer (see Chapter 2), in which a 2 N force sensor (XFTC300) was mounted [101]. The sensitivity of the load cell is not high enough to accurately measure the transient extensional viscosity of PDMS 60, PDMS 100 and PDMS 500. The minimum load cell measurable force is around 0.002 N. Therefore the extensional data are only given for PDMS 1000 (Figure 4.2). Constant stretching rate experiments were performed at 1 s^{-1} and at a temperature of 25°C. A drop of silicone fluid was placed on the bottom plate and then attached to the top plate according to the procedure described in Chapter 2 [101]. The transient extensional viscosity is compared with the linear viscoelastic envelope (LVE) in order to check the presence of strain hardening and the time scales of the onset of this non linear response. The LVE envelope was calculated using the relaxation spectrum from the fitting of the SAOS data, according to the following equation [62]:

$$\eta_E^+ = 3\sum_i G_i\tau_i\left(1-\exp\left(\frac{-t}{\tau_i}\right)\right). \tag{4.3}$$

The transient extensional viscosity is calculated from the data as:

$$\eta_E^+ = \left(\frac{F_z - 1/2mg}{\dot{\epsilon}\pi D^2/4} - \frac{2\sigma}{\dot{\epsilon}D}\right)(\kappa\dot{\gamma}). \tag{4.4}$$

In the above equation F_z is the axial force measured by the load cell, g is the gravitational acceleration, m the mass of the filament, D the diameter of the midfilament point, $\dot{\epsilon}$ the strain rate, σ the surface tension and $\kappa_{\dot{\gamma}}$ is the shear correction factor [68, 69, 101]. The expression of the shear correction factor proposed by Nielsen at al. [68] is used in this work. The second term on the right side of the equation corrects for surface tension contributions that become more important at later stages of the flow.

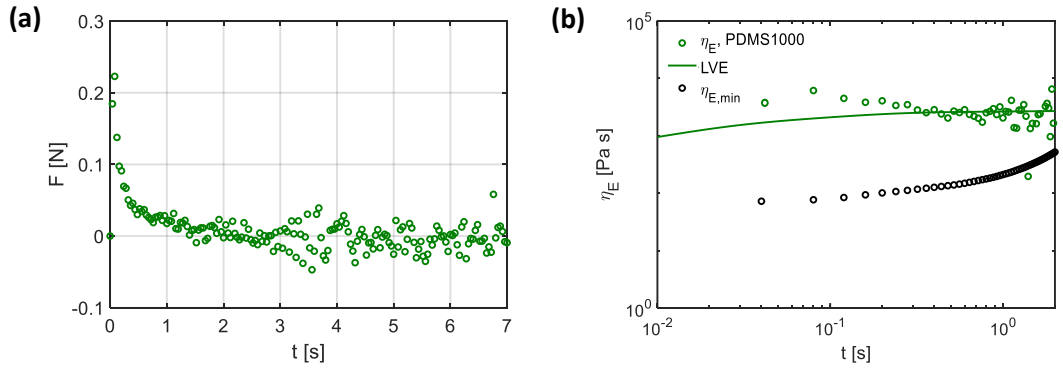

Figure 4.2: (a) Force signal during extensional deformation for PDMS 1000 at $\dot{\epsilon}$ 1 s^{-1} and 25°C. (b) Extensional viscosity of PDMS 1000 (open green symbols), minimum measurable extensional viscosity (open black symbols) and linear viscoelastic envelope (line).

To check the validity of our results we report the force signal during the experiment (Figure 4.2 (a)) and we compare the experimental extensional viscosity with the minimum value measurable (Figure 4.2 (b)) calculated as: $\eta_{E,min} = F_{min}/[(\pi D(t)^2/4)\dot{\epsilon}]$, where F_{min} is the minimum force detectable by the force sensor, $D(t)$ the experimental minimum filament diameter and $\dot{\epsilon}$ the applied strain rate. The results shown in Figure 4.2 confirm the validity of the measurements. Because at times greater than 2 s the force signal becomes too noisy, we considered for the calculation of the extensional viscosity only times up to 2 s. The extensional viscosity follows the LVE and therefore the fluid does not show any strain hardening behavior at this experimental conditions. Because of the limitation of the sensitivity of the load cell and of the maximum extension rate achievable with the instrument to perform controlled uniaxial extensional experiments, it is not possible to study the full extensional behavior of the material. Hence, the above results do not exclude non-Newtonian behavior during the thinning process, when higher transient extension rates are present.

4.2.2 Experimental setup and experimental protocol

To study the jetting performance an experimental setup has been developed (Figure 4.3 (a)). The fluid is ejected through a nozzle using a microdispensing valve (MDV 3250+ VERMES Microdispensing GmbH, externally controlled by an electronic controller MDC3200+). The valve consists of a cartridge, a fluid channel, a reservoir (just above the nozzle) and a nozzle. The fluid is inserted into the system using a pre-filled

cartridge connected to compressed air through a regulator. This allows to apply a constant pressure on the fluid that will subsequently flow and fill the fluid channel. The evolution of the jet is followed using a high speed camera (Phantom v9.0) mounted on a microscope which provides the flexibility to exchange objective lenses of different magnification. In all the experiments presented in this chapter a 5x objective lens (Olympus MSPlan5) was used. Back illumination is done with the output of a halogen source being guided by a flexible fibre optic light cable. The light is then scattered through a diffuser before shining on the sample (Figure 4.3 (b)). The microdispensing valve is mounted on a manual x-y-z stage as well as the substrate. The manual stage on which the substrate sits has a sensitivity of 1 μm for precise positioning. The substrate is a mirror polished stainless steel metal substrate chosen for its high flatness (roughness of 100 nm) which avoids stray reflections in the optical images. The experimental videos were recorded at a frame rate of 100 fps.

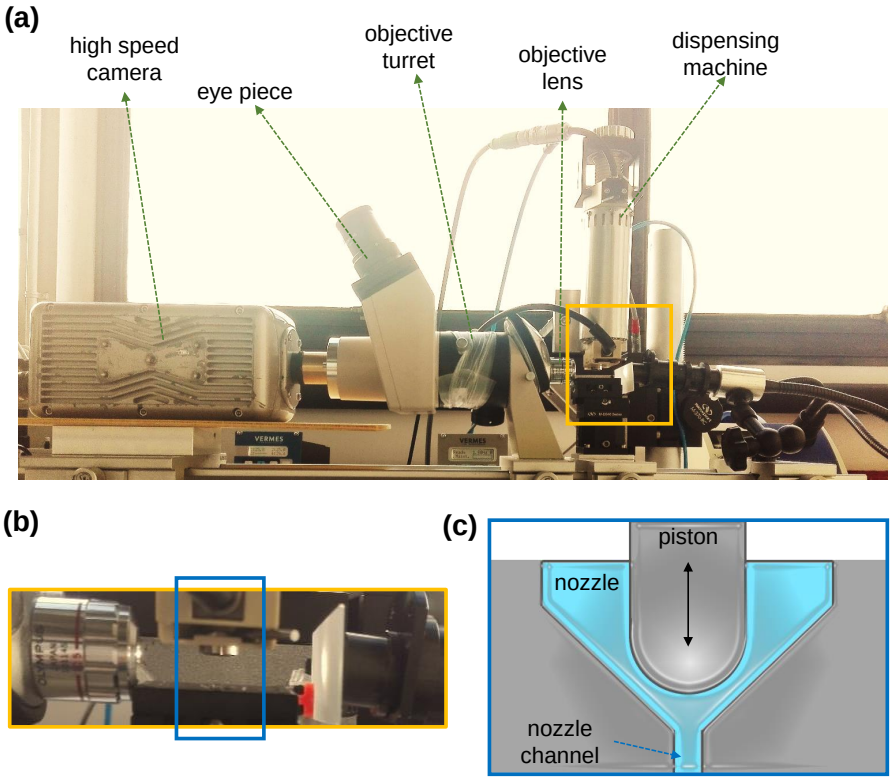

Figure 4.3: (a) Dispensing setup mounted on an optical table. (b) Inset picture showing the alignment between nozzle, light and objective lens. (c) Drawing depicting the piston movement in the nozzle.

The dispensing valve enables to work with fluids up to 2000 Pa·s thanks to a different working mechanism compared to conventional jetting machines: a small piston, driven by a piezo-element, pushes the fluid through the nozzle, see Figure 4.3 (c). This results in a very fast and precise mechanical movement of the piston/needle that is able to produce and transfer more kinetic energy to the material thereby overcoming viscous dissipation [139, 140, 179]. The electrical signal sent to the piezo-element is converted in

a trapezoidal needle lift pattern as shown in Figure 4.4. Considering the high viscosity of the fluids studied, the needle lift is set to 100%, and fixed pulse parameters were used: rising time (RI) 0.3 s, opening time (OT) 0.015 s, and falling time (FA) 0.3 s. The mentioned parameters together with the air pressure define the volume of material ejected. By experimental work the preferred set of parameters is identified. The nozzle diameter used is 100 μm and the piston diameter 1.5 mm.

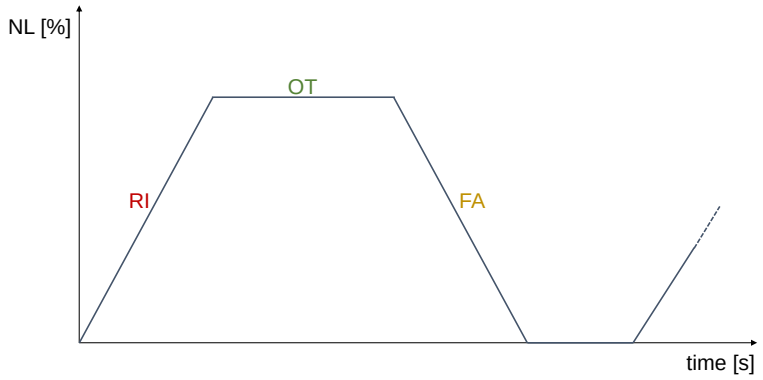

Figure 4.4: Needle lift path during a pulse.

Two main parameters were investigated in the experiments: the influence of substrate height for a specific viscosity and the influence of viscosity at a defined substrate height to filament height (h_f) ratio (h_s/h_f). The filament height is the maximum length that the filament reaches at the selected jetting parameters when no substrate is used. The experiments were performed at a temperature of 25°C. The reproducibility of the data is reported in Figure 4.20 of Appendix 4.A.

4.2.3 Data analysis

To extract quantitative information about the thinning of the filament diameter and the spreading of the fluid on the substrate, image processing is required. ImageJ software is used to convert the videos to image sequences, taking one frame out of every ten of the original video, and to estimate the volume (V) of the final droplet on the substrate, the substrate height (h_s), the breakup height (h_b) and the contact angle (θ). The volume is calculated after the filament breakup and relaxation of the filament tail into the droplet deposited on the substrate, according to the following equation for a spherical cup:

$$V = \frac{1}{6}\pi h \left(3a^2 + h^2\right). \tag{4.5}$$

where V is the volume of the droplet on the substrate, h is the height of the droplet and a is the radius of the droplet. The substrate height is the distance between the substrate and the nozzle, while the breakup height is the position, along the height of the filament, where the breakup occurs. In the present work a relative substrate height has been used and calculated as (h_s-h_b)/h_s. The contact angle is calculated using the Drop Analysis-LB-ADSA ImageJ plugin and defined as the contact angle between the tangent to the

liquid-air interface and the tangent to the liquid-solid interface. The equilibrium contact angle on the substrate is approximately 0° for all PDMS types investigated: the fluid is completely wetting the substrate. The evolution of the midfilament diameter (D) and the evolution of the contact line (cl) of the fluid with the substrate are evaluated after post processing analysis using the MATLAB® built-in Canny edge detection method.

4.3 Results and discussion

4.3.1 Rheological characterization

Because of the non-Newtonian nature of the fluids investigated, stresses accumulated during the ejection might not relax fast enough and, subsequently, may influence the thinning mechanism. Dimensional analysis is a very powerful tool in this matter, specifically, the calculation of the Weissenberg (Wi) and Deborah (De) dimensionless numbers is required. The Weissenberg number compares the elastic forces to the viscous forces and is defined as $Wi = \dot{\gamma}\tau$, where $\dot{\gamma}$ is the deformation rate and τ the relaxation time of the fluid, while the Deborah number, $De = \tau/t_{\text{flow}}$, compares the relaxation time of the material (τ) to the time scale of the flow being studied (t_{flow}). In order to understand whether the fluid is fully relaxed, the longest relaxation time needs to be considered. Furthermore a distinction between orientation and stretch of the molecules is necessary in the definition of the longest relaxation time. Orientation and stretch are characterized by the reptation time, τ_{rep}, and Rouse time, τ_{s}, respectively (Table 4.2). The relation between the aforementioned parameters for linear polymers is given by [180]:

$$\tau_{\text{s}} = \frac{\tau_{\text{rep}}}{3Z}, \tag{4.6}$$

where Z is the average number of entanglements, defined as the ratio of the average molecular weight and the molecular weight between entanglements ($Z = M_{\text{w}}/\ M_{\text{e}}$, where for PDMS M_{e} is ca. 10^4 g/mol [181]). The reptation time corresponds to the maximum relaxation time in the relaxation spectrum. Based on these time scales two different Weissennberg and Deborah numbers can be defined: Wi_{rep} and Wi_{s}, De_{rep} and De_{s} (Table 4.2). When $Wi_{\text{rep}} < 1$ and $Wi_{\text{s}} < 1$, the flow is very weak and the material is in its equilibrium state (coil state), if $Wi_{\text{rep}} > 1$ and $Wi_{\text{s}} < 1$, the chains are oriented in the direction of the flow, if $Wi_{\text{rep}} > 1$ and $Wi_{\text{s}} > 1$ the flow is strong enough to orient and stretch the chains. Despite the fact that the Weissenberg number provides information regarding the strength of the flow and the consequent orientation of the chains, it is necessary to consider the Deborah number to evaluate if the elasticity plays a role in the time frame of the applied deformation.

The flow in the fluid nozzle channel can be simplified as a capillary flow in which the Weissenberg-Rabinowitsch equation for non-Newtonian fluidn [62], can be applied in

order to estimate the shear rates ($\dot{\gamma}$) in the nozzle (Table 4.2):

$$\dot{\gamma} = \frac{8Q}{\pi d^3}\left(3 + \frac{1}{n}\right), \tag{4.7}$$

where Q is the volumetric flow rate, d the diameter of the nozzle and n the power law index. Because it is not possible to follow the movement of the piston within the VERMES dispensing setup, the flow rate in the nozzle has been back calculated from the velocity of the jet:

$$Q = \frac{\pi d^2}{4} v_{\text{jet}}. \tag{4.8}$$

In the above equation d is the nozzle diameter and v_{jet} is the arithmetic average jet velocity. The order of magnitude of this velocity is 0.01 m/s with values that slightly increase with increasing viscosity. This effect despite being counter-intuitive could be related to the fact that with increasing viscosity more energy is required to push the fluid through the nozzle and therefore most of the material is pushed almost at the end. The shear rates estimated with Eqn. 4.7 are used to calculate the Weissenberg numbers, while the time required for the jet to touch the substrate is used to calculate the Deborah numbers.

Table 4.2: Fluids relaxation times, shear rates and dimensionless numbers in the nozzle channel.

Material	τ_{rep} [s]	τ_{s} [s]	$\dot{\gamma}$ [s^{-1}]	Wi_{rep} [-]	Wi_{s} [-]	De_{rep} [-]	De_{s} [-]
PDMS60	0.04	0.001	42.3	1.69	0.04	0.15	0.004
PDMS100	0.13	0.003	73.9	9.61	0.22	0.72	0.02
PDMS500	0.64	0.031	130.7	83.65	4.05	4.26	0.06
PDMS1000	3.56	0.048	297	1057.32	14.26	39.56	0.53

Figure 4.5 shows image sequences of the dispensing of the jet from the nozzle onto the substrate. In agreement with the dimensional analysis the experiments confirm that at increasing molecular weight the fluid elasticity and orientation become predominant. As a consequence Wi is very high and $De_{\text{rep}} > 1$ for PDMS 500 and PDMS 1000. This is reflected in a less glossy jet and increasing surface instability with increasing molecular weight. The critical Wi_{s} for sharkskin flow instabilities is known to be around 3-7 [182]. In our experiments Wi_{s} for PDMS 500 and PDMS 1000 are above the critical value as confirmation of the flow instabilities observed at the exit of the nozzle. A time comparable to the reptation time is required to relax the flow instabilities after ejection from the nozzle. For the high M_{w} PDMS the elastic stresses have not yet relaxed when the filament reaches the substrate.

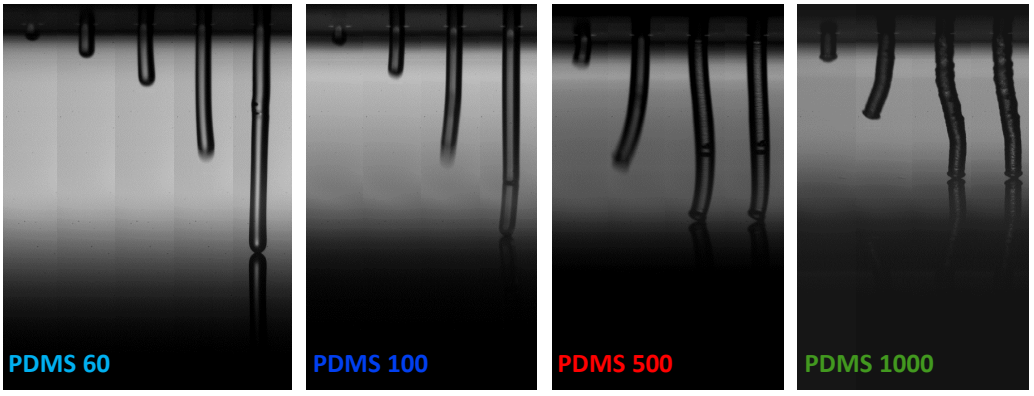

Figure 4.5: Dispensing of the jet on the substrate (at $h_s = h_f$) highlighting the influence of viscoelasticity on the flow instability.

4.3.2 Influence of substrate height

4.3.2.1 Filament thinning behavior

In deposition technologies the distance between the substrate and the nozzle plays an important role (e.g. in droplet formation, velocity impact, spreading, splashing, etc.). Because materials of such high viscosity, as used in this study, have never been extensively investigated and/or employed in jetting technologies, we first analyzed the influence of the substrate height on the jetting performance of PDMS 60. Figure 4.6 (a) shows image sequences of the volume on demand deposition process for different substrate heights, from the instant at which the jet touches the substrate till breakup of the filament. It is possible to observe that when the distance to the substrate is smaller than the filament length, the fluid buckles once in contact with the substrate. The tip of the jet impacts on the substrate with a certain velocity and, because of the high viscosity, it can not instantaneously spread on the substrate causing a constraint on the material which ends up pinned on the substrate. When $h_s < h_f$ this results in buckling: the fluid touches the substrate before the dispensing process is completed, therefore the fluid ejected after the contact together with the initial pinned condition of the fluid on the substrate causes the buckling. For analysis purposes the frames in which the fluid buckles have not been taken into inconsideration. Figure 4.6 (b) and Figure 4.6 (c) show the evolution of the thinnest diameter over time and the deformation rates ($\dot{\epsilon}$ = -2/$D(t)$d$D(t)$/dt) developed during the thinning process, respectively.

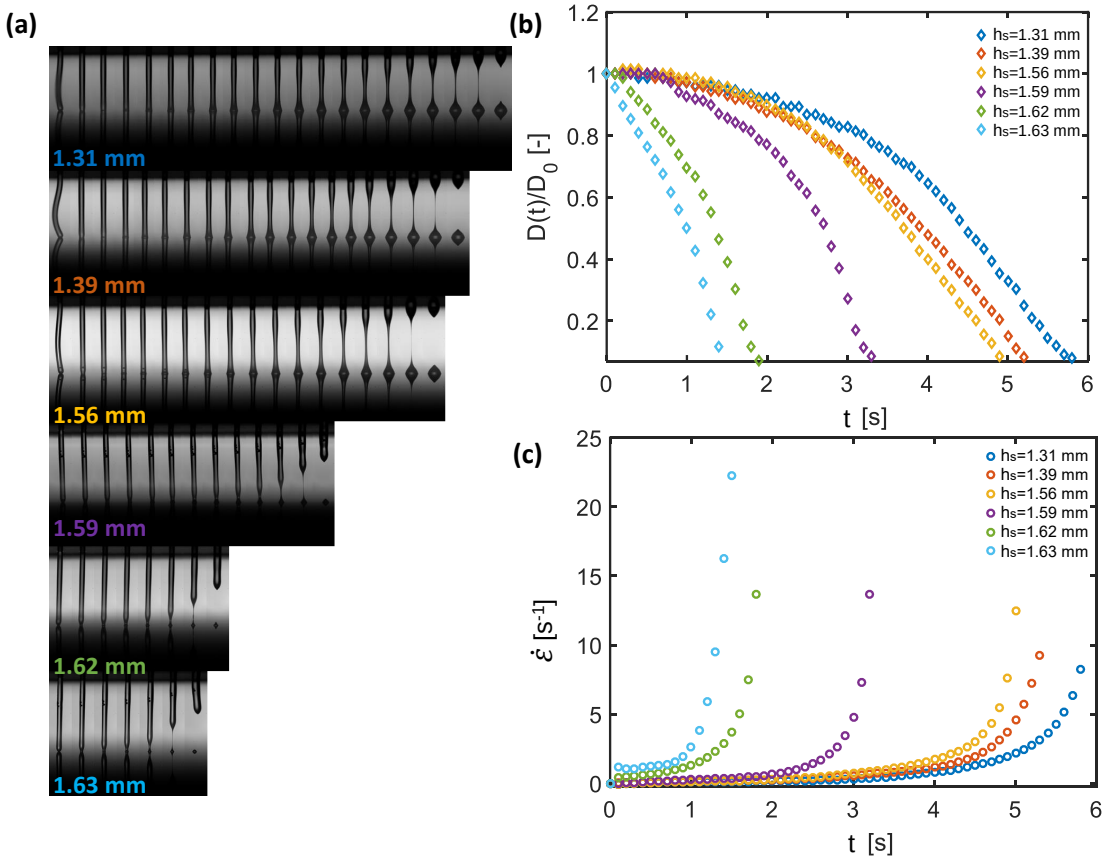

Figure 4.6: Influence of the substrate height on the filament thinning for PDMS 60. (a) Image sequences of the thinning process with increasing substrate height from top to bottom, $\Delta t = 0.3$ s. (b) Evolution of the diameter and (c) extension rate during the process.

It is possible to observe that the substrate height has a great impact on the time scale (Figure 4.6 (b)) and on the resolution of the process (Figure 4.6 (a)) with the time scale reducing and the resolution increasing, respectively, when moving the substrate further apart from the nozzle. The difference in time to breakup (t_b) is the consequence of the deformation rate selected by the fluid itself during the thinning process, which increases with increasing substrate height (Figure 4.6 (c)). The effect of substrate height on the volume deposited and the process time is more clearly visible in Figure 4.7 (a), where a transition in dependence can be observed at 1.56 mm $< h_s <$ 1.59 mm, defining two distinct regions: region I for $h_s \leqslant 1.56$ mm and region II for $h_s > 1.56$ mm. The substrate height influences also the position of the breakup along the height of the filament as can be observed in Figure 4.7 (b), where the relative breakup height decreases with the distance between the substrate and the nozzle, thereby indicating that the breakup point is shifting closer to the substrate. Also in this case two distinct regions are present with a transition from region I to region II at 1.56 mm $< h_s <$ 1.59 mm. In region I the relative breakup height remains approximately constant. This can be explained considering that at lower h_s a higher volume is transferred to the substrate at the early stages of the deposition, due to more pronounced buckling. This pulls the filament

towards the substrate affecting the breakup position. This effect disappears when the substrate height is sufficient enough to suppress excessive buckling, and the relative breakup height decreases linearly when moving the substrate further from the nozzle.

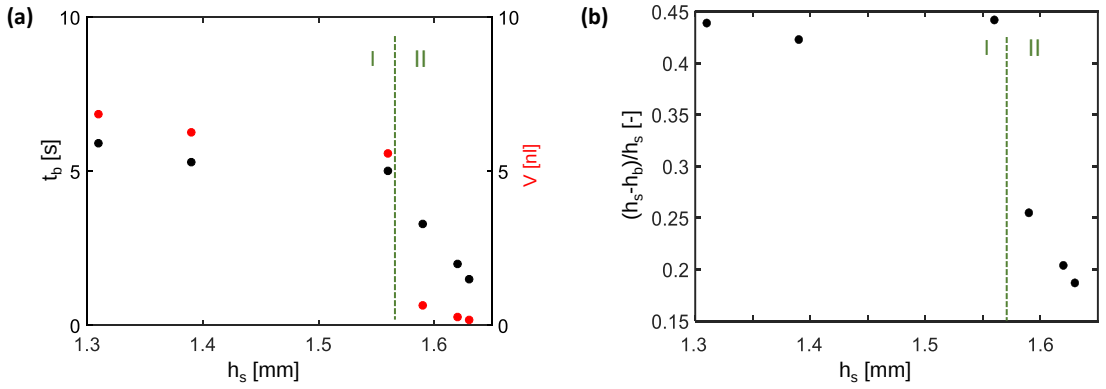

Figure 4.7: (a) Time to breakup and deposited volume as function of substrate height. (b) Relative breakup height as function of substrate height. (PDMS 60)

In order to fully understand these phenomena we approached the problem with a dimensional analysis attempting to apply the well defined theories for thinning processes. A free surface and self-thinning flow is driven by surface tension and resisted by inertia, viscosity and elasticity. The competition between the acting forces can be evaluated using dimensionless numbers [149, 150, 183, 184]: the Ohnesorge number, $Oh = \eta_0/(\rho\sigma R)^{1/2}$, defines the ratio of viscous to inertial and surface forces, the intrinsic Deborah number, $De_0 = \tau/(\rho R^3/\sigma)^{1/2}$, represents the ratio of the polymer relaxation time to the time scale of the flow and thus the competition between elastic and inertial forces, and the elasto-capillary number, $Ec = \tau\sigma/\eta_0 R$, defines the balance between elasticity and viscous forces. In these dimensionless numbers η_0 is the zero shear viscosity, ρ the density, σ the surface tension, τ the Rouse time and R the instantaneous radius of the filament. The choice of R as characteristic length allows us to estimate local values of the dimensionless numbers and if and when a transition from one regime to the other occurs [184]. Based on the predominant resisting force three different thinning mechanisms can be defined, each described by a specific diameter evolution. The inertio-capillary regime is present when $Oh \ll 1$ and $De \ll 1$, for low viscous and inelastic fluids, and the diameter decreases with a power law [149]:

$$\frac{D(t)}{D_0} = 0.8 \left(\frac{\sigma}{\rho {D_0}^3}\right)^{1/3} (t_\mathrm{b} - t)^{2/3}, \tag{4.9}$$

For viscous and inelastic fluids with $Oh \gg 1$ and $Ec \ll 1$, the thinning regime is visco-capillary and the filament diameter decreases linearly in time [149]:

$$\frac{D(t)}{D_0} = 0.0709 \left(\frac{\sigma}{\rho D_0}\right) (t_\mathrm{b} - t)\,, \tag{4.10}$$

When the elasticity becomes predominant and $Ec > 4.7$ [184] the thinning regime is elasto-capillary and can be described by an exponential decrease of the filament diameter [149]:

$$\frac{D(t)}{D_0} = \left(\frac{GD_0}{2\sigma}\right)^{1/3} \exp\left(-\frac{t}{3\tau}\right). \tag{4.11}$$

In all the above equations D_0 is the initial filament diameter and t_b the filament breakup time. For the specific case studied the dimensional analysis established that viscosity is the resisting force in the thinning process with $Oh \gg 1$, $De \ll$ and $Ec \ll 1$, thus the thinning should follow the visco-capillary regime.

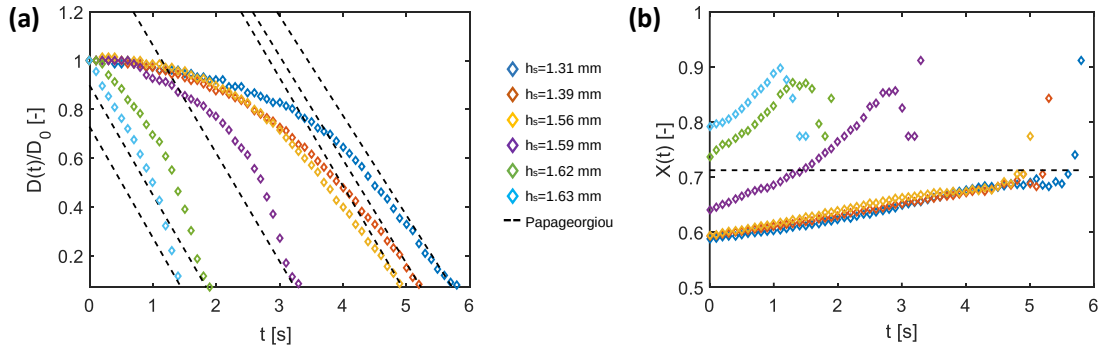

Figure 4.8: (a) Visco-capillary prediction of the filament diameter evolution. (b) Comparison of the experimental value of $X(t)$ for different substrate heights and the constant value from Papageorgiou [154]. (PDMS 60)

Predictions of the filament diameter evolution according to Eqn. 4.10 have been attempted and the results are shown in Figure 4.8 (a). The visco-capillary regime seems to not properly predict the experimental results not even at the later stages of the process when the effect of the initial geometry and the jetting itself should have disappeared. In order to understand whether a new prefactor is required in Eqn. 4.10 we compare its experimental value with the theoretical one based on the Papageorgiou analysis [154]. Eqn. 4.10 can be rewritten as follows:

$$\frac{D(t)}{D_0} = a\left(\frac{\sigma}{\rho D_0}\right)(t_b - t), \tag{4.12}$$

where $a(t) = (2X(t)\text{-}1)/6$, and $X(t) = F_z(t)/2\pi\sigma R(t)$, where $F_z(t)$ is the axial force at the midfilament point over time. For Newtonian fluids and an ideal axially uniform filament the value of $X(t)$ is equal to 1, and no longitudinal stresses are developed. In reality there are axial variations in the shape leading to effects that are described by the evolution in time of the tensile force $F_z(t)$. In case of viscous filaments with a smooth neck profile and no inertia Papageorgiou found that $X = 0.7127$ [154]. The comparison between the

experimental *X(t)* and the constant value from the Papageorgiou self-similar solution shows how the substrate distance from the nozzle influences the thinning mechanism, determining the formation of two regions (see Figure 4.8 (b)). In region I, for low substrate heights ($h_s \leqslant 1.56$ mm), the temporal evolution of *X(t)* is mostly linear with a steep increase in slope a few instants before breakup. In region II ($hs > 1.56$ mm) a different evolution of *X(t)* can be observed, with a presence of a maximum before breakup and overall higher values than the Papageorgiou constant indicating that higher axial stresses accumulated in the filament during the extensional flow. This may be related to the small fluid volume below the breakup point and pullback force of the upper filament. In all the experimental conditions *X(t)* changes in time and never approaches a constant value, therefore confirming that the data do not obey to the Papageorgiou self-similar solution.

It is clear that the filament thinning cannot be described according to the well known thinning theories for the whole range of substrate heights investigated. These results contradict previous works in which breakup experiments have been performed on a low viscosity PDMS [154] and a high viscosity PDMS [4], both showing a visco-capillary thinning according to Eqn. 4.10. This discrepancy can be explained considering the different nature of the problem investigated compared to capillary breakup experiments, in particular the higher aspect ratio and moving contact line, and thus the effect that the spreading on the substrate can have on the breakup process.

The change in thinning behavior observable at a substrate height higher than 1.56 mm has already been observed in Figure 4.7 and it is, once again, confirmed by plotting the evolution of the dimensionless diameter as a function of the experimental time scaled with the time to breakup (Figure 4.9), where it is possible to distinguish two different thinning slopes belonging to the two regions. The above results suggest that with changing substrate height the transient interaction between fluid and substrate is different and this could influence the thinning phenomenon thereby supporting the previous hypothesis of the influence of the moving contact line on the filament thinning.

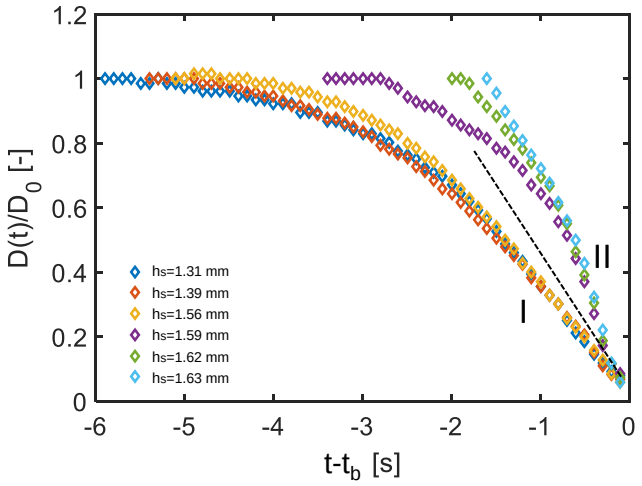

Figure 4.9: Evolution of the normalized diameter as function of the scaled time with the time to breakup. (PDMS 60)

4.3.3 Spreading behavior

To understand the influence of the moving contact lines on the thinning process, an analysis of the spreading behaviour is performed. When a droplet is not free to move on a substrate, like a sessile droplet, but is connected to a liquid bridge, the spreading dynamics results from a balance of interfacial stresses (determined by the affinity with the substrate), gravity, inertia, viscous and normal stresses in the bulk of the droplet and stresses developed in the filament [141]. Viscous stresses in the droplet and stresses in the filament decrease the spreading. To study the process an analysis of the moving contact lines (cl) and of the dynamic contact angle (θ) is required (see Figure 4.10 (a)). From Figure 4.10 the evolution of the contact line follows two distinct behaviors defining, once again, two regions. Region I, at lower substrate height ($h_s \leqslant 1.56$ mm), is characterized by a faster spreading than region II ($h_s > 1.56$ mm) where the increase of the contact line is slower. The difference in slope can be attributed to the size of the droplet in contact with the substrate: for smaller droplet sizes the spreading is known to be slower [185]. In region II also a different spreading behavior can be observed, the contact line plateaus for a short time before increasing again close to the breakup time. Wetting theories have been developed to describe the spreading behavior of Newtonian and non-Newtonian fluids through a generic power law equation: $R(t) \propto t^{\alpha}$, where the exponent α assumes different values according to the nature of the fluid employed and the dominant forces during spreading [141]. In our case the data cannot be fitted with the traditional wetting theories.

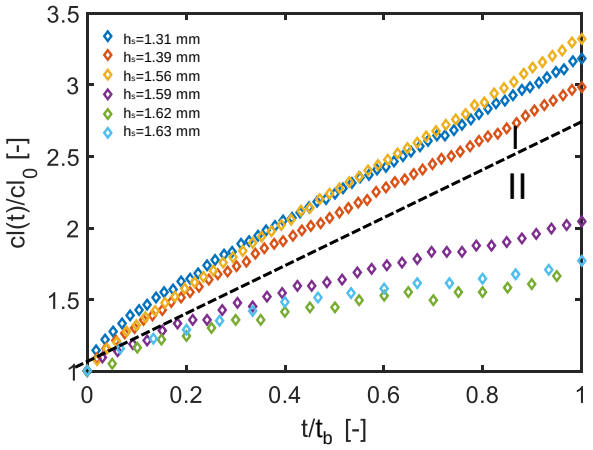

Figure 4.10: Evolution of the normalized contact line as function of the time normalized with the time to breakup.

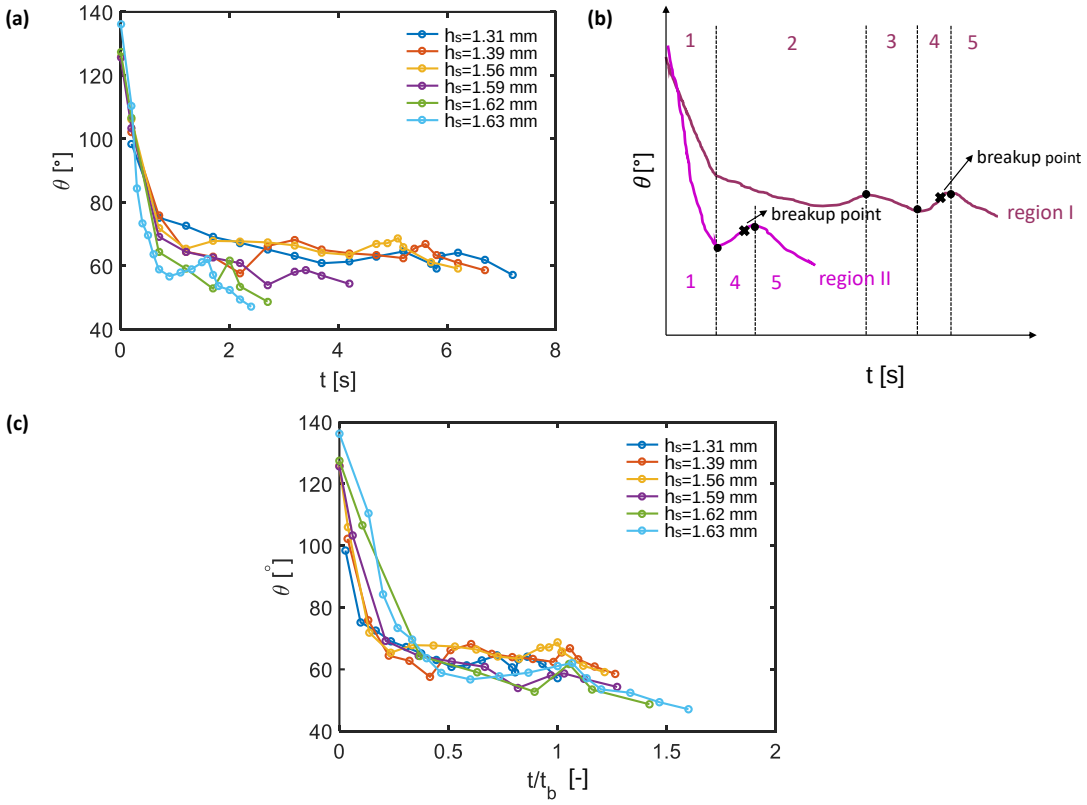

Figure 4.11: (a) Evolution of the dynamic contact angle. (b) Schematic representation of the evolution of the dynamic contact angle over time. (PDMS 60). (c) Evolution of the dynamic contact angle as function of the normalized time too the time to breakup

The evolution of the dynamic contact angle at different substrate heights is reported in Figure 4.11 (a) as function of time to better show change in its evolution with different substrate heights. When the fluid filament touches the substrate the contact angle is much higher than its value at equilibrium, thus the material starts to spread in order to minimize this difference [164, 185]. For values of $h_s \leqslant 1.56$ mm 5 phases can be individuated before breakup: during phase 1 the contact angle decreases rapidly due to the drive to minimization of the high energy state, in phase 2 the contact angle decreases much more slowly and increases during the later stage of it reaching a maximum before phase 3 during which the contact angle decreases again, reaching a minimum that signs the start of phase 4 that ends a few instants after the breakup when the contact angle reaches a new local maximum. Subsequently the dynamic contact angle again decreases towards its equilibrium value, in phase 5. The last phase can be treated as the well known spreading of a sessile droplet. With increasing substrate height the life time of phase 2 becomes shorter while phase 3 extends till they both disappear for $h_s > 1.59$ mm, and the dynamic contact angle evolution is described by phases 1, 4 and 5. A schematic representation of the dynamic contact angle evolution in region I and region II is available in Figure 4.11 (b), while Figure 4.11 (c) highlights the maximum in dynamic contact angles at values around t/t_b approximately equal to 1. The increase and decrease of the contact angle is not reflected in a receding of the contact lines that are continuously increasing over time, as shown before. A similar behavior of the dynamic contact angle has been observed by Šikalo et al. [186] for the spreading of a droplet of glycerin impacting on a glass. In the initial state of spreading the dynamic contact angle decreases till a minimum, then it starts rising again till it reaches a local maximum and then it decreases again. During these phases of spreading the contact line monotonically increases until the instant at which the dynamic contact angle is at its maximum value. After that it stays approximately constant. The behaviour is the same at different impact velocities, but the local minimum and maximum in the value of the contact angle occur at earlier times for lower impact velocities. Šikalo et al. [186] and Blake et al. [187] recognized that it is not always possible to correlate the dynamic contact angle with the spreading velocity. They argued that this phenomenon is the result of the flow field generated in the vicinity of the moving contact line. It is highly possible that the different impact velocities (at different substrate heights) as well as different initial contact areas between fluid and substrate might definitely affect this local flow fields influencing the dynamic contact angle evolution. Despite this, the different phases recognized in Figure 4.11 (b) could be the result of a combination of the different flow field at the contact line edge and the filament thinning itself.

In order to get a better understanding of the spreading process the contribution of each of the acting forces and possible non-Newtonian effects is estimated. To take possible non-Newtonian effects into consideration the spreading shear rate ($\dot{\gamma} = 1/cl(t)\mathrm{d}cl(t)/\mathrm{d}t$) is estimated from the evolution of the contact line. The maximum shear rate, that develops at the beginning of the process is always smaller than the onset of shear thinning. Moreover, the axial stresses at these shear rates are negligible indicating that no bulk viscoelasticity developed during spreading. In order to evaluate the importance of gravity, inertia and capillarity a dimensional analysis is performed. The Bond number, $Bo = 4\rho g R(t)^2/\sigma$, defines the importance of gravity over surface tension, while the

Reynolds number, $Re = \rho U R(t)/\eta$ represents the competition between inertia and viscosity. Furthermore the competition between viscous dissipation in the droplet and wetting forces can be expressed through the Capillary number, $Ca = \eta U/\sigma$, where U is the spreading velocity calculated as: $U = \mathrm{d}cl/\mathrm{d}t$. In the mentioned dimensionless number $R(t)$ is the radius of the droplet in contact with the substrate. For all the experiments Bo and Re are smaller than unity indicating that gravity and inertia forces are negligible. The Capillary number is greater than 0.1 at the first instants of the spreading and decreases for all substrate heights investigated, but in the later stages it returns to a value of approximately 0.1 for h_s belonging to region I. Overall the values of Ca for region I are much higher than those for region II and always very close to 0.1 suggesting that the spreading should be slower in region I. Values of Ca of approximately 0.1 indicate that viscous forces are predominant in the spreading phenomenon while resisting the latter. This result contradicts the evolution of the contact line observed in Figure 4.10 suggesting that indeed spreading cannot be studied as a phenomenon by itself and a link with filament thinning might exist.

The axial force that may develop in the connected filament and slows the spreading is compared with the capillary force that, in opposite, promotes spreading using the dimensionless ratio r. The mentioned ratio can be calculated as:

$$r = \frac{\eta_{\mathrm{E}} \dot{\epsilon} \pi D^2/4}{2\sigma cl}, \tag{4.13}$$

where D is the midfilament diameter and cl is the contact line of the droplet.

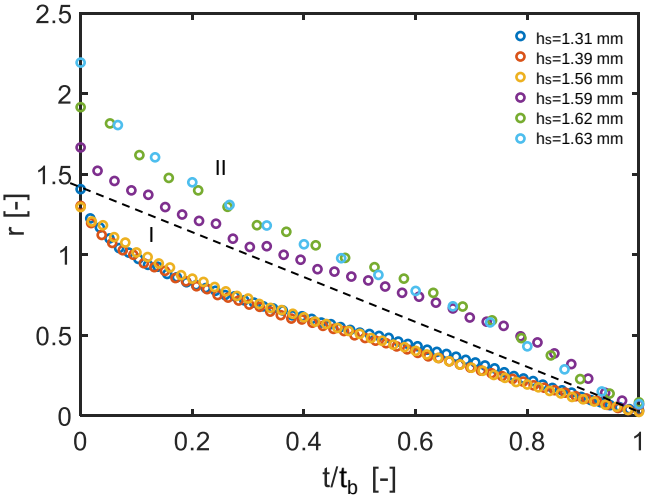

Figure 4.12: Evolution of the filament axial forces to droplet capillary contribution ratio as function of the time normalized by the time to breakup. (PDMS 60)

Figure 4.12 shows the evolution of r for the different substrate heights. Once again it is possible to observe two different behaviors corresponding to what was defined earlier in the chapter as region I and region II. When the substrate height falls in region I ($h_s \leqslant$

1.56 mm) the interplay between axial forces in the filament and spreading is independent of the actual substrate height and the spreading results to be the main driving force. This is confirmed by values of r decreasing over time and, excluding the initial instants after impact of the fluid on the substrate, r < 1. In region II ($h_s > 1.56$ mm) instead, the pulling upward of the filament is dominating, as confirmed by fast thinning, high extensional rates and slow spreading. As a consequence the axial forces in the filament dominate over the capillary forces that should promote spreading. While studying the filament thinning and spreading separately does not provide clear information on the underlining process the evolution of the contact angle and the ratio r reveal the crucial role that the substrate to nozzle distance plays in the dispensing process.

4.3.4 Influence of viscosity

4.3.4.1 Filament thinning behavior

To study the influence of viscosity, PDMS samples of increased molecular weight have been used (see Section 4.2.1). Based on the results shown above regarding the influence of substrate height, we chose to perform experiments at a value of h_s approximately equal to the filament height (region II as defined in Section 4.3.2.1), that differ for the different viscosities as can be observed from Figure 4.5, thereby eliminating the effect of the substrate-nozzle distance and achieving higher resolution and a faster process for each of the fluids investigated.

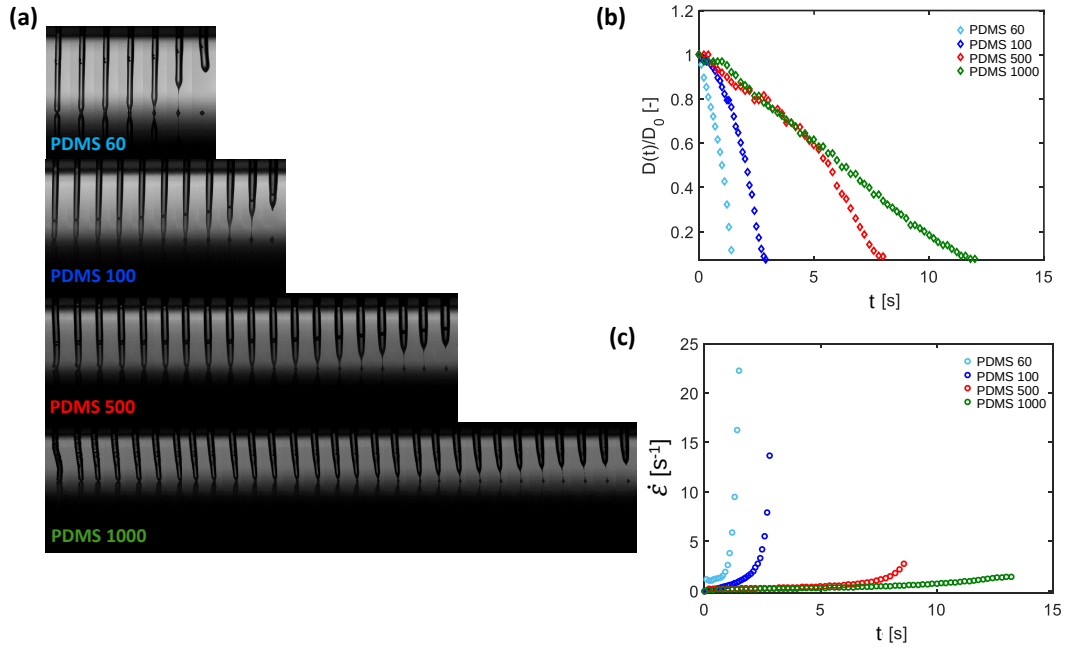

Figure 4.13: Filament thinning for PDMS with different viscosities at $h_s/h_f = 0.99$. (a) Image sequences of the filament thinning process with increasing viscosity from top to bottom, $\Delta t = 0.3$ s for PDMS 60 and PDMS 100, $\Delta t = 0.5$ for PDMS 500 and PDMS 1000. (b) Evolution of the diameter and (c) extension rate during the process.

From the image sequence in Figure 4.13 (a) it is possible to notice the effect that the increase in viscosity has on the resolution and on the position of the breakup point along the filament height. The evolution of the midfilament (Figure 4.13 (b)) underlines the increase of the time to breakup with increasing viscosity. The deformation rates (Figure 4.13 (c)) developed during the thinning become more than 50% smaller for PDMS 500 and PDMS 1000, indicating that a much stronger force is acting against thinning itself. The results in terms of volume deposited, time to breakup and breakup height are summarized in Figure 4.14. The volume of the droplet on the substrate decreases with viscosity while the time to breakup increases, the position of the breakup also shifts closer to the substrate with increasing viscosity.

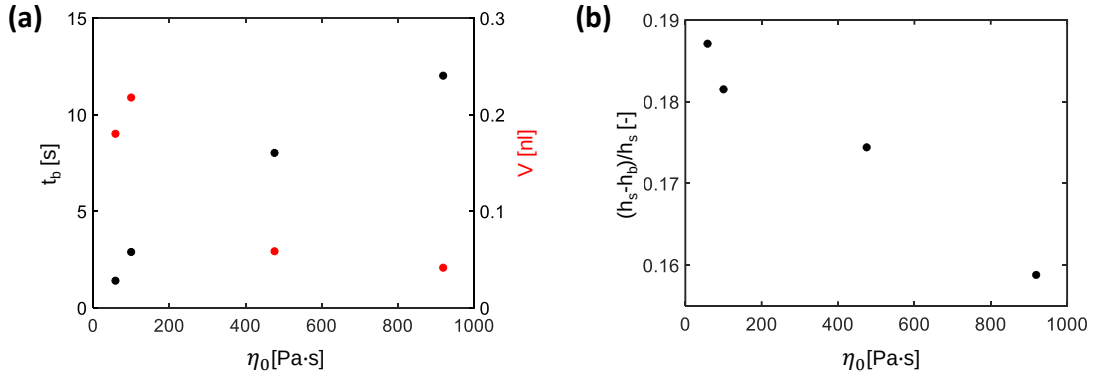

Figure 4.14: (a) Time to breakup and deposited volume as function of fluid viscosity. (b) Relative breakup height as function of fluid viscosity. ($h_s/h_f = 0.99$)

To understand which are the dominant forces acting against the filament thinning, the same dimensional analysis described in Section 4.3.2.1 has been performed. The calculation of the dimensionless numbers suggests that for all the investigated PDMS types viscosity is the dominant resisting force thus the thinning mechanism is visco-capillary driven. To determine whether or not the Papageorgiou prediction of the evolution of the midfilament diameter is applicable to the thinning of samples with different viscosities we compared the theoretical diameter evolution with the experimental one. The results of this comparison are reported in Figure 4.15. The difference between the experimental data and the theoretical prediction increases with viscosity (Figure 4.15 (a)). When the M_w increases the evolution of *X(t)* shows a less pronounced peak before breakup while it completely disappears for the highest viscosity investigated in Figure 4.15 (b)). When using PDMS 1000 the initial value of *X(t)* is the highest and it stays constant for almost the entire experiment. Being *X(t)* related to the axial force generated in the filament during the extensional flow while thinning, the results for PDMS 1000 suggest that already at the beginning of the deposition process the material has high stresses accumulated, as a result of the flow instabilities mentioned in Section 4.3.1 and possible axial variations in the filament shape that might induce higher accumulated local stresses.

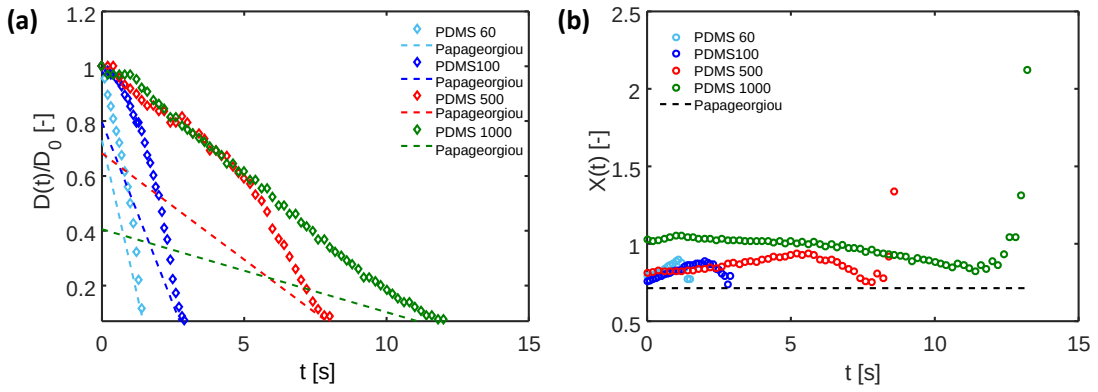

Figure 4.15: (a) Visco-capillary prediction of the filament diameter evolution. (b) Comparison of the experimental value of $X(t) = F_z(t)/2\pi\sigma R(t)$ for different viscosities, at $h_s/h_f = 0.99$, and the constant value from the Papageorgiou analysis.

To determine if it is possible to distinguish different regimes in the thinning behavior of the filament the dimensionless diameter is plotted as function of the dimensionless time $(t\text{-}t_b)\sigma/\eta D_0$.

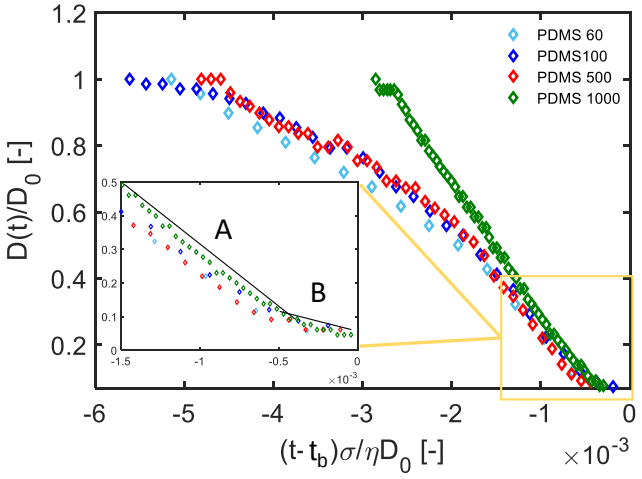

Figure 4.16: Evolution of the dimensionless minimum diameter as function of the dimensionless time for different viscosities at $h_s/h_f = 0.99$. Inset shows the transition from region A to B at later stages of the filament thinning process.

The above figure underlines the formation of different thinning stages with increasing viscosity. Closer to the breakup event the filament thinning becomes relatively slower. Good agreement is found for the different PDMS samples used, this suggests that the process is strictly influenced by the dynamic contact with the substrate. Using the same h_s/h_f ratio for all PDMS samples investigated ensures that the only effect influencing

the process is the viscosity. This slows down the overall process without contributing to a change in thinning dynamics. This is confirmed by the experiments shown in Figure 4.21 and Figure 4.22 of Appendix 4.A for PDMS 1000 at different substrate heights. Two regimes are present and the transition between them occurs at a value of $h_s/h_f > 0.97$ that is slightly higher than the $h_s/h_f > 0.95$ found in the case of PDMS 60.

4.3.4.2 Spreading behavior

To confirm the above hypothesis that the h_s/h_f is the only parameter affecting the process, a detailed analysis of the spreading behavior is required. We start evaluating the evolution of the contract line and of the dynamic contact angle, see Figure 4.17 (a) and Figure 4.18 respectively. The spreading becomes slower with increasing viscosity as suggested by the evolution of the contact line, in case of PDMS 1000 the velocity reaches a plateau at the end of the filament thinning process. A decreasing spreading velocity with increasing viscosity has been observed for the spreading of sessile droplets as well [166].

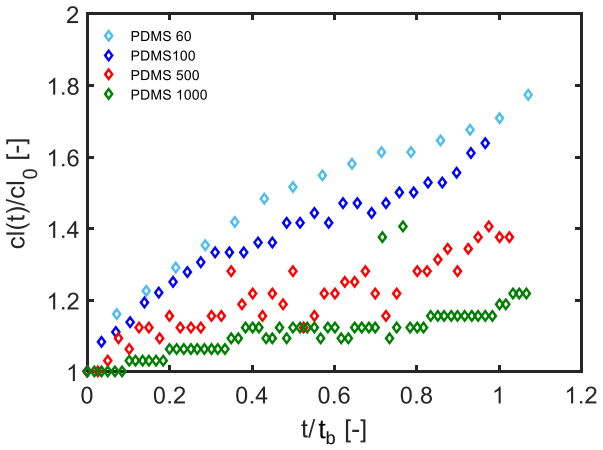

Figure 4.17: Evolution of the normalized contact line as function of the time normalized with the time to breakup. ($h_s/h_f = 0.99$)

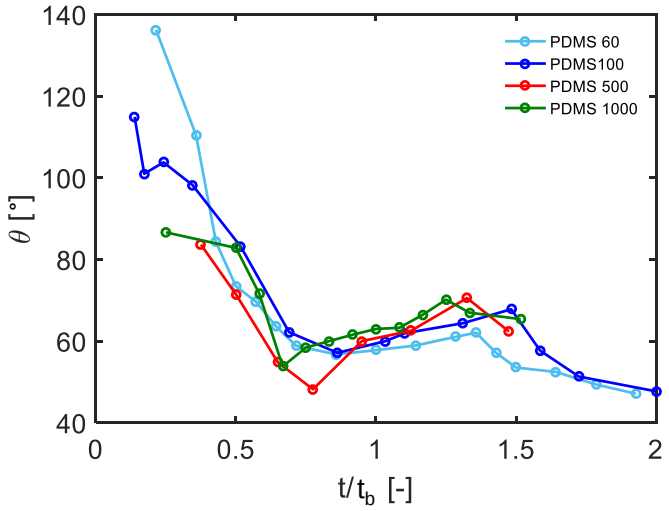

Figure 4.18: Evolution of the dynamic contact angle as function of the normalized time normalized by the time to breakup for different viscosities at $h_s/h_f = 0.99$.

The dynamic contact angle shows the 3 stage evolution for all viscosities, as observed for $h_s > 1.59$ mm in Section 4.3.3. The contact angle first decreases fast to reach the equilibrium condition, at later stages of the process it starts to increase to reach a maximum after the breakup point, subsequently it decreases towards the static value. To analyze the spreading behavior in more detail we used the same approach described in Section 4.3.3. The dimensional analysis suggests that gravity, inertia and viscous forces are small enough to be ignored. The evolution of the dimensionless ratio r (Figure 4.19) shows that the balance of axial to capillary forces is independent of viscosity and at the chosen h_s/h_f the axial stresses dominate for about half of the thinning process. This independence of r from viscosity suggests that when increasing viscosity the increased relaxation time, with consequent lower stretch rate in the filament, and higher viscous dissipation in the droplet balance each other resulting in an unchanged dispensing process.

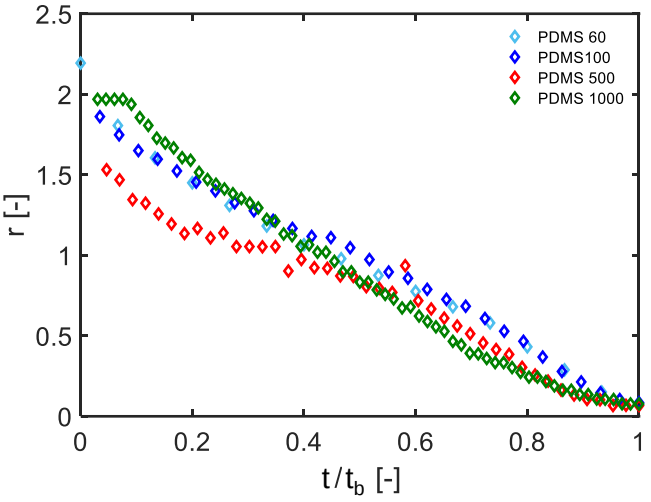

Figure 4.19: Evolution of the dimensionless ratio r for different viscosity at $h_s/h_f = 0.99$.

4.4 Conclusions

We have studied for the first time the jetting behavior of extremely high viscous fluids, with particular interest in the influence of the substrate to nozzle distance and the molecular weight on the jetting performance. First of all, a transition from droplet-on-demand to volume-on-demand is observed when the viscosity is very high. This transition determines the development of a different fluid dynamics problem wherein the interplay between spreading of the fluid on the substrate and filament thinning determines the processing behavior. At constant fluid viscosity the substrate height becomes crucial in defining the resolution and process time scale: moving further from the nozzle generates smaller deposited droplets in a shorter time. The stresses developed in the filament compete with the spreading capillary forces affecting the evolution of the contact angle. Increasing the viscosity increases the processing time and resolution, while the balance between stresses in the fluid and spreading remains unaltered when the substrate height to filament height ratio is kept constant. These results provide more understanding of the jetting of high viscous fluids. Despite the very long process timescale the results are of importance for industrial applications wherein a small volume of high viscous materials has to be precisely deposited without changing the properties during printing (e.g. reducing viscosity).

4.A Appendix

Table 4.3: Relaxation spectrum of silicone fluids measured at 25°C.

PDMS 60			PDMS 100			PDMS 500			PDMS 1000		
mode	τ_i [s]	G_i [Pa]	mode	τ_i [s]	G_i [Pa]	mode	τ_i [s]	G_i [Pa]	mode	τ_i [s]	G_i [Pa]
1	0.00118	$3.58{\cdot}10^4$	1	0.00146	$4.02{\cdot}10^4$	1	0.000693	$7.00{\cdot}10^4$	1	0.00176	$5.95{\cdot}10^4$
2	0.00958	$1.47{\cdot}10^3$	2	0.0131	$2.78{\cdot}10^3$	2	0.0073	$2.49{\cdot}10^4$	2	0.012	$2.33{\cdot}10^4$
3	0.036	60.9	3	0.13	22.3	3	0.0414	$4.51{\cdot}10^3$	3	0.0637	$5.57{\cdot}10^3$
						4	0.229	279	4	0.348	428
						5	2.26	1.28	5	3.56	3.1

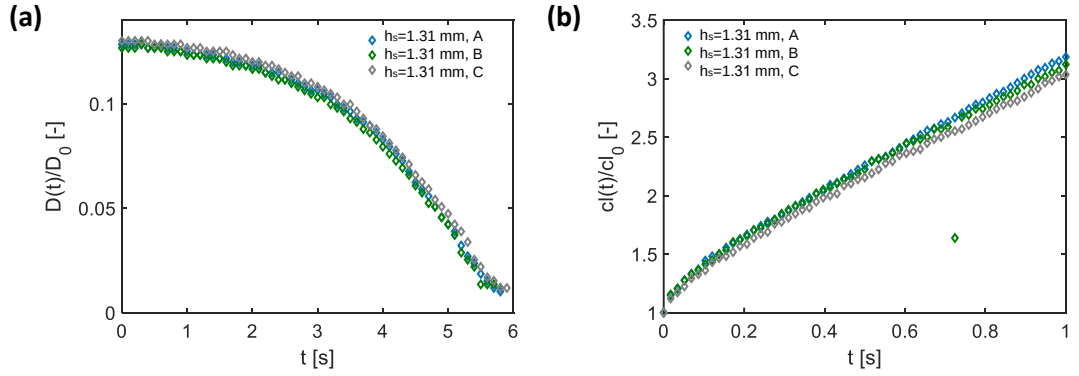

Figure 4.20: Reproducibility check of the minimum diameter evolution for PDMS 60 at $h_s = 1.31$ mm.

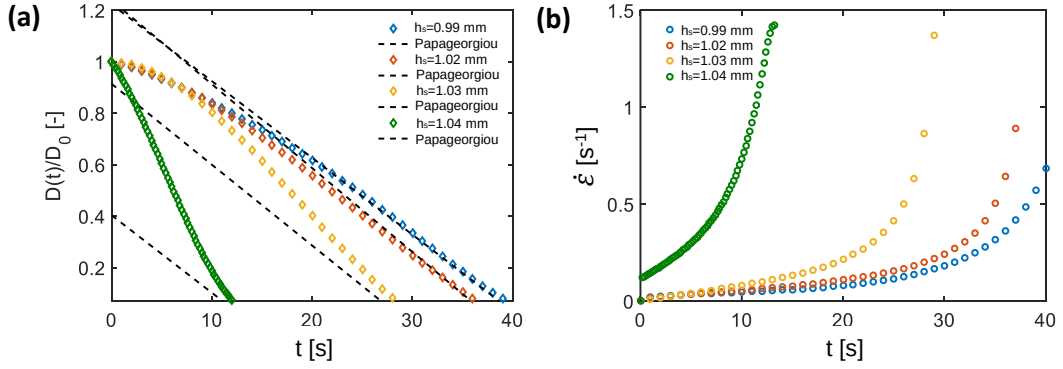

Figure 4.21: (a) Influence of the substrate height on the filament thinning for PDMS 1000 (open symbols) and visco-capillary prediction (dashed lines). (b) Extension rate during the process.

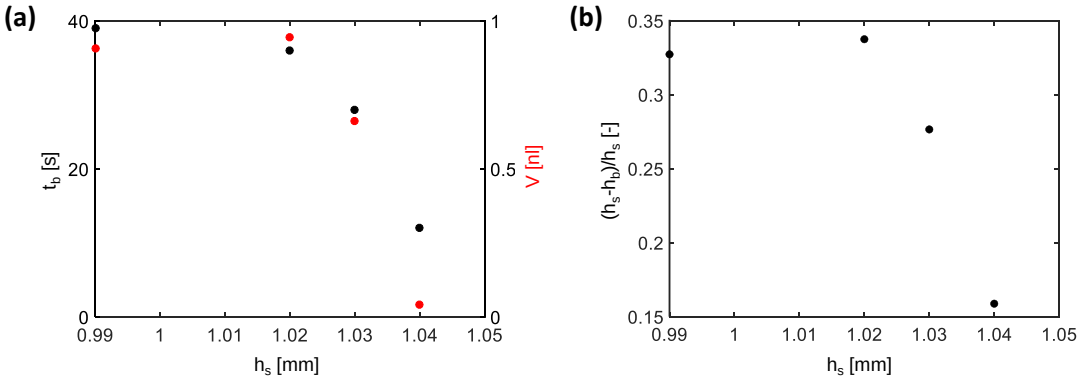

Figure 4.22: (a) Time to breakup and deposited volume as function of substrate height. (b) Relative breakup height as function of substrate height. Data for PDMS 1000.

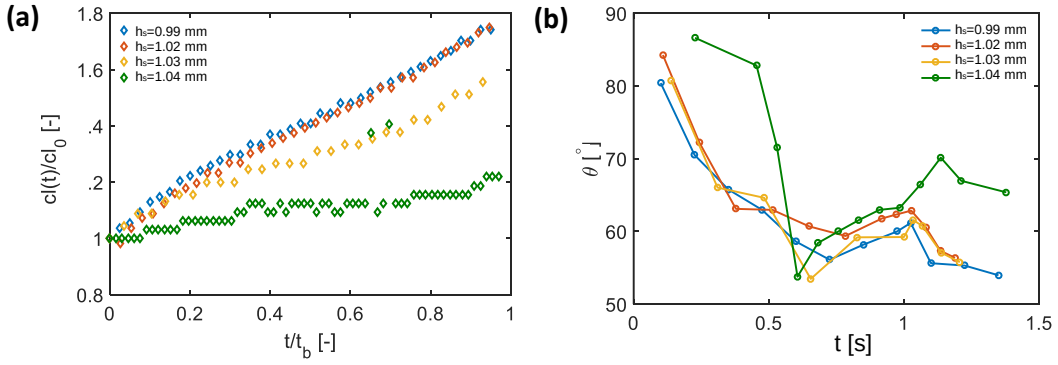

Figure 4.23: Evolution of the (a) normalized contact line as function of the time normalized with the time to breakup, and (b) dynamic contact angle for PDMS 1000.

CHAPTER 5

Effect of substrate - fluid interaction on the thinning of a viscous filament

Abstract

The effect of the fluid - substrate interactions on the jetting of high viscous silicone fluids have been studied. In particular, the effects of the static contact angle and of surface irregularities have been investigated using an oil repellent (oleophobic) substrate and two coated sandpapers with different surface roughness. The jetting experiments have been performed with a commercial micro-dispensing system capable of handling high viscosity fluids and an optical system for imaging the process. An analysis of the thinning and spreading has been performed, after image processing, and the results are compared with the case of jetting on a smooth surface for which the fluid exhibits full wetting. The influence of the substrate to nozzle distance has also been included. When oleophobic surfaces are used the resolution of the process increases while the time for breakup remains the same, and this effect is independent of the substrate height. When surface roughness is introduced, the resolution and breakup time scale are dependent on the substrate height, since this determines the relative roughness size to the area of the fluid in contact with the substrate. The substrate height causes different fluid - substrate interactions that influence the balance between the forces developed in the filament and the capillary forces that drive the spreading. This work provides important information for industrial processes that involve the deposition of a small amount of material on different materials as in the field of multi-material applications.

5.1 Introduction

To fully understand and describe the deposition mechanism of a fluid it is extremely important to investigate the equipment utilized, the fluid properties (density, viscosity,

Largely reproduced from:
Pepe, J., Cardinaels, R., Peters, G.W. and Anderson, P.D. A study on the jetting and spreading process of highly viscous fluids. *In preparation.*

surface tension, rheology), but equally important the substrate nature and the interaction that the last has with the deposited material. The success of jetting a fluid is determined by the fluid physical and rheological properties together with the capability of the dispensing device to handle it. The subsequent formation of an in flight droplet, a droplet with a long tail or simply a filament is dictated by the delicate balance between fluid properties and surface tension. On the other hand the contact and spreading of the fluid on the substrate is controlled by the interaction between them, which is the result of the fluids physical and rheological properties and substrate nature (wettability and topography among others [159]).

Surfaces are usually classified according to their surface energy and thus the interaction with the material they are in contact with. When a fluid is in contact with a surface, based on the respective surface tension values, it could completely wet the surface or dewet it, or have intermediate behavior. To describe wetting and dewetting, respectively, for a liquid with a surface tension very similar to that of water, the terms hydrophilic and hydrophobic are used. In case of a liquid with surface tension similar to that of oil the terms oleophilic and oleophobic are used to describe the aforementioned phenomena [188, 189]. The affinity between a fluid and a substrate also depends on the surface topography of the last: an example is the lotus flower that thanks to the microstructures present on its surface repels water. In contact with the flower the latter forms a perfect sphere. This phenomenon generates a self-cleaning effect: the water rolling on the flower will collect any dirt and possible bacteria [190, 191, 192]. Studying the contact angle and spreading is highly relevant since surfaces are never smooth in real life and this helps in controlling the engineering processes to create functional substrates. The knowledge and the inspiration comes very often from nature that evolves to adapt to the environmental changes and shows surfaces with different microstructures and wettability [193, 194, 195, 196]. Oleophobic and superoleophobic substrates are very difficult to be found in nature since almost no surface has a lower surface energy than oil. Despite this scientists have been able to develop superoleophobic substrates utilizing both chemical treatments and the introduction of structured irregularities, thereby studying the effects of their presence and their size and shape on the wettability [189, 190, 197, 197, 198, 199].

The classic theories of the contact angle on a rough substrate are known to be the Wenzel [200] and the Cassie-Baxter [201] theories. In the case of the Wenzel state the fluid fills the cavities between the roughness while in the Cassie-Baxter state the fluid remains on top of the roughness. The presence of roughness on the substrate is known to amplify the wetting or dewetting. This is only valid when the size of the surface asperities is considerably lower than the droplet size of the fluid [202]. When the size of the roughness approaches the same scale as the fluid droplet other effects, like liquid filling, become predominant contributing to the change of the measured contact angle [203].

Most of the studies devoted to understanding the spreading of a fluid on surfaces with different wettability and with structured or irregular surface asperities have been conducted utilizing, mostly, sessile or impacting droplets. The aim of this work is to investigate the effect of surface roughness and the static contact angle during jetting of viscous fluids, where the spreading and thinning phenomena are coupled. This is to our knowledge the first time that this type of study is performed and we believe it will help

understanding the high viscous jetting process further and open up the possibilities for new applications.

5.2 Materials and methods

5.2.1 Materials and material characterization

Silicone fluid AK 60 000 (PDMS 60) from Wacker Chemie AG, was chosen as a representative material to study the effect of the substrate properties on high viscosity jetting. The fluid has a molecular weight (M_w) of 120 000 kg/mol, density (ρ) of 970 kg/m^3 and surface tension (σ) of 0.0215 N/m. The substrates used in this study are a mirror polished stainless steel metal, an oil repellent surface and two commercial sandpapers, FEPA P4000 and CAMI 120. According to the standards both sandpapers are coated with abrasive particles. The particle sizes and roughness specifications are given in Table 5.1. Roughness height (R_h) has been estimated using the simple model proposed by Pinson and Wang [204]. They assumed the sandpaper particles to be hemispherical and the height to be half the particle size.

Table 5.1: Sandpaper characterization.

Sandpaper type	Average particle size [μm]	Roughness (R_h) [μm]
CAMI 120	106	53
FEPA P4000	2.5	1.25

The metal and oil repellent substrate are both smooth and differ in their affinity with silicone oil. The static contact angle (θ_s) has been measured using the sessile droplet technique by means of the Drop Analysis-LB-ADSA IamgeJ plugin. The static contact angle for the metal surface is $\approx 0°$ while for the oleophobic substrate it is $\approx 60°$ (see Figure 5.1). For the sandpaper substrate it was not possible to calculate the static contact angle since the fluid is percolating in time through the substrate roughness.



Figure 5.1: Static contact angle measurement.

The rheological properties of the silicone fluid were measured using an Anton Paar rheometer (MCR 501) in combination with a 25 mm sanded plate/plate geometry

at a temperature of 25°C, with a fixed strain of 10% and frequencies between 0.03 rad/s and 628 rad/s. A multi-mode Maxwell model was used to obtain the linear viscoelastic relaxation spectrum from the experimental storage and loss moduli and the Cox-Merz rule was applied to extract the zero shear viscosity (η_0) [62]. The results of the measurements are reported in Table 5.2. For more details on the experimental and calculation methods the reader can refer to Chapter 4 of the thesis.

Table 5.2: Silicone fluids properties.

Material	M_w [kg/mol]	PDI [-]	η_0 [Pa·s]	n [-]	τ_{av} [s]
PDMS 60	120 000	5.2	58.2	0.87	0.005

5.2.2 Experimental setup and experimental protocol

Jetting experiments were performed using an *in-house* developed setup (Figure 5.2). The setup consists of a microdispensing valve (MDV 3250+ VERMES Microdispensing GmbH, externally controlled by an electronic controller MDC3200+). High speed imaging (100 fps) and back lightening system allow to follow the evolution of the jet. The fluid is ejected through a 100 μm nozzle using a mechanically driven piston. A piezo element is responsible for the fast and precise trapezoidal movement of the piston. The substrates are mounted on a manual x-y-z stage for precise definition of the position of the substrate with respect to the nozzle. The temperature of the system is set to 25°. Considering the high viscosity of the fluids studied, the needle lift is set to 100%, and fixed pulse parameters were used: rising time (RI) 0.3 s, opening time (OT) 0.015 s, and falling time (FA) 0.3 s. A detailed description of the dispensing setup can be found in Chapter 4 of this dissertation.

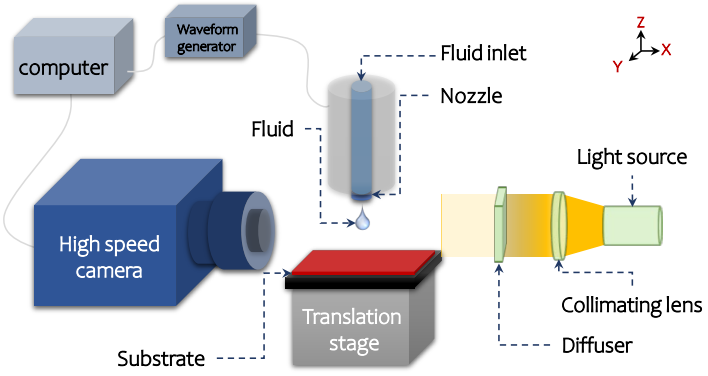

Figure 5.2: Schematic drawing of the dispensing setup and high-speed imaging system.

In this study experiments were performed at two substrate heights for each substrate type in order to check the effect of wettability and surface roughness in region I and II defined in Chapter 4.

5.2.3 Data analysis

The video data were converted to image sequences using ImageJ software. The image sequence obtained was used to extract quantitative information about the thinning and spreading behavior (see Figure 5.3). The deposited fluid volume (V), substrate height (h_s), breakup height (h_b), static and dynamic contact angle (θ_s and θ, respectively) are measured using ImageJ software. The evolution of the midfilament diameter (D) and the evolution of the contact line (cl) of the fluid with the substrate are evaluated after post processing using MATLAB® built-in Canny edge detection method. In case of experiments with sandpaper the spreading behavior is completely analyzed using ImageJ because of the failure of the edge detection method in the presence of surfaces asperities.

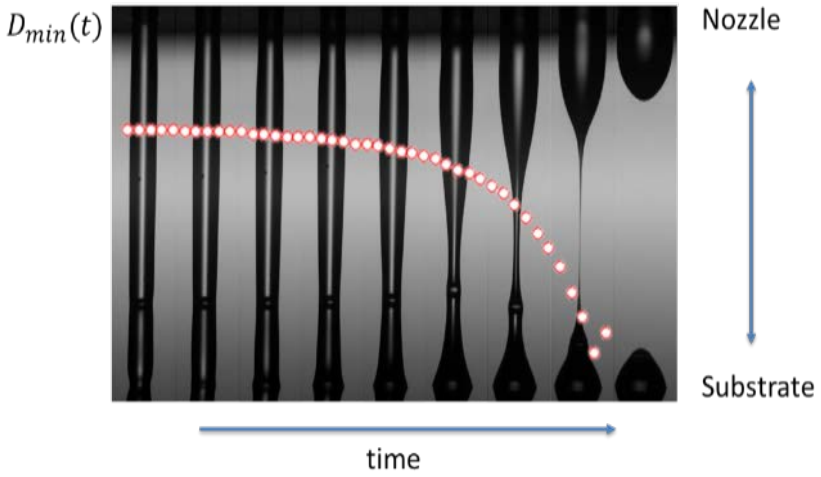

Figure 5.3: Representative example of the image analysis process. Image sequences and evolution of the midfilament diameter extracted from the images.

5.3 Results and discussion

5.3.1 Influence of static contact angle

Silicone fluid is one of the materials with the lowest surface tension. Surfaces that resist wetting of this type of fluids are called superoleophobic. In nature there is no material that has a surface tension much lower than silicone thus superoleophobic surfaces have to be engineered combining chemical composition, re-entrance surface curvature and surface roughness [190, 191]. The creation of superoleophobic surfaces is out of the scope of this study, therefore only commercially available substrates were chosen as a case study.

5.3.1.1 Thinning behavior

To investigate the influence of the wetting properties on the filament thinning and breakup, jetting experiments were performed using substrates on which PDMS has quite

a substantial difference in static contact angle ($\Delta\theta_s \approx 60°$). Figure 5.4 shows image sequences of the thinning mechanism of PDMS 60 on a metal and on a oleophobic substrate. Two substrate heights were investigated: h_s = 1.52 mm and h_s =1.63 mm, corresponding, respectively to region I and II previously individuated (see Chapter 4). The main goal is to understand if the influence of the static contact angle depends on the distance between substrate and nozzle. From the image sequence it is evident that at h_s = 1.52 mm the volume dispensed on oleophobic substrate is much smaller to the one on metal and the breakup point shifts closer to the substrate despite the fact that the time to breakup is comparable. Table 5.3 summarize the jetting results discussed above.

Table 5.3: Jetting experiments results.

Substrate	h_s [mm]	t_b [s]	V [mm^3]	h_s-h_b/h_s[-]
metal	1.52	4.7	$5.7{\cdot}10^{-3}$	0.44
oleophobic	1.52	4.5	$7.1{\cdot}10^{-4}$	0.29
metal	1.63	1.6	$1.8{\cdot}10^{-4}$	0.18
oleophobic	1.63	1.5	$1.3{\cdot}10^{-4}$	0.19

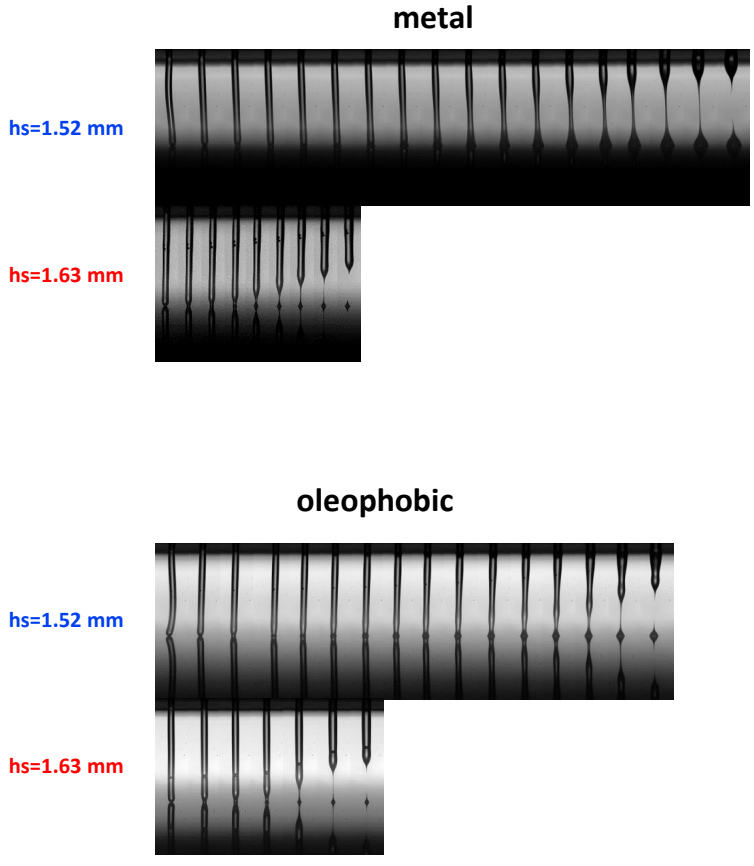

Figure 5.4: Image sequence of the thinning process on a metal and on an oleophobic surface for different substrate heights.

For a more detailed analysis we extracted the minimum filament diameter evolution over time and computed the extensional deformation rate as: $\dot{\epsilon}$ = -2/D(t) dD(t)/dt, where $D(t)$ is the filament diameter and t the experimental time. From Figure 5.5 it is possible to observe that the breakup time and extensional rate developed during the process are not affected by the static contact angle at $h_s = 1.63$ mm. At lower h_s the breakup time is slightly shorter and the deformation rate increases for the oleophobic surface as compared to the metal surface. The different affinity with the substrate has a higher effect at lower substrate height (h_s = 1.52 mm), where the contact area with the substrate is bigger and more competition arises between spreading and elastic stresses developed during thinning.

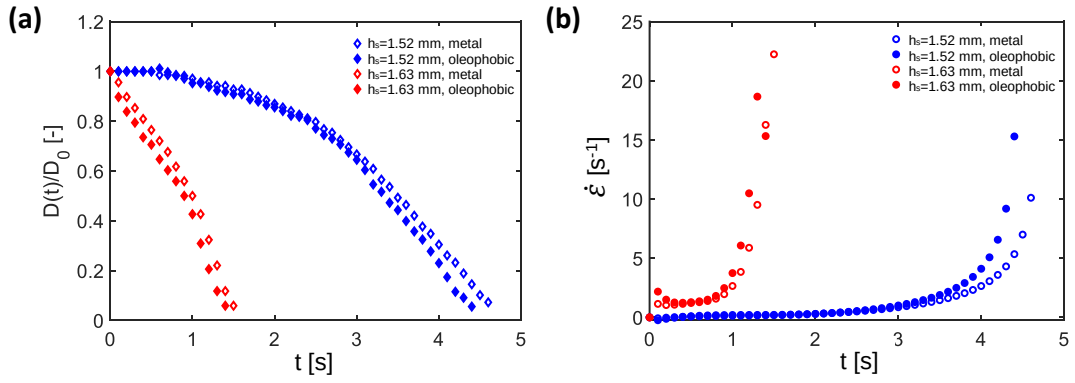

Figure 5.5: (a) Evolution of the diameter and (b) extension rate during the thinning process.

In the previous study (see Chapter 4) we have performed a dimensional analysis to properly characterize the thinning behavior and determine the thinning mechanisms. For the type of fluid studied and the type of experimental boundary conditions the thinning experimental results were not well predicted using the dimensional analysis, therefore, it was not possible to treat the problem with the known thinning theories. Because of the change of the static contact angle we want to verify that the thinning mechanism does not change, therefore we performed the same dimensional analysis in order to define whether it is valid when using less wettable surfaces. The relevant dimensionless numbers are [149, 150, 183, 184]: the Ohnesorge number, $Oh = \eta_0/(\rho\sigma R)^{1/2}$, defines the ratio of inertial forces over viscous forces, the intrinsic Deborah number, $De_0 = \tau/(\rho R^3/\sigma)^{1/2}$, represents the ratio of the polymer relaxation time to the time scale of the flow and thus the competition between elastic and inertial forces, and the elasto-capillary number, $Ec = \tau\sigma/\eta_0 R$, defines the balance between elastic and viscous forces. In the mentioned dimensionless groups η_0 is the zero shear viscosity, ρ the density, σ the surface tension of the fluid, τ the Rouse time and R the instantaneous radius of the filament. Using R as characteristic length it is possible to estimate local values of the dimensionless numbers and the time at which a transition from one regime to the other occurs [184]. From the dimensional analysis $Oh \gg 1$, $De \ll$ and $Ec \ll 1$, thus viscosity is the predominant resisting force and the thinning should follow the visco-capillary regime according to the Papageorgiou equation [149]:

$$\frac{D(t)}{D_0} = 0.0709 \left(\frac{\sigma}{\rho D_0} \right) (t_b - t)\,, \tag{5.1}$$

In the above equation D_0 is the initial filament radius and t_b the filament breakup time. The numeric prefactor can be written as $a = (2X(t)\text{-}1)/6$ where the value of $X(t)$ in the Papageorgiou solution is constant and equal to 0.7127 (see Chapter 4 for more information). The visco-capillary prediction cannot properly predict the thinning for h_s = 1.52 mm and h_s = 1.63 mm as shown in Figure 5.6 (a) and, in particular, in Figure 5.6 (b) where the experimental value of $X(t)$ is compared with the constant value from the Papageorgiou solution. The results are in agreement with the previous study on PDMS 60 on different metal substrate heights reported in Chapter 4.

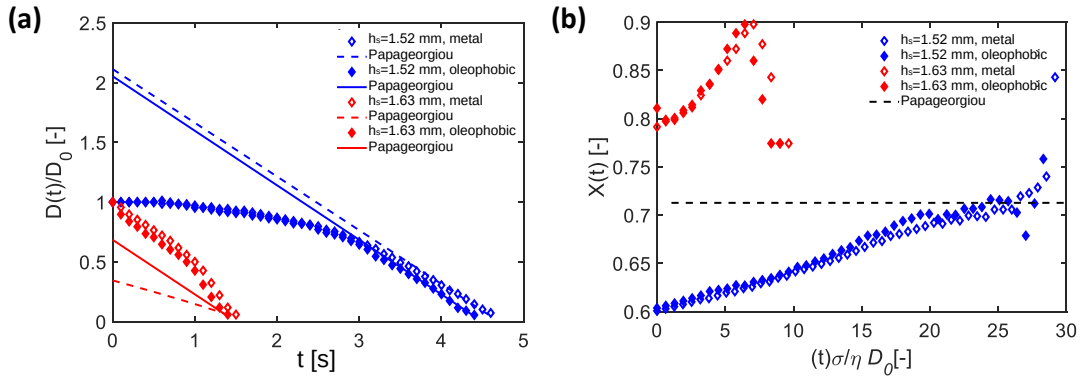

Figure 5.6: (a) Diameter evolution compared with the Papageorgiou prediction ($X(t) = F_z(t)/2\pi\sigma R(t)$). (b) Comparison between the evolution of the experimental value of $X(t)$ and the Papageorgiou solution.

In order to underline the effect of wettability on the thinning mechanism we plotted the dimensionless filament diameter against the time normalized with the time to breakup. Independently from the wettability the substrate height determines the thinning behavior as is clearly observable in Figure 5.7.

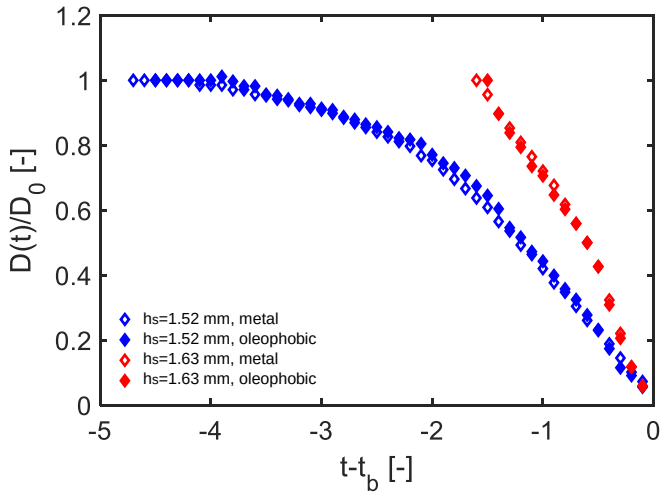

Figure 5.7: Evolution of the normalized diameter as function of the normalized time with the time to breakup.

5.3.2 Spreading behavior

As shown in Chapter 4 it is extremely important to characterize the spreading to fully understand the process. The spreading behavior is analyzed investigating the evolution of the contact line of the fluid on the substrate and the evolution of the dynamic contact angle. Figure 5.8 shows the evolution of the contact line.

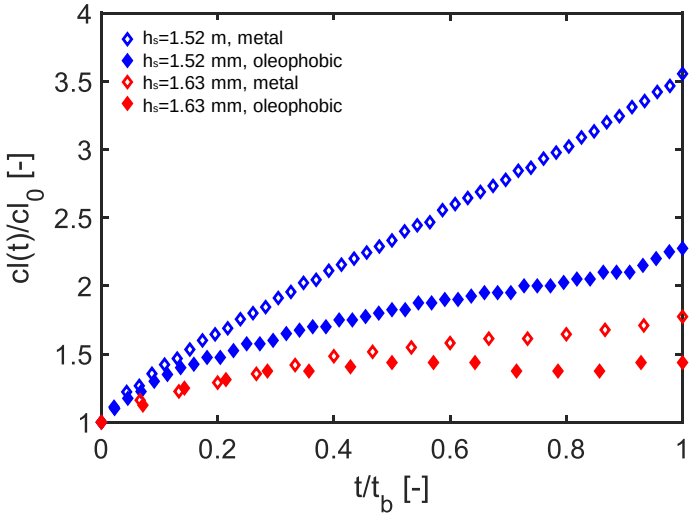

Figure 5.8: Evolution of the dimensionless contact line.

The above figure shows the effect of the initial contact area on the spreading velocity as well as the fact that a higher static contact angle translates in a lower spreading velocity

independently of the substrate height. Despite the slower spreading the evolution of the dynamic contact angle is not influenced by the wettability as shown in Figure 5.9. It is possible to individuate the same phases defined in Chapter 4 for both metal and oleophobic substrates at the same distance from the nozzle. Despite this the results in part contradict the study from Šikalo et al. [186] were no effect of the static contact angle was found on the spreading and dynamic contact angle evolution in the case of a glycerin droplet on a smooth glass and wax substrate in spreading conditions when inertial and viscous forces dominates.

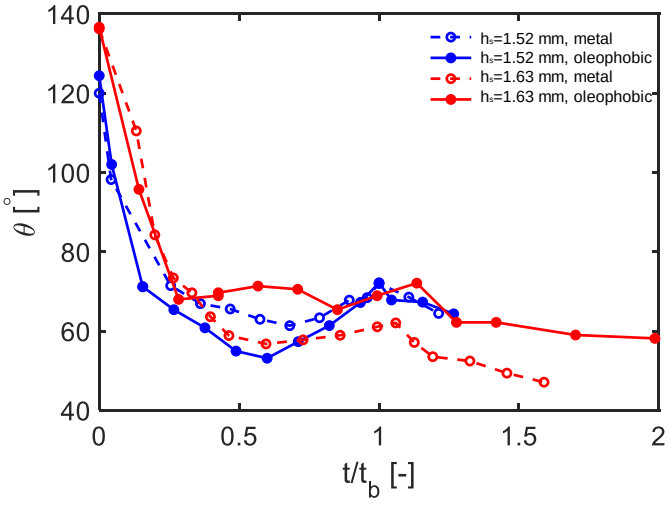

Figure 5.9: Evolution of the dynamic contact angle.

The contradiction and the different effect that the static contact angle has on the spreading could be related to the interplay with thinning. In order to understand if a relation between the two processes exists the evolution of the ratio r has been calculated. This ratio represents the balance between the axial forces and the capillary forces acting against the thinning and in favor of spreading on the substrate, respectively. This ratio was introduced in Chapter 4 for the first time and is calculated according to Eqn. 4.13. Figure 5.10 shows that when the intrinsic interaction between the fluid and the substrate changes, a different balance between the forces developed in the filament and the spreading is created. This is particularly visible for PDMS60 on an oleophobic substrate at $h_s = 1.52$ mm where the spreading is much slower and, thus, the contribution of the stresses in the filament is higher. When moving further from the nozzle the process becomes less sensitive to the wettability of the substrate because of the lower contact area of the fluid on the substrate itself.

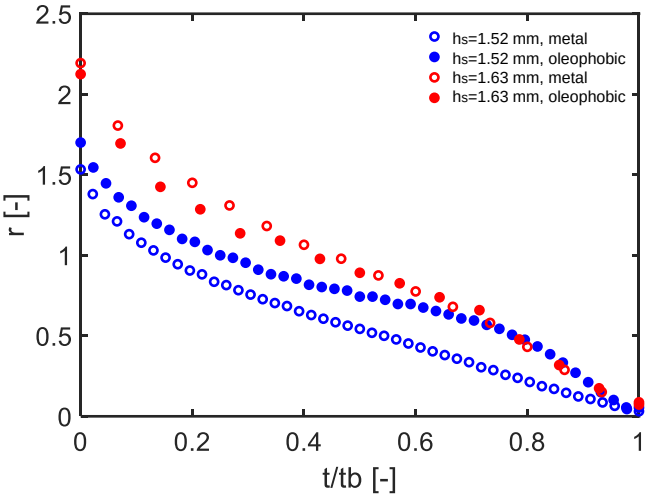

Figure 5.10: Evolution of r as function of the normalized time for PDMS60 on metal and oleophobic substrate at two h_s.

5.3.3 Influence of roughness

5.3.3.1 Thinning behavior

In order to understand the influence of roughness in this type of process, we performed jetting experiments on two sandpapers with different abrasive average particle sizes, at two substrate heights. In this case, as well, the distances from the nozzle were chosen in order to investigate the behavior in region I and II described in Chapter 4. The image sequences in Figure 5.11 show that the substrate height has the same effect when using rough surfaces namely increasing the time to breakup and the dispensed volume when moving the substrate closer to the nozzle and speeding up the process and increasing the resolution when further way from the nozzle.

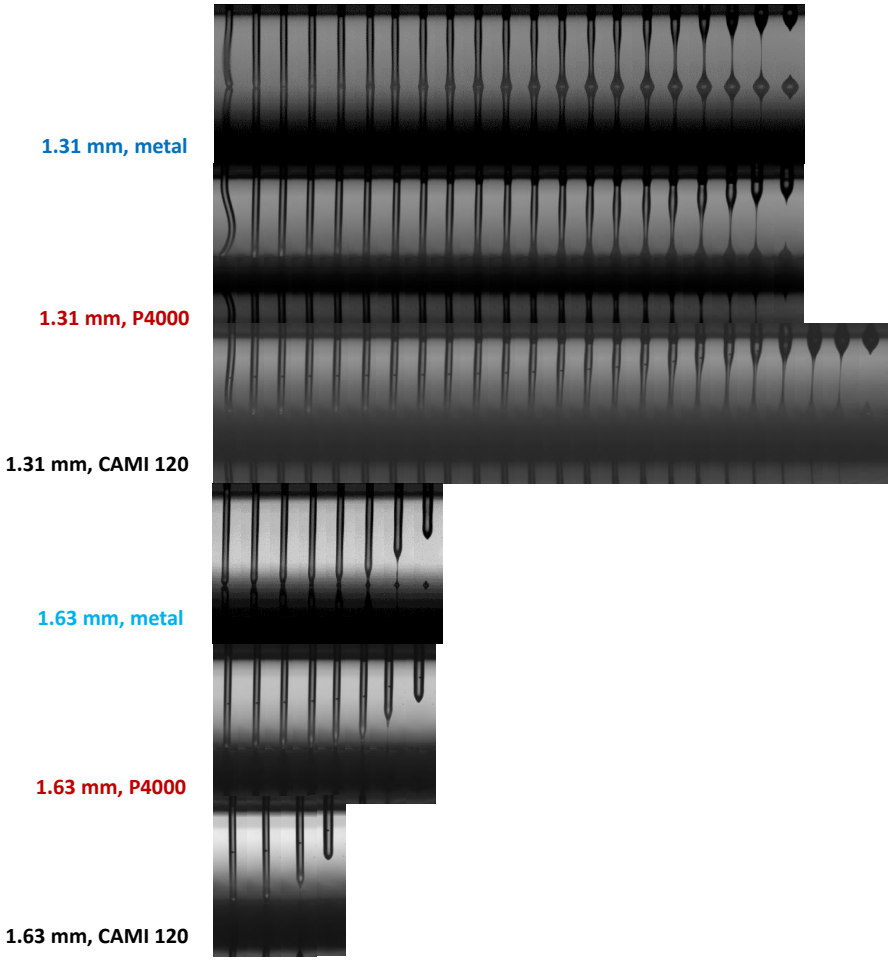

Figure 5.11: Image sequence of the thinning process of PDMS 60 on metal and sandpapers at different substrate heights.

In order to highlight the effect of substrate asperities the results are compared with the ones performed on a smooth metal surface. When analyzing the evolution of the diameter (Figure 5.12 (a)) over time it is possible to observe that the effect of the roughness has a "reversed" behavior: at low substrate heights the thinning and breakup is slower on a rougher substrate (CAMI 120) while at higher substrate height it is faster. The extensional rates developed during the self-thinning process are in agreement with the time to breakup dependence on the substrate roughness, as can be observed in Figure 5.12 (b). Despite this, the extensional rates in region I are much larger than the ones obtained when PDMS 60 is jetted on a metal substrate. This result seems to be in contrast with the time to breakup suggesting that some extra contributions are determining the filament thinning.

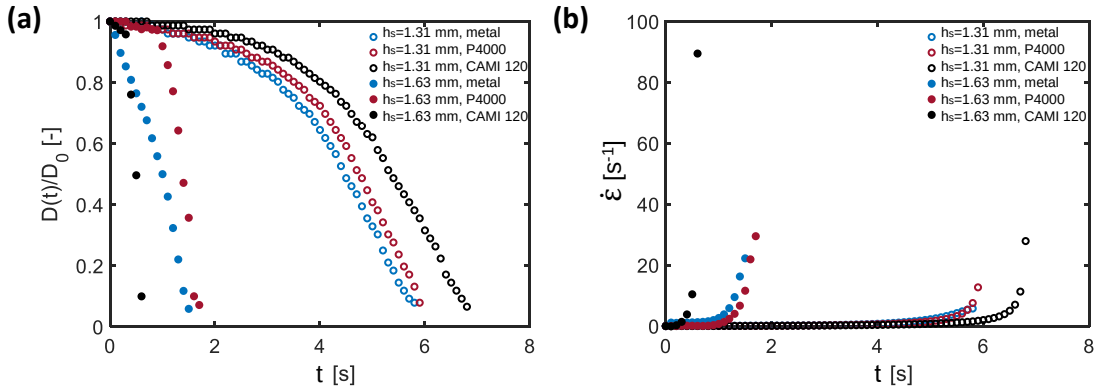

Figure 5.12: (a) Evolution of the diameter and (b) extension rate during the thinning process.

The jetting results on sandpaper are summarized in Table 5.4. Interesting to notice is that the volume deposited at $h_s = 1.31$ mm is lower in the case of CAMI 120 despite the fact that the time to breakup and relative position of the breakup would suggest the opposite. The increase in resolution together with the "reversed" roughness effect mentioned above can be explained with the tendency of the fluid to percolate through the abrasive sandpaper particles. When the roughness height is bigger, (i.e. bigger particle size), and the initial contact area of the material is larger, (i.e. lower substrate height), the fluid tends to fill the cavities of the roughness and the effect is bigger when the substrate asperities size is comparable with the initial droplet size. In opposition to this, when moving further the substrate further from the nozzle the initial droplet size is much smaller than the roughness and a bulk penetration occurs [203, 205]. This phenomenon becomes more evident with decreasing droplet size. This is confirmed by a lower deposited volume than on the smooth metal surface.

Table 5.4: Jetting experiments results on sandpaper.

Substrate	h_s [mm]	t_b [s]	V [mm^3]	h_s-h_b/h_s[-]
P 4000	1.31	5.9	$3.8{\cdot}10^{-3}$	0.39
CAMI 120	1.31	6.8	$2.3{\cdot}10^{-3}$	0.45
P 4000	1.63	1.8	$6.2{\cdot}10^{-5}$	0.17
CAMI 120	1.63	0.7	$4.3{\cdot}10^{-6}$	0.12

Utilizing the dimensional analysis described in Section 5.3.1.1 we found that the thinning is dominated by the visco-capillary regime. Thereafter we compared the Papageorgiou prediction to the experimental diameter evolution. Figure 5.13 (a) and Figure 5.13 (b) show that the prediction, once again is not able to describe the filament thinning, in agreement with the results obtained when utilizing flat metal and oleophobic surfaces.

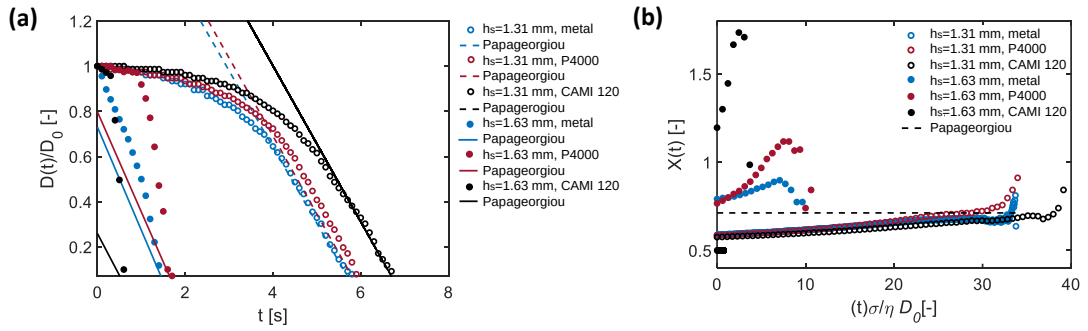

Figure 5.13: (a) Papageorgiou prediction of the diameter evolution. (b) Comparison between the evolution of the experimental value of *X(t)* and the Papageorgiou solution.

The above results can be summarized in Figure 5.14 that highlights the fact that the substrate roughness plays a role in determining the thinning behavior. At $h_s = 1.52$ mm the diameter evolution is determined only by the substrate height independently of the substrate nature, while at $h_s = 1.63$ mm the wettability definitely influences the thinning.

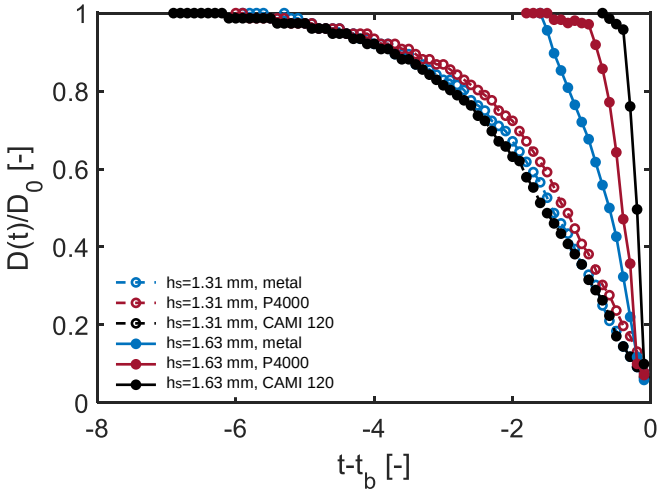

Figure 5.14: Evolution of the normalized diameter as function of the normalized time with the time to breakup.

5.3.3.2 Spreading behavior

The effects of the substrate roughness become much more evident when analyzing the spreading behavior of PDMS 60. In the case of sandpaper substrate the spreading velocity in region I decreases with increasing roughness (see Figure 5.14 (b)). This result confirms the hypothesis postulated in Section 5.3.3.1. At lower substrate height the increase of roughness and contact area determine a higher flow within the cavities thereby reducing

the spreading velocity since part of the fluid is now pulled into the substrate cavities. Contrarily in region II the liquid penetration determines a fast disappearing of the fluid in the substrate bulk. As already shown in previous studies [203] this phenomenon causes an extreme decrease of the spreading till reaching pinning or even a receding of the contact line. Our results are quite well in agreement as shown in Figure 5.15 where the contact line stays approximately constant or slightly reduces over time for both sandpapers.

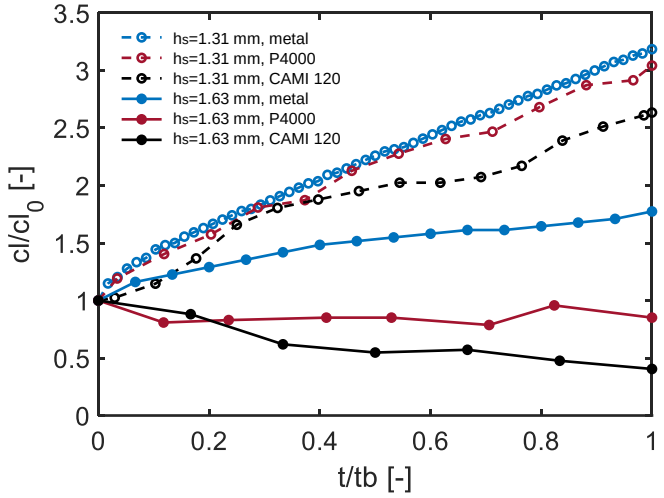

Figure 5.15: (a) Evolution of the dimensionless contact line. (b) Evolution of the dimensionless spreading velocity.

Despite the quite different spreading behavior the evolution of the dynamic contact angle follows the same trend for different substrate heights as in the case of smooth surfaces, as can be observed in Figure 5.16. Regardless of the fact that the trends are the same with the presence of the same phases for the same value of h_s the value of the dynamic contact angles for rough surfaces are always higher.

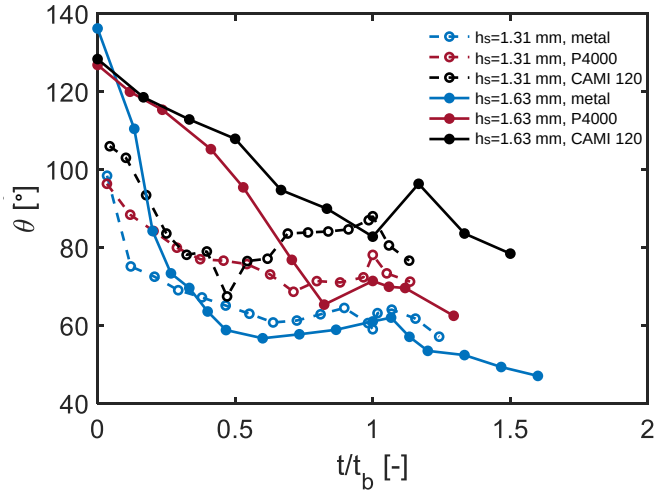

Figure 5.16: Evolution dynamic contact angle

The investigation of the spreading helps in explaining the results observed in Section5.3.1.1. Because of the higher contact area, at lower substrate height, filling of the surface cavities occurs inducing absorption of the liquid, thereby slowing the spreading and increasing the lifetime of the filament. At higher substrate heights the roughness becomes of the same order as the droplet size and liquid infiltration takes place causing a pinning or even receding of the contact line and the continuous pulling of liquid in the substrate adds an extra drainage of the fluid filament that translates in a faster thinning. This effect is much more predominant for the rougher substrate (CAMI 120), as can be seen from the results shown above. When calculating the ratio r, the balance between axial forces in the filament and the capillary forces in the droplet, changes when using rough surfaces. At $h_s = 1.31$ mm the contribution of the axial stresses in the filament increases due to less spreading and absorption of fluid in the asperity cavities, an effect that become more predominant at higher R_h. When shifting to $h_s = 1.31$ mm the temporal evolution of r completely changes from smooth to rough substrates. In this case r first slightly increases and then decreases towards the breakup time. This phenomenon can be explained considering that the axial stresses are predominant until the fluid fills the substrate cavities while afterwards the penetration of fluid in the bulk of the substrate takes over in the process.

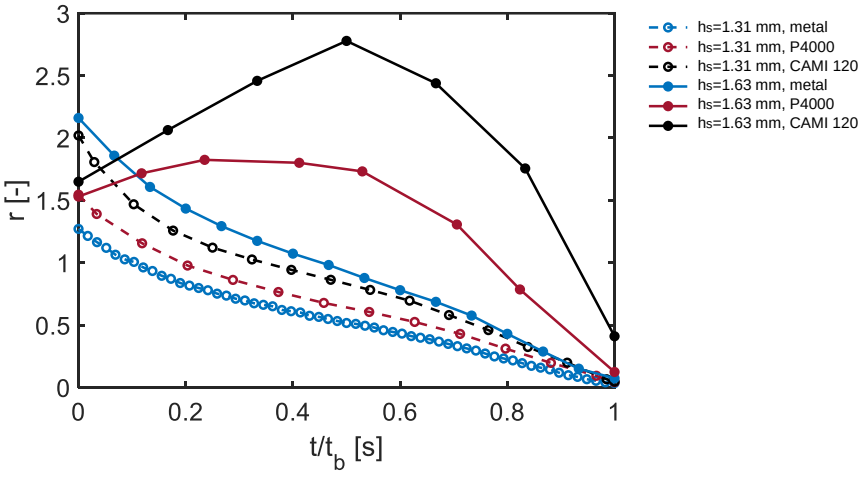

Figure 5.17: Evolution of the ratio r as function of the time normalized to the time to breakup.

5.4 Conclusions

In this study we have investigated the effect of static contact angle and surface topography on the thinning phenomenon during jetting of a high viscous silicone fluid. The effect of fluid-substrate interaction was coupled with the effect of substrate height. The results show that when changing the static contact angle the thinning behavior remains unaltered while the spreading is slowed down with no significant change in the evolution of the dynamic contact angle. When the topography of the substrate is changed with the introduction of roughness the thinning-spreading coupled phenomenon becomes more complicated due to the presence of other phenomena such as cavity filling and bulk penetration that characterize the spreading behavior. In our study the presence of surface roughness slows down the thinning process for a low substrate height while it speeds up the thinning process for a high substrate height. The deposited volumes are always smaller compared to those obtained on smooth surfaces. While for the thinning phenomenon there is a "reversed effect", depending on the distant between nozzle and substrate, in case of spreading surface roughness always slows the process down. The latter effect is due to cavities filling and liquid penetration occurring at low and high substrate heights, respectively. The evolution of the dynamic contact angle follows the same trend as for smooth surfaces at the same substrate distance but with much higher local values. A relation between axial forces in the filament and capillary forces in the fluid in contact with the substrate is found for both cases studied in this Chapter. This study shows the high complexity of the process especially when nonideal and non-smooth surfaces are being used. The results of the current work require a more detailed and systematic study to fully characterize the effect of different substrates.

CHAPTER 6

Conclusions and Recommendations

6.1 Conclusions

The first aim of this work is to provide new experimental tools to further understand the behavior of polymers when subjected to an extensional flow. Despite the fact that this type of flow is very common during processing, there is a lack of experimental setups that allow a fundamental study of the effect of this type of flow on the rheology, and, consequently, processing behavior of polymers as well as their crystallization.

As second aim, these new setups will be used for the investigation of extensional flow induced crystallization ans the interaction between thinning and spreading of highly viscous liquids.

The research performed in this dissertation has led to the following conclusions:

Chapter 2: A filament stretching rheometer for *in-situ* X-ray experiments: combining rheology and *in-situ* crystalline morphology characterization

- A filament stretching rheometer has been designed and developed with the unique capability of allowing *in-situ* measurements while applying a well controlled uniaxial extensional deformation.
- Validation experiments have been performed on a commercial LDPE. The melt rheology is very well in line with the results obtained using consolidated extensional rheometers, while *in-situ* X-ray experiments prove the capability of the instruments to capture the formation and evolution of crystal morphologies during and after uniaxial extensional flow.
- This setup will contribute to improve the knowledge of extensional rheology and in particular of extensional flow induced crystallization. The unique capabilities of associating rheology with *in-line* time-resolved structure characterizations defines the flexibility of the machine and opens up new research opportunities.

Chapter 3: Unraveling the extensional flow induced crystallization of LDPE via *in-situ* characterization

- A systematic study of the extensional flow induced crystallization of LDPE has been performed. The overall extensional rheology is not affected by the crystallization during flow. The amount of material that crystallizes during flow is too little

to contribute to an observable change in the material stress therefore, possibly explaining the unperturbed strain hardening behavior.

- At the chosen flow conditions both strain and strain rate influence the crystallization process: crystallization rates and amount of orientation increase when increasing strain and/or strain rate. Despite the fact that this effect is present for both flow parameters the effect of strain is predominant.
- From the analysis of the 2D-SAXS patterns emerges a peculiar mechanism in the formation of kebabs. There is an initial phase during which not well oriented structures with long correlation length form in the direction of the flow. This phase lasts until a critical time that signs the start of the formation of kebab. The initial phase as well as the critical time are influenced by the flow conditions.
- It is possible to follow the kebab growth using the model introduced by the group of Hsiao and coworkers [11, 99]. This model is not applicable to all flow conditions investigated in this work since not always clear shish-kebab structures are formed. Following the temporal evolution of the kebab diameter, calculated by the model, an initial constant growth rate is identified for all flow conditions. This growth rate is strongly influenced by the flow conditions and decreases over time before the diameter reaches a plateau.
- 1D-WAXD experiments reveal the presence af mixed Type I-II crystal structures at the highest strain rate but no further information could be extracted due to the limited available angle.

Chapter 4: A study on the jetting process of highly viscous fluids: from droplet-on-demand (DOD) to volume-on-demand (VOD)

- A setup that combines a commercial microdispensing valve, able to handle high viscous fluids, and an optical system to image the jetting process, and thus follow the filament breakup and spreading of the deposited droplet on the substrate.
- The jetting behavior of highly viscous PDMS has been investigated with particular interest on the effect of substrate to nozzle distance and molecular weight. The experiments show a transition from DOD to VOD.
- Substrate height has a significant effect on the resolution and time scale of the jetting process when keeping the fluid type fixed. Depending on the substrate height value two regions are identified: region I and region II, closer and further from the nozzle respectively. These two regions are characterized by two different thinning and spreading behaviors. When increasing the substrate to nozzle distance the time to breakup and the deposited volume decrease. On the other hand when keeping the substrate to nozzle distance fixed at the distance an unbounded jetted filament reaches, while increasing viscosity, the time to breakup increases while the deposited volume reduces.
- During the jetting process the stresses developed in the filament compete with the spreading capillary forces. The balance between these competing forces is different in the two regions (region I and region II). This is the result of the two filament geometries developed in region I and II that influence the spreading and the stresses developed in the filament. When viscosity is increased the balance between axial stresses and capillary forces remains unchanged, for experiments

performed in region II, due to extra viscous dissipation in the droplet and lower deformation rate in the filament.

Chapter 5: Effect of substrate - fluid interaction on the thinning of a viscous filament

- The reduction of the interaction between fluid and substrate, by increasing the static contact angle, has an effect on the spreading velocity without substantially altering the jetting behavior or the dynamic contact angle at all substrate heights compared to the reference case with good interaction between the fluid and the substrate.
- Changing the surface topography of the substrate using commercial sandpapers increases the complexity of the process due to additional phenomena that affect the jetting process, such as cavities filling and liquid penetration.
- The evolution of the ratio between axial stresses generated in the filament and capillary forces in the spreading droplet shows that when the spreading is slower, i.e. with a higher static contact angle or introduction of surface roughness, the axial force contribution increases. When the substrate height is in the defined region II, the axial stresses control the process until the bulk penetration of the fluid into the cavities of the substrate occurs.

6.2 Recommendations

The first focus of this work was to provide a new experimental setup for the study of extensional flow induced crystallization. Despite the capabilities of the rheometer some improvements are required in order to expand the potentials of the setup. During the experiments performed in this work it was not possible to follow the stress relaxation of the polymer after cessation of flow. This is important information to better understand the X-ray results and to correlate the microscopic characterization with the macroscopic response of the material obtained from the rheometer. This requires an improvement in the software control of the device. Despite the fact that *ex-situ* characterizations after extensions can provide valuable information to further understand the crystallization mechanism it is currently very difficult to freeze the formed structures, because of the lack of appropriate quenching methods. We believe that a research should be dedicated on this topic in order to design a suitable system that could be associated to the rheometer.

Secondly, the extensional flow induced crystallization experiments unveiled a rich dynamics of the shish kebab microstructure. More strain and strain rates, together with isothermal temperature variations, are required to get a better understanding of the crystallization mechanisms of LDPE under extensional flow such as the kebab and shish formation mechanism. This could help identifying whether there is a critical strain for FIC as shown in literature [102]. In addition, 2D-WAXD patterns should be acquired to gather information on crstallinity and overall crystallization kinetics. Considering that LDPE when oriented can present complex structures like Type I and Type II twisted lamellae it is of vital importance to acquire 2D WAXD images to fully picture

the contribution of all oriented structure and to gain a better understanding of the of the structure. The selection of a smaller beam size would allow to scan the filament to evaluate if there are differences in the crystal structure and morphology along the midfilament diameter.

Third, volume-on-demand printing of highly viscous fluids was demonstrated. In order to gain more understanding on the jetting performance of high viscous fluids and the capabilities of the novel dispensing device for industrial applications a broader investigation of process parameters should be performed. More pulse parameters in combination with more nozzle diameters and geometries should be the subject of future studies. These studies should include fluids with different rheological behaviors in order to gain a better understanding and provide more guidance in the choice of material process parameter combinations. In addition to the deposition of a single droplets jetting of multiple droplets should be conducted. Information about the spreading dynamics is essential for industrial applications. To help this experiment the setup should be improved using an automated stage for the movement of the dispensing valve. To gain a better understanding on the effect of the substrate - fluid interactions, engineered oleophobic and substrates with a well defined roughness should be used. This fundamental knowledge could help in understanding the general phenomena governing the process and become a guide for the actual applications.

Bibliography

[1] H. Andersson, C. Öhgren, D. Johansson, M. Kniola, and M. Stading. Extensional flow, viscoelasticity and baking performance of gluten-free zein-starch doughs supplemented with hydrocolloids. *Food Hydrocolloids*, 25(6):1587–1595, 2011.

[2] M. Prakash, D. Quéré, and J.W.M. Bush. Surface tension transport of prey by feeding shorebirds: the capillary ratchet. *science*, 320(5878):931–934, 2008.

[3] P.M. Reis, S. Jung, J. M Aristoff, and R. Stocker. How cats lap: water uptake by felis catus. *Science*, 330(6008):1231–1234, 2010.

[4] P. Erni, M. Varagnat, C. Clasen, J. Crest, and G.H. McKinley. Microrheometry of sub-nanolitre biopolymer samples: non-newtonian flow phenomena of carnivorous plant mucilage. *Soft Matter*, 7(22):10889–10898, 2011.

[5] S. Kimata, T. Sakurai, Y. Nozue, T. Kasahara, N. Yamaguchi, T. Karino, M. Shibayama, and J.A. Kornfield. Molecular basis of the shish-kebab morphology in polymer crystallization. *Science*, 316(5827):1014–1017, 2007.

[6] I. Dukovski and M. Muthukumar. Langevin dynamics simulations of early stage shish-kebab crystallization of polymers in extensional flow. *The Journal of chemical physics*, 118(14):6648–6655, 2003.

[7] A. Elmoumni, H.H. Winter, A.J. Waddon, and H. Fruitwala. Correlation of material and processing time scales with structure development in isotactic polypropylene crystallization. *Macromolecules*, 36(17):6453–6461, 2003.

[8] R. Dargazany, V.N. Khiêm, E.A. Poshtan, and M. Itskov. Constitutive modeling of strain-induced crystallization in filled rubbers. *Physical Review E*, 89(2):022604, 2014.

[9] J.K. Hobbs, A.D.L. Humphris, and M.J. Miles. In-situ atomic force microscopy of polyethylene crystallization. 1. crystallization from an oriented backbone. *Macromolecules*, 34(16):5508–5519, 2001.

[10] J. Eggers and E. Villermaux. Physics of liquid jets. *Reports on progress in physics*, 71(3):036601, 2008.

[11] R.H. Somani, L. Yang, L. Zhu, and B.S. Hsiao. Flow-induced shish-kebab precursor structures in entangled polymer melts. *Polymer*, 46(20):8587–8623, 2005.

[12] H. Janeschitz-Kriegl. *Crystallization modalities in polymer melt processing*. Springer, 2018.

[13] F. De Santis, R. Pantani, and G. Titomanlio. Effect of shear flow on spherulitic growth and nucleation rates of polypropylene. *Polymer*, 90:102–110, 2016.

[14] H.J.M. Caelers, L.E. Govaert, and G.W.M. Peters. The prediction of mechanical performance of isotactic polypropylene on the basis of processing conditions. *Polymer*, 83:116–128, 2016.

[15] K. Bernland, T. Tervoort, and P. Smith. Phase behavior and optical-and mechanical properties of the binary system isotactic polypropylene and the nucleating/clarifying agent 1, 2, 3-trideoxy-4, 6: 5, 7-bis-o-[(4-propylphenyl) methylene]-nonitol. *Polymer*, 50(11):2460–2464, 2009.

[16] J. Gomes, J.S. Nunes, V. Sencadas, and S. Lanceros-Méndez. Influence of the β-phase content and degree of crystallinity on the piezo-and ferroelectric properties of poly (vinylidene fluoride). *Smart Materials and Structures*, 19(6):065010, 2010.

[17] S. Liedauer, G. Eder, H. Janeschitz-Kriegl, P. Jerschow, W. Geymayer, and E. Ingolic. On the kinetics of shear induced crystallization in polypropylene. *International Polymer Processing*, 8(3):236–244, 1993.

[18] J. Baert, P.V. Puyvelde, and F. Langouche. Flow-induced crystallization of pb-1: From the low shear rate region up to processing rates. *Macromolecules*, 39(26): 9215–9222, 2006.

[19] H. Janeschitz-Kriegl, E. Ratajski, and M. Stadlbauer. Flow as an effective promotor of nucleation in polymer melts: A quantitative evaluation. *Rheologica acta*, 42:355–364, 2003.

[20] A.M. Kumaraswamy, G.and Issaian and J.A. Kornfield. Shear-enhanced crystallization in isotactic polypropylene. 1. correspondence between in situ rheo-optics and ex situ structure determination. *Macromolecules*, 32(22):7537–7547, 1999.

[21] M. Seki, D.W. Thurman, J.P. Oberhauser, and J.A. Kornfield. Shear-mediated crystallization of isotactic polypropylene: The role of long chain- long chain overlap. *Macromolecules*, 35(7):2583–2594, 2002.

[22] J-B. Boitte, C. Vizcaïno, L. Benyahia, J-M. Herry, C. Michon, and M. Hayert. A novel rheo-optical device for studying complex fluids in a double shear plate geometry. *Review of Scientific Instruments*, 84(1), 2013.

[23] N.Y.C. Lin, J.H. McCoy, X. Cheng, B. Leahy, J.N. Israelachvili, and I. Cohen. A multi-axis confocal rheoscope for studying shear flow of structured fluids. *Review of Scientific Instruments*, 85(3), 2014.

[24] R.H. Somani, B.S. Hsiao, A. Nogales, S. Srinivas, A.H. Tsou, I. Sics, F.J. Balta-Calleja, and T.A. Ezquerra. Structure development during shear flow-induced crystallization of i-pp: in-situ small-angle x-ray scattering study. *Macromolecules*, 33(25):9385–9394, 2000.

[25] L. Balzano, S. Rastogi, and G.W.M. Peters. Flow induced crystallization in isotactic polypropylene- 1, 3: 2, 4-bis (3, 4-dimethylbenzylidene) sorbitol blends: implications on morphology of shear and phase separation. *Macromolecules*, 41(2): 399–408, 2008.

[26] L. Balzano, Z. Ma, D. Cavallo, T. B van Erp, L. Fernandez-Ballester, and G.W.M. Peters. Molecular aspects of the formation of shish-kebab in isotactic polypropylene. *Macromolecules*, 49(10):3799–3809, 2016.

[27] J. Chang, Z. Wang, X. Tang, F. Tian, K. Ye, and L. Li. A portable extruder for in situ wide angle x-ray scattering study on multi-dimensional flow field induced crystallization of polymer. *Review of Scientific Instruments*, 89(2), 2018.

[28] E.M. Troisi, H.J.M. Caelers, and G.W.M. Peters. Full characterization of multiphase, multimorphological kinetics in flow-induced crystallization of ipp at elevated pressure. *Macromolecules*, 50(10):3868–3882, 2017.

[29] E.M. Troisi, M. van Drongelen, H.J.M. Caelers, G. Portale, and G.W.M. Peters. Structure evolution during film blowing: An experimental study using in-situ small angle x-ray scattering. *European polymer journal*, 74:190–208, 2016.

[30] P. Hejmady, L.C. Cleven, L.C.A. van Breemen, P.D. Anderson, and R. Cardinaels. A novel experimental setup for in situ optical and x-ray imaging of laser sintering of polymer particles. *Review of Scientific Instruments*, 90(8), 2019.

[31] G. Portale, D. Cavallo, G.C. Alfonso, D. Hermida-Merino, M. van Drongelen, L. Balzano, G.W.M. Peters, J.G.P. Goossens, and W. Bras. Polymer crystallization studies under processing-relevant conditions at the saxs/waxs dubble beamline at the esrf. *Journal of applied crystallography*, 46(6):1681–1689, 2013.

[32] B. Luijsterburg, P. Jobse, D. Hermida Merino, T. Peijs, and H. Goossens. Solid-state drawing of β-nucleated polypropylene: Effect of additives on drawability and mechanical properties. *Journal of Polymer Science Part B: Polymer Physics*, 52 (16):1071–1082, 2014.

[33] G. Portale, D. Hermida-Merino, and W. Bras. Polymer research and synchrotron radiation perspectives. *European Polymer Journal*, 81:415–432, 2016.

[34] A.J. Ryan, D. Bras, W.and Hermida-Merino, and D. Cavallo. The interaction between fundamental and industrial research and experimental developments in the field of polymer crystallization. *Journal of Non-Crystalline Solids*, 451:168–178, 2016.

[35] Y. Liu, W. Zhou, K. Cui, N. Tian, X. Wang, L. Liu, L. Li, and Y. Zhou. Extensional rheometer for in situ x-ray scattering study on flow-induced crystallization of polymer. *Review of Scientific Instruments*, 82(4), 2011.

[36] S. Filipe, B. Knogler, K. Buchmann, and M. Obadal. Shear and extensional flows as drivers for the crystallisation of isotactic polypropylene: When rheology, microscopy and thermal analysis must meet. *Journal of thermal analysis and calorimetry*, 98:667–674, 2009.

[37] M. Chellamuthu, D. Arora, and J.P. Winter, H.H.and Rothstein. Extensional flow-induced crystallization of isotactic poly-1-butene using a filament stretching rheometer. *Journal of Rheology*, 55(4):901–920, 2011.

[38] M. Sentmanat, O. Delgadillo-Velázquez, and S.G. Hatzikiriakos. Crystallization of an ethylene-based butene plastomer: the effect of uniaxial extension. *Rheologica acta*, 49:931–939, 2010.

[39] M. Derakhshandeh and S.G. Hatzikiriakos. Flow-induced crystallization of high-density polyethylene: the effects of shear and uniaxial extension. *Rheologica acta*, 51:315–327, 2012.

[40] C. Hadinata, D. Boos, C. Gabriel, E. Wassner, M. Rüllmann, N. Kao, and M. Laun. Elongation-induced crystallization of a high molecular weight isotactic polybutene-1 melt compared to shear-induced crystallization. *Journal of Rheology*, 51(2):195–215, 2007.

[41] E.E. Bischoff White, H. Henning Winter, and J.P. Rothstein. Extensional-flow-induced crystallization of isotactic polypropylene. *Rheologica acta*, 51(4):303–314, 2012.

[42] P.C. Roozemond and G.W.M. Peters. Flow-enhanced nucleation of poly (1-butene): Model application to short-term and continuous shear and extensional flow. *Journal of Rheology*, 57(6):1633–1653, 2013.

[43] S.L. Wingstrand, M. van Drongelen, K. Mortensen, R.S. Graham, Q. Huang, and O. Hassager. Influence of extensional stress overshoot on crystallization of ldpe. *Macromolecules*, 50(3):1134–1140, 2017.

[44] S.L. Wingstrand, L. Imperiali, R. Stepanyan, and O. Hassager. Extension induced phase separation and crystallization in semidilute solutions of ultra high molecular weight polyethylene. *Polymer*, 136:215–223, 2018.

[45] M. Kisilak, H. Anderson, N.S. Babcock, M.R. Stetzer, S.H.J. Idziak, and E.B. Sirota. An x-ray extensional flow cell. *Review of Scientific Instruments*, 72(11): 4305–4307, 2001.

[46] F.H.M. Swartjes, G.W.M. Peters, S. Rastogi, and H.E.H. Meijer. Stress induced crystallization in elongational flow. *International Polymer Processing*, 18(1):53–66, 2003.

[47] J. van Meerveld, G.W.M. Peters, and M. Hütter. Towards a rheological classification of flow induced crystallization experiments of polymer melts. *Rheologica Acta*, 44:119–134, 2004.

[48] T. Hu, N. Tian, S. Ali, Z. Wang, N. Chang, J.and Huang, and L. Li. Polymer–ion interaction weakens the strain-rate dependence of extension-induced crystallization for poly (ethylene oxide). *Langmuir*, 32(8):2117–2126, 2016.

[49] Z. Wang, F. Su, Y. Ji, H. Yang, N. Tian, J. Chang, L. Meng, and L.B. Li. Transition from chain-to crystal-network in extension induced crystallization of isotactic polypropylene. *Journal of Rheology*, 61(4):589–599, 2017.

[50] Z. Wang, J. Ju, L. Meng, N. Tian, H. Chang, J.and Yang, Y. Ji, F. Su, and L. Li. Structural and morphological transitions in extension-induced crystallization of poly (1-butene) melt. *Soft Matter*, 13(19):3639–3648, 2017.

[51] M.L. Sentmanat. Miniature universal testing platform: from extensional melt rheology to solid-state deformation behavior. *Rheologica acta*, 43(6):657–669, 2004.

[52] E.M. McCready and W.R. Burghardt. Structural response of a prealigned cylindrical block copolymer melt to extensional flow. *Journal of Rheology*, 59(4): 935–956, 2015.

[53] V. Tirtaatmadja and T. Sridhar. A filament stretching device for measurement of extensional viscosity. *Journal of Rheology*, 37(6):1081–1102, 1993.

[54] S.H. Spiegelberg, D.C. Ables, and G.H. McKinley. The role of end-effects on measurements of extensional viscosity in filament stretching rheometers. *Journal of Non-Newtonian Fluid Mechanics*, 64(2-3):229–267, 1996.

[55] G.H. McKinley and T. Sridhar. Filament-stretching rheometry of complex fluids. *Annual Review of Fluid Mechanics*, 34(1):375–415, 2002.

[56] A. Bach, H.K. Rasmussen, and O. Hassager. Extensional viscosity for polymer melts measured in the filament stretching rheometer. *Journal of Rheology*, 47(2): 429–441, 2003.

[57] N.V. Orr and T. Sridhar. Probing the dynamics of polymer solutions in extensional flow using step strain rate experiments. *Journal of non-newtonian fluid mechanics*, 82(2-3):203–232, 1999.

[58] J.M.R. Marín, J.K. Huusom, N.J. Alvarez, Q. Huang, H.K. Rasmussen, A. Bach, A.L. Skov, and O. Hassager. A control scheme for filament stretching rheometers with application to polymer melts. *Journal of Non-Newtonian Fluid Mechanics*, 194:14–22, 2013.

[59] S.L. Anna, C. Rogers, and G.H. McKinley. On controlling the kinematics of a filament stretching rheometer using a real-time active control mechanism. *Journal of non-newtonian fluid mechanics*, 87(2-3):307–335, 1999.

[60] H.J.M. Caelers, E.M. Troisi, L.E. Govaert, and G.W.M. Peters. Deformation-induced phase transitions in ipp polymorphs. *Polymers*, 9(10):547, 2017.

[61] A.P. Hammersley. Fit2d: a multi-purpose data reduction, analysis and visualization program. *Journal of Applied Crystallography*, 49(2):646–652, 2016.

[62] C.W. Macosko and R. G. Larson. Rheology: principles, measurements, and applications. 1994.

[63] G. Liu, H. Sun, S. Rangou, K. Ntetsikas, A. Avgeropoulos, and S-Q. Wang. Studying the origin of "strain hardening": Basic difference between extension and shear. *Journal of Rheology*, 57(1):89–104, 2013.

[64] C.Y.H.J Liu and R.B.C Keunings. New linearized relation for the universal viscosity-temperature behavior of polymer melts. *Macromolecules*, 39(25):8867–8869, 2006.

[65] Q. Huang, M. Mangnus, N.J. Alvarez, R. Koopmans, and O. Hassager. A new look at extensional rheology of low-density polyethylene. *Rheologica Acta*, 55:343–350, 2016.

[66] P. Szabo. Transient filament stretching rheometer: I: Force balance analysis. *Rheologica Acta*, 36:277–284, 1997.

[67] M. Yao and G.H. McKinley. Numerical simulation of extensional deformations of viscoelastic liquid bridges in filament stretching devices. *Journal of Non-Newtonian Fluid Mechanics*, 74(1-3):47–88, 1998.

[68] J.K. Nielsen, H.K. Rasmussen, and O. Hassager. Stress relaxation of narrow molar mass distribution polystyrene following uniaxial extension. *Journal of Rheology*, 52(4):885–899, 2008.

[69] M.I. Kolte, H.K. Rasmussen, and O. Hassager. Transient filament stretching rheometer: Ii: Numerical simulation. *Rheologica acta*, 36:285–302, 1997.

[70] M. Tolan and M. Tolan. *X-ray scattering from soft-matter thin films: materials science and basic research*, volume 148. Springer, 1999.

[71] N. Stribeck. *X-ray scattering of soft matter*. Springer Science & Business Media, 2007.

[72] M. van Drongelen, D. Cavallo, L. Balzano, G. Portale, I. Vittorias, W. Bras, G.C. Alfonso, and G.W.M. Peters. Structure development of low-density polyethylenes during film blowing: A real-time wide-angle x-ray diffraction study. *Macromolecular materials and engineering*, 299(12):1494–1512, 2014.

[73] A. Turner-Jones. The triclinic crystal form of polymethylenes and polyethylenes. *Journal of Polymer Science*, 62(174):S53–S56, 1962.

[74] M.M.H. Shirazi, M. Khajouei-Nezhad, S.M. Zebarjad, and R. Ebrahimi. *Polymer Bulletin*, 77:1681–1694, 2020.

[75] L. Poh, Q. Wu, Y. Chen, and E. Narimissa. Characterization of industrial low-density polyethylene: a thermal, dynamic mechanical, and rheological investigation. *Rheologica Acta*, 61(10):701–720, 2022.

[76] D. Duraccio, A. Mauriello, S. Cimmino, C. Silvestre, F. Auriemma, C. De Rosa, B. Pirozzi, and G.R. Mitchell. Structure–property relationships in polyethylene based films obtained by blow molding as model system of industrial relevance. *European Polymer Journal*, 62:97–107, 2015.

[77] S.K. Sen and S. Raut. Microbial degradation of low density polyethylene (ldpe): A review. *Journal of Environmental Chemical Engineering*, 3(1):462–473, 2015.

[78] R.N. Tharanathan. Biodegradable films and composite coatings: past, present and future. *Trends in food science & technology*, 14(3):71–78, 2003.

[79] M. Ozdemir and J.D. Floros. Active food packaging technologies. *Critical reviews in food science and nutrition*, 44(3):185–193, 2004.

[80] C. Silvestre and S. Cimmino. *Ecosustainable polymer nanomaterials for food packaging: innovative solutions, characterization needs, safety and environmental issues*. CRC Press, 2013.

[81] M. Salmerón Sánchez, V.B.F. Mathot, G. Vanden Poel, and J.L. Gómez Ribelles. Effect of the cooling rate on the nucleation kinetics of poly (l-lactic acid) and its influence on morphology. *Macromolecules*, 40(22):7989–7997, 2007.

[82] R. Androsch, H.M.N. Iqbal, and C. Schick. Non-isothermal crystal nucleation of poly (l-lactic acid). *Polymer*, 81:151–158, 2015.

[83] R. Pantani, I. Coccorullo, V. Volpe, and G. Titomanlio. Shear-induced nucleation and growth in isotactic polypropylene. *Macromolecules*, 43(21):9030–9038, 2010.

[84] A. Keller. Flow-induced orientation and structure formation. in proc, polymers. *Materials science and technology: a comprehensive treatment*, 18:189–268, 1997.

[85] F. Bustos, P. Cassagnau, and R. Fulchiron. Effect of molecular architecture on quiescent and shear-induced crystallization of polyethylene. *Journal of Polymer Science Part B: Polymer Physics*, 44(11):1597–1607, 2006.

[86] J. Tian, W. Yu, and C. Zhou. Crystallization kinetics of linear and long-chain branched polypropylene. *Journal of Macromolecular Science, Part B*, 45(5):969–985, 2006.

[87] M. Sugimoto, T. Tanaka, Y. Masubuchi, J-I. Takimoto, and K. Koyama. Effect of chain structure on the melt rheology of modified polypropylene. *Journal of Applied Polymer Science*, 73(8):1493–1500, 1999.

[88] A.D. Gotsis, B.L.F. Zeevenhoven, and C. Tsenoglou. Effect of long branches on the rheology of polypropylene. *Journal of rheology*, 48(4):895–914, 2004.

[89] Y. An, J.J. Holt, G.R. Mitchell, and A.S. Vaughan. Influence of molecular composition on the development of microstructure from sheared polyethylene melts: Molecular and lamellar templating. *Polymer*, 47(15):5643–5656, 2006.

[90] C.A. Sperati, W.A. Franta, and H.W. Starkweather Jr. The molecular structure of polyethylene. v. the effect of chain branching and molecular weight on physical properties1. *Journal of the American Chemical Society*, 75(24):6127–6133, 1953.

[91] F. Ania, F.J. Baltá Calleja, R.K. Bayer, A. Tshmel, I. Naumann, and G.H. Michler. Comparative study of size and distribution of lamellar thicknesses and long periods in polyethylene with a shish-kebab structure. *Journal of materials science*, 31: 4199–4206, 1996.

[92] D.R. Rueda, F. Ania, and F.J. BaltáCalleja. A usaxs study of melt processed pe with a shish-kebab structure: the influence of temperature on the long periods. *Polymer*, 38(9):2027–2032, 1997.

[93] L. Balzano, N. Kukalyekar, S. Rastogi, G.W.M. Peters, and J.C. Chadwick. Crystallization and dissolution of flow-induced precursors. *Physical review letters*, 100(4):048302, 2008.

[94] Z. Ma, L. Balzano, and G.W.M. Peters. Dissolution and re-emergence of flow-induced shish in polyethylene with a broad molecular weight distribution. *Macromolecules*, 49(7):2724–2730, 2016.

[95] J.K. Keum, C. Burger, F. Zuo, and B.S. Hsiao. Probing nucleation and growth behavior of twisted kebabs from shish scaffold in sheared polyethylene melts by in situ x-ray studies. *Polymer*, 48(15):4511–4519, 2007.

[96] B.S. Hsiao, L. Yang, R.H. Somani, C.A. Avila-Orta, and L. Zhu. Unexpected shish-kebab structure in a sheared polyethylene melt. *Physical review letters*, 94 (11):117802, 2005.

[97] M. van Drongelen, P.C. Roozemond, E.M. Troisi, A.K. Doufas, and G.W.M. Peters. Characterization of the primary and secondary crystallization kinetics of a linear low-density polyethylene in quiescent-and flow-conditions. *Polymer*, 76:254–270, 2015.

[98] E.M. Troisi, G. Portale, Z. Ma, M. van Drongelen, D. Hermida-Merino, and G.W.M. Peters. Unusual melting behavior in flow induced crystallization of lldpe: effect of pressure. *Macromolecules*, 48(8):2551–2560, 2015.

[99] J.K. Keum, C. Burger, B.S. Hsiao, R. Somani, L. Yang, B. Chu, R. Kolb, H. Chen, and C-T. Lue. *Synchrotron X-ray scattering studies of the nature of shear-induced shish-kebab structure in polyethylene melt*. Springer, 2005.

[100] J.K. Keum, F. Zuo, and B.S. Hsiao. Formation and stability of shear-induced shish-kebab structure in highly entangled melts of uhmwpe/hdpe blends. *Macromolecules*, 41(13):4766–4776, 2008.

[101] J. Pepe, L. C. Cleven, E.J.M.C. Suijkerbuijk, E.C.A. Dekkers, D. Hermida-Merino, R. Cardinaels, G.W.M. Peters, and P.D. Anderson. A filament stretching rheometer for in situ x-ray experiments: Combining rheology and crystalline morphology characterization. *Review of Scientific Instruments*, 91(7), 2020.

[102] T. Yan, B. Zhao, Y. Cong, Y. Fang, S. Cheng, L. Li, G. Pan, X. Wang, Z.and Li, and F. Bian. Critical strain for shish-kebab formation. *Macromolecules*, 43(2): 602–605, 2010.

[103] D. Liu, N. Tian, N. Huang, K. Cui, T. Wang, Z.and Hu, H. Yang, X. Li, and L. Li. Extension-induced nucleation under near-equilibrium conditions: the mechanism on the transition from point nucleus to shish. *Macromolecules*, 47(19):6813–6823, 2014.

[104] M. Doi and S.F. Edwards. *The theory of polymer dynamics*, volume 73. oxford university press, 1988.

[105] W.M.H. Verbeeten, G.W.M. Peters, and F.P.T. Baaijens. Differential constitutive equations for polymer melts: The extended pom–pom model. *Journal of Rheology*, 45(4):823–843, 2001.

[106] T.C.B. McLeish and R.G. Larson. Molecular constitutive equations for a class of branched polymers: The pom-pom polymer. *Journal of rheology*, 42(1):81–110, 1998.

[107] J-W. Housmans, R.J.A. Steenbakkers, P.C. Roozemond, G.W.M. Peters, and H.E.H. Meijer. Saturation of pointlike nuclei and the transition to oriented structures in flow-induced crystallization of isotactic polypropylene. *Macromolecules*, 42(15):5728–5740, 2009.

[108] P.C. Roozemond, Z. Ma, K. Cui, L. Li, and G.W.M. Peters. Multimorphological crystallization of shish-kebab structures in isotactic polypropylene: Quantitative modeling of parent–daughter crystallization kinetics. *Macromolecules*, 47(15):5152–5162, 2014.

[109] Z. Ma, L. Balzano, T. van Erp, G. Portale, and G.W.M. Peters. Short-term flow induced crystallization in isotactic polypropylene: How short is short? *Macromolecules*, 46(23):9249–9258, 2013.

[110] Andrew J Lovinger. Twisted crystals and the origin of banding in spherulites of semicrystalline polymers, 2020.

[111] B-J. De Gans, Paul C. Duineveld, and Ulrich S. Schubert. Inkjet printing of polymers: state of the art and future developments. *Advanced materials*, 16(3): 203–213, 2004.

[112] J.R. Castrejon-Pita, W.R.S. Baxter, J. Morgan, S. Temple, G.D. Martin, and I.M. Hutchings. Future, opportunities and challenges of inkjet technologies. *Atomization and sprays*, 23(6), 2013.

[113] S.D. Hoath. *Fundamentals of inkjet printing: the science of inkjet and droplets*. John Wiley & Sons, 2016.

[114] F.C. Godoi, S. Prakash, and B.R. Bhandari. 3d printing technologies applied for food design: Status and prospects. *Journal of Food Engineering*, 179:44–54, 2016.

[115] S.L. Voon, J. An, G. Wong, Y. Zhang, and C.K. Chua. 3d food printing: A categorised review of inks and their development. *Virtual and Physical Prototyping*, 14(3):203–218, 2019.

[116] S. Vadodaria and T. Mills. Jetting-based 3d printing of edible materials. *Food Hydrocolloids*, 106:105857, 2020.

[117] N. Karim, S. Afroj, S. Tan, K. S Novoselov, and S.G. Yeates. All inkjet-printed graphene-silver composite ink on textiles for highly conductive wearable electronics applications. *Scientific reports*, 9(1):8035, 2019.

[118] M. He, L. Sun, K. Hu, Y. Zhu, L. Ma, H. Chen, et al. Drop-on-demand inkjet printhead performance enhancement by dynamic lumped element modeling for printable electronics fabrication. *Mathematical Problems in Engineering*, 2014, 2014.

[119] D.S. Saidina, N. Eawwiboonthanakit, M. Mariatti, S. Fontana, and C. Hérold. Recent development of graphene-based ink and other conductive material-based inks for flexible electronics. *Journal of Electronic Materials*, 48:3428–3450, 2019.

[120] I.J. Fernandes, A.F. Aroche, A. Schuck, P. Lamberty, C.R. Peter, W. Hasenkamp, and T.L.A.C. Rocha. Silver nanoparticle conductive inks: Synthesis, characterization, and fabrication of inkjet-printed flexible electrodes. *Scientific reports*, 10(1):8878, 2020.

[121] J.Y.H. Fuh, J. Sun, E.Q. Li, L. Li, J.and Chang, G.S. Hong, Y.S. Wong, and E.S. Thian. Micro and bio-rapid prototyping using drop-on-demand 3d printing. In *HandBook of Manufacturing Engineering and Technology*, pages 2567–2583. Springer-Verlag London Ltd, 2015.

[122] S. Azizi Machekposhti, S. Mohaved, and R.J. Narayan. Inkjet dispensing technologies: recent advances for novel drug discovery. *Expert opinion on drug discovery*, 14(2):101–113, 2019.

[123] R.D Boehm, P.R Miller, J. Daniels, and R.J. Stafslien, S.and Narayan. Inkjet printing for pharmaceutical applications. *Materials Today*, 17(5):247–252, 2014.

[124] M. Pandey, H. Choudhury, J.L.C. Fern, A.T.K. Kee, J. Kou, J.L.J. Jing, H.C. Her, H.S. Yong, H.C. Ming, S.K. Bhattamisra, et al. 3d printing for oral drug delivery: a new tool to customize drug delivery. *Drug delivery and translational research*, 10:986–1001, 2020.

[125] A.J. Babiarz. Jetting small dots of high viscosity fluids for packaging applications. *Semiconductor International*, 29(9):2–6, 2006.

[126] M Eslamian and N Ashgriz. Drop-on-demand drop generators. *Handbook of Atomization and Sprays: Theory and Applications*, pages 581–601, 2011.

[127] D. Jang, D. Kim, and J. Moon. Influence of fluid physical properties on ink-jet printability. *Langmuir*, 25(5):2629–2635, 2009.

[128] S.D. Hoath, I.M. Hutchings, G.D. Martin, T.R. Tuladhar, M.R. Mackley, and D. Vadillo. Links between ink rheology, drop-on-demand jet formation, and printability. *J. Imaging Sci. Technol*, 53(4):041208, 2009.

[129] S. Krainer, C. Smit, and U. Hirn. The effect of viscosity and surface tension on inkjet printed picoliter dots. *RSC advances*, 9(54):31708–31719, 2019.

[130] O.A. Basaran. Small-scale free surface flows with breakup: Drop formation and emerging applications. *American Institute of Chemical Engineers. AIChE Journal*, 48(9):1842, 2002.

[131] P. Delrot, M.A. Modestino, D. Psaltis, and C. Moser. Laser-assisted inkjet printing of highly viscous fluids with sub-nozzle resolution. In *Laser 3D Manufacturing III*, volume 9738, pages 14–20. SPIE, 2016.

[132] I.H. Choi and J. Kim. A pneumatically driven inkjet printing system for highly viscous microdroplet formation. *Micro and Nano Systems Letters*, 4(1):1–7, 2016.

[133] R.J. Houben. Equipment for printing of high viscosity liquids and molten metals. 2012.

[134] P.J. Smith and A. Morrin. Reactive inkjet printing. *Journal of Materials Chemistry*, 22(22):10965–10970, 2012.

[135] S. Fathi and P. Dickens. Challenges in drop-on-drop deposition of reactive molten nylon materials for additive manufacturing. *Journal of Materials Processing Technology*, 213(1):84–93, 2013.

[136] C. Sturgess, C.J. Tuck, I.A Ashcroft, and R.D. Wildman. 3d reactive inkjet printing of polydimethylsiloxane. *Journal of Materials Chemistry C*, 5(37):9733–9743, 2017.

[137] E. Saleh, P. Woolliams, B. Clarke, A. Gregory, S. Greedy, C. Smartt, R. Wildman, I. Ashcroft, R. Hague, P. Dickens, et al. 3d inkjet-printed uv-curable inks for multi-functional electromagnetic applications. *Additive Manufacturing*, 13:143–148, 2017.

[138] E.M. Hamad, S.E.R. Bilatto, N.Y. Adly, D.S. Correa, B. Wolfrum, M.J. Schöning, A. Offenhäusser, and A. Yakushenko. Inkjet printing of uv-curable adhesive and dielectric inks for microfluidic devices. *Lab on a Chip*, 16(1):70–74, 2016.

[139] Y. Yang, S. Gu, J. Liu, H. Tian, and Q. Lv. Research and development of a 3d jet printer for high-viscosity molten liquids. *Micromachines*, 9(11):554, 2018.

[140] J. Kurz, A.and Bauer and M. Wagner. Piezo-plunger jetting technology: An experimental study on jetting characteristics of filled epoxy polymers. *Fluids*, 4(1): 23, 2019.

[141] S. Wu and H. Mohammadigoushki. Effects of moving contact line on filament pinch-off dynamics of viscoelastic surfactant fluids. *Physical Review Fluids*, 5(5): 053303, 2020.

[142] H. Chen, A. Ponce-Torres, J.M. Montanero, and A. Amirfazli. Viscoelastic liquid bridge breakup and liquid transfer between two surfaces. *Journal of Colloid and Interface Science*, 582:1251–1256, 2021.

[143] S. Kumar. Liquid transfer in printing processes: Liquid bridges with moving contact lines. *Annual Review of Fluid Mechanics*, 47:67–94, 2015.

[144] S. Dodds, M.S. Carvalho, and S. Kumar. The dynamics of three-dimensional liquid bridges with pinned and moving contact lines. *Journal of fluid mechanics*, 707:521–540, 2012.

[145] C. Gupta, G.A. Mensing, M.A. Shannon, and P.J.A. Kenis. Double transfer printing of small volumes of liquids. *Langmuir*, 23(5):2906–2914, 2007.

[146] T.M. Squires and S.R. Quake. Microfluidics: Fluid physics at the nanoliter scale. *Reviews of modern physics*, 77(3):977, 2005.

[147] T. Ward. Capillary-pressure driven adhesion of rigid-planar surfaces. *Journal of colloid and interface science*, 354(2):816–824, 2011.

[148] M.J. Vogel and P.H. Steen. Capillarity-based switchable adhesion. *Proceedings of the National Academy of Sciences*, 107(8):3377–3381, 2010.

[149] M. Rosello, S. Sur, B. Barbet, and J.P. Rothstein. Dripping-onto-substrate capillary breakup extensional rheometry of low-viscosity printing inks. *Journal of Non-Newtonian Fluid Mechanics*, 266:160–170, 2019.

[150] J. Dinic, L.N. Jimenez, and V. Sharma. Pinch-off dynamics and dripping-onto-substrate (dos) rheometry of complex fluids. *Lab on a Chip*, 17(3):460–473, 2017.

[151] C. Clasen. Capillary breakup extensional rheometry of semi-dilute polymer solutions. *Korea-Australia Rheology Journal*, 22(4):331–338, 2010.

[152] M. Rubio-Rubio, W. Mathues, A. Sevilla, and C. Clasen. One-dimensional modelling of the thinning of particulate suspensions near pinch-off. *International Journal of Multiphase Flow*, 108:202–210, 2018.

[153] S.S. Vadodaria and R.J. English. Extensional rheometry of cellulose ether solutions: flow instability. *Cellulose*, 23:339–355, 2016.

[154] G.H. McKinley and A. Tripathi. How to extract the newtonian viscosity from capillary breakup measurements in a filament rheometer. *Journal of Rheology*, 44 (3):653–670, 2000.

[155] T.R. Tuladhar and M.R. Mackley. Filament stretching rheometry and break-up behaviour of low viscosity polymer solutions and inkjet fluids. *Journal of Non-Newtonian Fluid Mechanics*, 148(1-3):97–108, 2008.

[156] D.C. Vadillo, T.R. Tuladhar, A.C. Mulji, S. Jung, S.D. Hoath, and M.R. Mackley. Evaluation of the inkjet fluid's performance using the "cambridge trimaster" filament stretch and break-up device. *Journal of Rheology*, 54(2):261–282, 2010.

[157] H.V.M. Kibbelaar, A. Deblais, F. Burla, G.H. Koenderink, K.P. Velikov, and D. Bonn. Capillary thinning of elastic and viscoelastic threads: From elastocapillarity to phase separation. *Physical Review Fluids*, 5(9):092001, 2020.

[158] C-D. Xue, X-D. Chen, Y-J. Li, G-Q. Hu, T. Cao, and K-R. Qin. Breakup dynamics of semi-dilute polymer solutions in a microfluidic flow-focusing device. *Micromachines*, 11(4):406, 2020.

[159] D. Bonn, J. Eggers, J. Indekeu, J. Meunier, and E. Rolley. Wetting and spreading. *Reviews of modern physics*, 81(2):739, 2009.

[160] J.H. Snoeijer and B. Andreotti. Moving contact lines: scales, regimes, and dynamical transitions. *Annual review of fluid mechanics*, 45:269–292, 2013.

[161] J-H. Kim and J.P. Rothstein. Dynamic contact angle measurements of viscoelastic fluids. *Journal of Non-Newtonian Fluid Mechanics*, 225:54–61, 2015.

[162] Y. Wang, D-Q. Minh, and G. Amberg. Dynamic wetting of viscoelastic droplets. *Physical Review E*, 92(4):043002, 2015.

[163] V. Charitatos, W.J. Suszynski, M.S. Carvalho, and S. Kumar. Dynamic wetting failure in shear-thinning and shear-thickening liquids. *Journal of Fluid Mechanics*, 892:A1, 2020.

[164] A. Carlson, M. Do-Quang, and G. Amberg. Dissipation in rapid dynamic wetting. *Journal of Fluid Mechanics*, 682:213–240, 2011.

[165] D. Duvivier, D. Seveno, R. Rioboo, T.D. Blake, and J. De Coninck. Experimental evidence of the role of viscosity in the molecular kinetic theory of dynamic wetting. *Langmuir*, 27(21):13015–13021, 2011.

[166] L. Chen and E. Bonaccurso. Effects of surface wettability and liquid viscosity on the dynamic wetting of individual drops. *Physical Review E*, 90(2):022401, 2014.

[167] Z. Shi, Y. Zhang, M. Liu, D.A.H. Hanaor, and Y. Gan. Dynamic contact angle hysteresis in liquid bridges. *Colloids and Surfaces A: Physicochemical and Engineering Aspects*, 555:365–371, 2018.

[168] A. Akbari and R.J. Hill. Liquid-bridge stability and breakup on surfaces with contact-angle hysteresis. *Soft Matter*, 12(32):6868–6882, 2016.

[169] A. Akbari, R.J. Hill, and T.G.M. van de Ven. Liquid-bridge breakup in contact-drop dispensing: Liquid-bridge stability with a free contact line. *Physical Review E*, 92(2):022404, 2015.

[170] H. Chen, T. Tang, and A. Amirfazli. Liquid transfer mechanism between two surfaces and the role of contact angles. *Soft matter*, 10(15):2503–2507, 2014.

[171] H. Chen, A. Amirfazli, and T. Tang. Modeling liquid bridge between surfaces with contact angle hysteresis. *Langmuir*, 29(10):3310–3319, 2013.

[172] H. Chen, T. Tang, and A. Amirfazli. Fast liquid transfer between surfaces: breakup of stretched liquid bridges. *Langmuir*, 31(42):11470–11476, 2015.

[173] H. Chen, T. Tang, and A. Amirfazli. Effects of surface wettability on fast liquid transfer. *Physics of Fluids*, 27(11), 2015.

[174] H. Chen, T. Tang, H. Zhao, K-Y. Law, and A.J.S.M. Amirfazli. How pinning and contact angle hysteresis govern quasi-static liquid drop transfer. *Soft Matter*, 12 (7):1998–2008, 2016.

[175] B. Qian and K.S. Breuer. The motion, stability and breakup of a stretching liquid bridge with a receding contact line. *Journal of Fluid Mechanics*, 666:554–572, 2011.

[176] F.A. Morrison et al. *Understanding rheology*. Oxford University Press, USA, 2001.

[177] Z. Kőkuti, K. van Gruijthuijsen, M. Jenei, G. Toth-Molnar, A. Czirjak, J. Kokavecz, P. Ailer, L. Palkovics, A.C. Völker, and G. Szabo. High-frequency rheology of a high viscosity silicone oil using diffusing wave spectroscopy. *Applied Rheology*, 24 (6):32–38, 2014.

[178] M. Rudolf, D. Boutelier, M. Rosenau, G. Schreurs, and O. Oncken. Rheological benchmark of silicone oils used for analog modeling of short-and long-term lithospheric deformation. *Tectonophysics*, 684:12–22, 2016.

[179] H. Yang, Y. He, C. Tuck, R. Wildman, I. Ashcroft, P. Dickens, and R. Hague. High viscosity jetting system for 3d reactive inkjet printing. In *2013 International Solid Freeform Fabrication Symposium*. University of Texas at Austin, 2013.

[180] M. Rubinstein, R.H. Colby, et al. *Polymer physics*, volume 23. Oxford university press New York, 2003.

[181] L-H. Cai, T.E. Kodger, R.E. Guerra, A.F. Pegoraro, M. Rubinstein, and D.A. Weitz. Soft poly (dimethylsiloxane) elastomers from architecture-driven entanglement free design. *Advanced Materials*, 27(35):5132–5140, 2015.

[182] A.Y. Malkin. Flow instability in polymer solutions and melts. *Polymer Science Series C*, 48(1):21–37, 2006.

[183] G.H. McKinley. Visco-elasto-capillary thinning and break-up of complex fluids. 2005.

[184] C. Clasen, P.M Phillips, L. Palangetic, Vermant, and J. Dispensing of rheologically complex fluids: The map of misery. *AIChE Journal*, 58(10):3242–3255, 2012.

[185] J.C Bird, S. Mandre, and H.A. Stone. Short-time dynamics of partial wetting. *Physical review letters*, 100(23):234501, 2008.

[186] Š. Šikalo, C. Tropea, and E.N. Ganić. Dynamic wetting angle of a spreading droplet. *Experimental Thermal and Fluid Science*, 29(7):795–802, 2005.

[187] TD Blake, M Bracke, and YD Shikhmurzaev. Experimental evidence of nonlocal hydrodynamic influence on the dynamic contact angle. *Physics of fluids*, 11(8): 1995–2007, 1999.

[188] K-Y. Law. Definitions for hydrophilicity, hydrophobicity, and superhydrophobicity: getting the basics right, 2014.

[189] Q. Zheng and C. Lü. Size effects of surface roughness to superhydrophobicity. *Procedia IUtam*, 10:462–475, 2014.

[190] Z. Pan, H. Shahsavan, W. Zhang, F.K. Y, and B. Zhao. Superhydro-oleophobic bio-inspired polydimethylsiloxane micropillared surface via fdts coating/blending approaches. *Applied Surface Science*, 324:612–620, 2015.

[191] W. Tuteja, A.and Choi, M. Ma, J.M. Mabry, S.A. Mazzella, G.C. Rutledge, G.H. McKinley, and R.E. Cohen. Designing superoleophobic surfaces. *Science*, 318 (5856):1618–1622, 2007.

[192] M.A. Nilsson, R.J. Daniello, and J.P. Rothstein. A novel and inexpensive technique for creating superhydrophobic surfaces using teflon and sandpaper. *Journal of Physics D: Applied Physics*, 43(4):045301, 2010.

[193] T. Darmanin and F. Guittard. Superhydrophobic and superoleophobic properties in nature. *Materials today*, 18(5):273–285, 2015.

[194] B. Bhushan. Biomimetics: lessons from nature–an overview. *Philosophical Transactions of the Royal Society A: Mathematical, Physical and Engineering Sciences*, 367(1893):1445–1486, 2009.

[195] M. Liu, Y. Zheng, J. Zhai, and L. Jiang. Bioinspired super-antiwetting interfaces with special liquid- solid adhesion. *Accounts of chemical research*, 43(3):368–377, 2010.

[196] Y-L. Zhang, Q-D. Chen, Z. Jin, E. Kim, and H-B. Sun. Biomimetic graphene films and their properties. *Nanoscale*, 4(16):4858–4869, 2012.

[197] J. Yong, F. Chen, J. Yang, Q.and Huo, and X. Hou. Superoleophobic surfaces. *Chemical Society Reviews*, 46(14):4168–4217, 2017.

[198] D. Kim, N.M. Pugno, and S. Ryu. Wetting theory for small droplets on textured solid surfaces. *Scientific reports*, 6(1):37813, 2016.

[199] M.S. Ambrosia, M.Y. Ha, and S. Balachandar. The effect of pillar surface fraction and pillar height on contact angles using molecular dynamics. *Applied surface science*, 282:211–216, 2013.

[200] R.N. Wenzel. Resistance of solid surfaces to wetting by water. *Industrial & engineering chemistry*, 28(8):988–994, 1936.

[201] A.B.D. Cassie and S.J.T.O.T.F.S. Baxter. Wettability of porous surfaces. *Transactions of the Faraday society*, 40:546–551, 1944.

[202] A. Marmur and E. Bittoun. When wenzel and cassie are right: reconciling local and global considerations. *Langmuir*, 25(3):1277–1281, 2009.

[203] S. Krainer and U. Hirn. Contact angle measurement on porous substrates: Effect of liquid absorption and drop size. *Colloids and Surfaces A: Physicochemical and Engineering Aspects*, 619:126503, 2021.

[204] M.W. Pinson and T. Wang. Effects of leading-edge roughness on fluid flow and heat transfer in the transitional boundary layer over a flat plate. *International journal of heat and mass transfer*, 40(12):2813–2823, 1997.

[205] D.J. Bouchard and S. Chandra. Infiltration of impacting droplets into porous substrates. *Experiments in Fluids*, 61:1–16, 2020.

Publications

Belonging to this thesis:

1. Pepe, J., Cleven, L.C., Suijkerbuijk, E.J., Dekkers, E.C., Hermida-Merino, D., Cardinaels, R., Peters, G.W. and Anderson, P.D., 2020. A filament stretching rheometer for in situ X-ray experiments: Combining rheology and crystalline morphology characterization. *Review of Scientific Instruments, 91(7).*

2. Pepe, J., Cardinaels, R., Peters, G.W. and Anderson, P.D. Unraveling the extensional flow induced crystallization of LDPE via *in-situ* X-ray characterization. *In preparation.*

3. Pepe, J., Cardinaels, R., Peters, G.W. and Anderson, P.D. A study on the jetting and spreading process of highly viscous fluids. *In preparation.*

Acknowledgment

This work would have not been possible without the valuable contribution of many people. My gratitude to Patrick for giving me the opportunity to embark in this journey, to collaborate with various groups and academia and presenting work at conferences. Many thanks for your valuable advice that helped me to improve as professional. My acknowledgment to Gerrit for your invaluable scientific contribution, for your creativity, and life lessons, I truly enjoyed your talks about... well, pretty much everything! To Ruth, without you this work would have not been possible. Thanks for your constant guidance, help and passion. From you I have learned to be more critical and structured and that there are no good or bad results in research. I would like to thank Brightlands Material Center (BMC) for funding my PhD project. Thanks to the members of my committee for being part of this, and for all the valuable feedback. Many thanks to many people that worked in the background. I would like to thank Ole Hassager and Qian Huang for the training on filament stretching rheometer measurements at the Technical University of Denmark (DTU). To Luigi Balzano for the constructive discussions on crystallization and his support over the past years. Thanks to Martin van Drongelen for his advice on experimental work. Thanks to Lucien for his help in building the setups developed in this study and his support in everyday lab work. Thanks to the team of the Equipment and Prototyping Center of TU/e for their collaboration in designing and building the extensional rheometer. To Daniel for all his support and help (24/7) at ESRF during our great beam time. Thanks to Stan for all the driving and the sleepless nights during the beam time. Many thanks to Ans for her great support and kindness. I would like to thank all the friends that have shared with me this journey for their moral support that helped overcome difficult times (no need to mention names!). To all my colleagues of Lake3D for their encouragement in the last period. To part of my family spread across the world thanks for your support. To the designer of the cover of this thesis thanks for this and much much more! In ultimo vorrei ringraziare la mia famiglia per il loro supporto e amore incondizionato, a voi tutta la mia gratitudine e ripetto. Grazie di cuore!

Curriculum Vitae

Jessica Pepe was born on 22nd of August 1991 in Salerno, Italy. After obtaining her Bachelor degree in Chemical Engineering at University of Salerno, she continued her studies pursuing a Master in the same field. During this period she obtained the Erasmus scholarship to carry out an internship at DSM Material Science, Geleen, The Netherlands. During this time she studied the effect of solvent quality on drawability of UHMWPE fibers under the supervision dr. L. Balzano, dr. Roman Stepanyan and dr.ir. P.C. Roozemond. After obtaining her Master degree in Chemical Engineering with specialization in polymer processing she took a position as Doctoral candidate in the Polymer Technology group at Eindhoven University of Technology, Eindhoven, The Netherlands, under the supervision of prof.dr.ir. P.D. Anderson and co-supervisors, prof.dr.ir. G.W.M. Peters and prof. dr.ir. R. Cardinaels, of which the results are presented in this dissertation. In April 2021 she joined Lake3D B.V. as Process Developer.